



National  
Defence

Défense  
nationale



# MULTIPATH MODELLING FOR TERRESTRIAL VHF RADIO DIRECTION FINDING (U)

by

William Read

DTIC QUALITY INSPECTED 2

DISTRIBUTION STATEMENT A

Approved for public release;  
Distribution Unlimited

DEFENCE RESEARCH ESTABLISHMENT OTTAWA  
REPORT NO. 1300

Canada

19970115 057

December 1996  
Ottawa

## ABSTRACT

This report details the development of computer models to investigate and explain the effects of multipath on VHF radio direction finding (DF). The motivation for this development was to help explain the large and small scale multipath effects which occur for changes in transmitter and receiver position, or for changes in frequency. This is particularly important when analyzing the capabilities of current wide and narrow band DF methods, or when developing new DF methods. The development of the computer models is based on representing the terrain and vegetation affecting the signal by a large number of small (relative to the signal wavelength) isotropic reradiators. Polarization effects are not accounted for. Although this kind of approach can quickly become a computationally daunting task, a number of simplifications are introduced which greatly simplify the calculations. Two examples have been included illustrating the use of the proposed approach in the analysis and modelling of real world measurements.

## RÉSUMÉ

Le présent rapport expose en détails la conception de modèles informatiques permettant l'examen et l'explication des effets des trajets multiples sur la radiogoniométrie VHF. Nous avons conçu ces modèles dans le but de pouvoir expliquer les effets à grande et à petite échelle des trajets multiples qui se produisent lors de changements dans la position de l'émetteur et du récepteur ou dans la fréquence. Cela s'avère particulièrement important lors de l'analyse des capacités des méthodes actuelles de radiogoniométrie de bandes larges et restreintes ou dans le cadre de l'élaboration de nouvelles méthodes. La conception de ces modèles informatiques s'appuie sur la représentation du relief et de la végétation affectant le signal par un grand nombre de petites (par rapport à la longueur d'onde du signal) antennes isotropes de réémission. Nous n'avons pas rendu compte des effets de polarisation. Bien qu'une telle approche puisse rapidement devenir une tâche computationnelle intimidante, nous avons incorporé certaines simplifications qui facilitent grandement les calculs. Nous incluons deux exemples qui illustrent l'utilisation de l'approche proposée dans le cadre de l'analyse et de la modélisation des mesures du monde réel.

## EXECUTIVE SUMMARY

Improvement of communications radio direction finding (DF) accuracy is a high priority for the Canadian and Allied Forces. To this end, research in advanced DF techniques has been carried out worldwide over the last two decades with the view of taking advantage of advances in DF algorithms as well as the capabilities of modern processing technology. At the Defence Research Establishment Ottawa (DREO), a series of field trials were carried out to quantify the effects of multipath propagation during the Spring of 1994. The field measurements were carried out using an experimental eight-channel VHF DF system called the Osprey System.

In analyzing the field trial data it quickly became evident that the multipath environment has a complex effect on the transmitter signal. To properly understand the information yielded by the collected data, it was deemed necessary to develop computer models so that multipath effects could be simulated under strict control – something that is not possible in the real world.

The approach used to develop these computer models was to break the physical environment into an immense grid of individual reradiating elements. Analogous to digitizing an audio signal except using position (3-dimensions) instead of time (1-dimension). A large part of the report deals with the development of this grid model, beginning with a single reradiating element then analyzing the effect of collections of reradiating elements. This includes an analysis of the effect of size and shape of the collection of reradiators on an impinging signal, and the resultant reradiated signal. This is followed by an analysis of the interaction between reradiator elements (i.e. mutual coupling) and finally the effect of an infinite grid of reradiators (to represent the ground). Although the mathematics become quite involved, the results agree with both the laws of physics and common sense views of the real world – necessary conditions in order for a modelling approach to be successful.

Given that the reradiating elements must be small in order to accurately represent features which cause multipath, the computational burden may increase prohibitively as the number or size of these features increases. Consequently, this report also deals with the appropriate simplifications that can be made to greatly reduce this computation burden. These simplifications are somewhat dependent on the physical environment being modelled, so that there are some cases where simplifications are not possible (i.e. very

uneven ground or very uneven vegetation requiring lots of individual features to be modelled) so more work remains to be done in this area. However, for many real situations the proposed simplifications can be employed with good success. To demonstrate this point, two examples showing the simulation of measurements that have been made in the real world have also been included.

The main benefit of the new approach is the ability to model various aspects of the environment which will lead to a better understanding of the actual sources of multipath, their numbers, and locations. This will allow the multipath environment to be properly modelled for the purposes of testing DF methods and calibration techniques, as well as open up the possibility of developing new methods which are capable of significantly improving the accuracy of DF compared to current approaches.



## TABLE OF CONTENTS

	<u>Page</u>
ABSTRACT/RÉSUMÉ . . . . .	iii
EXECUTIVE SUMMARY . . . . .	v
TABLE OF CONTENTS . . . . .	vii
LIST OF FIGURES . . . . .	ix
 1.0 INTRODUCTION . . . . .	 1
1.1 The Modelling Approach . . . . .	3
1.2 Further Considerations . . . . .	5
 2.0 MULTIPATH SOURCE CHARACTERISTICS . . . . .	 12
2.1 The Discrete Reradiator . . . . .	12
2.2 Collections of Reradiators . . . . .	14
2.3 Characterizing Multipath Sources . . . . .	17
2.3.1 Beam Power . . . . .	21
2.3.2 Beamwidth . . . . .	21
2.3.3 Beam Phase . . . . .	31
2.3.4 Reflections . . . . .	31
2.3.5 The Beam Model . . . . .	36
 3.0 COUPLING EFFECTS . . . . .	 37
3.1 Coupling within a Multipath Source . . . . .	37
3.2 Characteristics of a Coupled Multipath Source . . . . .	41
3.2.1 Effect on Power . . . . .	41
3.2.2 Effect on Beamwidth . . . . .	45
3.2.3 Effect on Phase . . . . .	45
3.2.4 Enhancement of Reflections . . . . .	46
3.2.5 The Modified Beam Model . . . . .	48
3.3 Processing for More Than One Multipath Source . . . . .	48
3.3.1 Coupling between Multipath Sources . . . . .	49
3.3.2 Internal Coupling . . . . .	52
3.3.3 Comparing Coupling Methods . . . . .	53
 4.0 THE GROUND PLANE . . . . .	 63
4.1 The Ideal Ground Plane . . . . .	63
4.2 Vegetation and Terrain Features . . . . .	68
4.3 Variations in the Reradiation Properties . . . . .	72
 5.0 SUMMARY OF MULTIPATH EQUATIONS . . . . .	 78
5.1 Freespace Equations . . . . .	79
5.2 Vegetation and Terrain Feature Equations . . . . .	79
5.3 Nonhomogeneous Dielectric Earth Equations . . . . .	80

6.0 REAL WORLD MODELLING EXAMPLES . . . . .	81
6.1 Example 1 . . . . .	81
6.2 Example 2 . . . . .	88
6.3 Assumption Verification . . . . .	90
7.0 CONCLUSIONS . . . . .	93
REFERENCES . . . . .	REF-1
A.0 CIRCULAR GROUND GRID CALCULATIONS . . . . .	A-1

## LIST OF FIGURES

	<u>Page</u>
Figure 1: Experimental N channel DF system block diagram. . . . .	2
Figure 2: Signal power for a moving transmitter . . . . .	6
Figure 3: Overview of a signal impinging on a large obstacle . . . . .	8
Figure 4: Cartesian coordinate system representation for multipath source position. . . . .	16
Figure 5: Geometry of simulation experiment to determine multipath source output as a function of receiver azimuth. . . . .	18
Figure 6: Multipath signal power as a function of receiver azimuth angle for multipath line sources. . . . .	19
Figure 7: Multipath signal phase as a function of receiver azimuth angle for multipath line sources. . . . .	20
Figure 8: Vector representation of summation terms for a line source. . . . .	23
Figure 9: Map showing phase contours as a function of position relative to the center of the multipath source. . . . .	24
Figure 10: Geometry of line multipath source (open circles) and zero-phase line (dotted line) for $\phi' = 30^\circ$ . . . . .	26
Figure 11: Dumbbell multipath source showing (a) geometry and zero-phase line for $\phi' = 27.2^\circ$ , and (b) multipath power as a function of $\phi$ . . . . .	27
Figure 12: Dumbbell source vector diagram for $\phi' = 27.2^\circ$ . . . . .	28
Figure 13: Bent cross multipath source showing (a) geometry and zero-phase line for $\phi' = 43.2^\circ$ , and (b) multipath power as a function of $\phi$ . . . . .	29
Figure 14: Bent cross source vector diagram for $\phi' = 43.2^\circ$ . . . . .	30
Figure 15: Multipath source main beam phase for the (a) line source, (b) dumbbell, and (c) bent cross. . . . .	32
Figure 16: Reflection beam generated by a line source for different orientations. . . . .	34

Figure 17:	Comparison of the reflection beam generated by (a) a line source, (b) a thin rectangular shaped source, and (c) a thicker rectangular shaped source. . . . .	35
Figure 18:	Multipath source power (with coupling effects included) as a function of azimuth for the (a) line source, (b) dumbbell, and (c) bent cross. . . . .	39
Figure 19:	Multipath source main beam phase (with coupling effects included) for the (a) line source, (b) dumbbell, and (c) bent cross. . . . .	40
Figure 20:	Maximum power for the line source as the reradiator spacing $d$ is varied while $\mu_m^2$ is kept constant. . . . .	42
Figure 21:	Depiction of the first ten Fresnel zones for a transmitter and the $k^{th}$ reradiator. . . . .	44
Figure 22:	Comparison of the reflection beam generated by (a) a line source, (b) a thin rectangular shaped source, and (c) a thicker rectangular shaped source. . . . .	47
Figure 23:	Map used for simulation purposes and showing the geometry of the transmitter, receiver, and two multipath sources. . . . .	54
Figure 24:	Configuration of reradiators used to create a wall-like multipath source. . . . .	55
Figure 25:	Relative amplitude of signal at receiver calculated using (a) the full coupling method, (b) the multipath source coupling method, and (c) the internal coupling method. . . . .	56
Figure 26:	Map of locations of transmitter, receiver, and multipath sources used in simulation to investigate effect of spacing. . . . .	58
Figure 27:	Mean squared error results for two approximate methods as a function of spacing between multipath sources. . . . .	59
Figure 28:	Map showing setup used for multipath simulation involving seven multipath sources. . . . .	61
Figure 29:	Multipath simulation showing relative amplitude of signal at the receiver calculated using (a) the full coupling method, (b) the multipath source coupling method, and (c) the internal coupling method. . . . .	62
Figure 30:	Ideal ground plane showing direct and reflected signals. . . . .	64
Figure 31:	Geometry of a circular grid used for ground simulations. . . . .	65

Figure 32:	Results of ground simulation for $\beta = -1$ showing the magnitude of the reradiator signals as a function of distance from the transmitter.	66
Figure 33:	Above ground multipath source model. . . . .	68
Figure 34:	Values of the coupling elements $\gamma_{kl}$ as a function of the distance between reradiators $r_{kl}$ . . . . .	75
Figure 35:	Map showing site of multipath measurements carried out at DREO in 1994. . . . .	82
Figure 36:	Received signal power measured with respect to the transmitter position. . . . .	82
Figure 37:	Shape of multipath sources showing reradiator positions for (a) small scatterer model, (b) tree model, and (c) large reflector model. . . . .	84
Figure 38:	Location of most significant multipath sources using (a) small scatterer model, (b) tree model, and (c) large reflector model. . . . .	86
Figure 39:	Received signal power using (a) small scatterer model, (b) tree model, and (c) large reflector model. . . . .	87
Figure 40:	Map showing site of wideband DF measurements carried out at DREO in 1992. . . . .	89
Figure 41:	Received signal power measured with respect to the transmitter frequency. . . . .	89
Figure 42:	Received signal power using (a) tree model, and (b) large reflector model. . . . .	91

## 1.0 INTRODUCTION

Improvement of communications radio direction finding (DF) accuracy is a high priority for the Canadian and Allied Forces. To this end, research in advanced DF techniques has been carried out worldwide over the last two decades with the view of taking advantage of advances in DF algorithms as well as the capabilities of modern processing technology. Central to this approach is the  $N$ -channel digital beamformer, one possible version of which is shown in block diagram form in Figure 1. The main advantage of this approach is that the phase and amplitude measurements from each antenna are available for analysis. This maximizes the information available about the incoming radio signal which allows multiple signal DF (superresolution) to be performed, or distortion of the received wavefront (compared to theoretical expectations) to be measured.

In recent years it has become evident that multipath propagation can severely degrade the accuracy of tactical VHF DF systems operated over land. To investigate the effects of multipath on DF, an eight-channel hardware realization of Figure 1, called the Osprey System, was set up at DREO. A series of field measurements were carried out with this system during the Fall of 1992 and the Spring of 1993, and reported in [1]. These trials confirmed that under good conditions (e.g. high signal-to-noise ratio signals, no wind, properly calibrated equipment, etc.), multipath is a dominant source of error. The trials also showed that the DF bearing errors induced by multipath were random as a function of transmitter azimuth and likely range as well. The implication of this result was that the number of sources of multipath was large and the multipath environment complex.

In the spring of 1994, a second set of measurement trials was carried out in the Ottawa area to further investigate the random nature of multipath. The measurement data was initially analyzed and further insight into the multipath phenomena was gained. However many questions remained unanswered such as, for example, the physical cause of the multipath, as well as the numbers and distribution of the multipath sources. To this end, multipath computer models were developed and various computer simulations were run in an effort to duplicate characteristics seen in the measurement data. The results of this effort were very successful, yielding valuable information about the multipath environment which would have been difficult to derive otherwise. Since the theoretical justification for the computer models is quite involved, the model development, and the analysis of the measurement data (including comparison with the model data) have been broken into two reports. This report deals with the theoretical development of the multipath models, while [2] deals with the analysis of the measurement data.

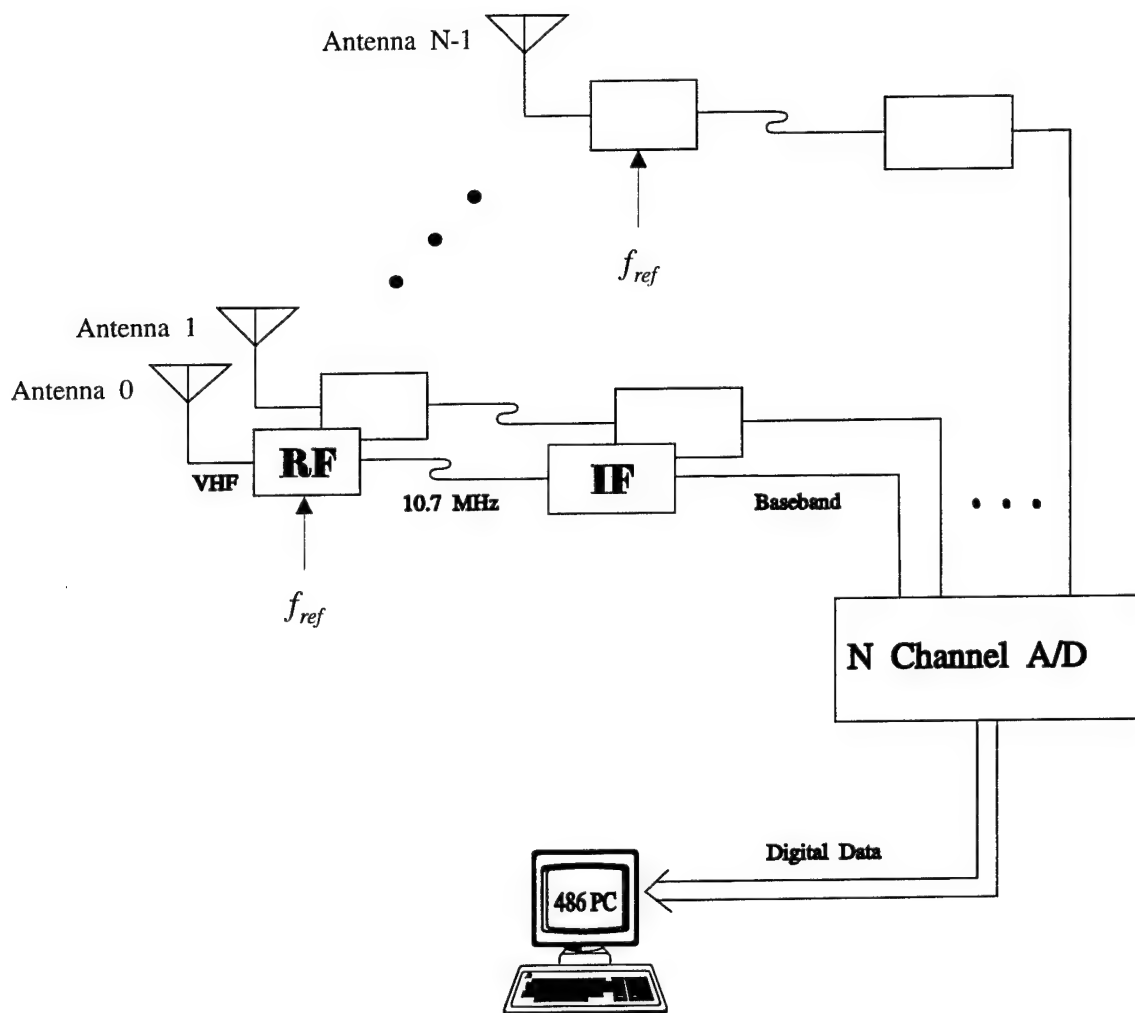


**Figure 1:** Experimental N channel DF system block diagram.

## 1.1 The Modelling Approach

The normal approach taken in propagation modelling is to estimate the expected values for the received signal based on modelling the surface using either known shapes or statistical surfaces (i.e. rough surfaces). For example, successive ridges along the signal path could be modelled using knife-edge diffraction techniques [3]. These approaches are often successful at predicting the average path loss as a function of transmitter position (i.e. the average path loss for the transmitter moved to various positions over a given area) but cannot predict fine-scale effects (i.e. the change in path loss as the transmitter is moved distances on the order of one meter). In this analysis, it is the fine-scale effects and the statistical nature of these effects which are of the most interest.

The failure of most propagation models to predict fine-scale effects is a function of the requirement for these models to provide useful information (i.e. expected path loss) without being too difficult to use. Consequently the constructive and destructive phase effects of competing signal paths are usually ignored to simplify processing. It is these phase effects which give rise to the fine-scale multipath effects.

Exact multipath effects could probably be modelled using approaches employed by electromagnetic software packages such as the Numerical Electromagnetics Code (NEC). However, these packages are normally used to predict antenna characteristics so that for the scale of the problem described here, the computer processing and memory requirements would be prohibitive. Additionally, exact sizes, positions, electrical properties of everything surrounding the signal path would have to be measured. Consequently, trying to model exact effects would not be practical.

The approach employed in this report is to break the terrain, or parts of the terrain, into very small pieces with dimensions on the order of a fraction of a wavelength. Each part can then be considered as a secondary or elemental reradiating source which, in turn, can be modelled in a very simple way. This is similar in most respects to Huygens' principle [4], and analogous to using digital signal processing to analyze analog signals.

To simplify the analysis, a number of assumptions and simplifications have been made. These include:

1. the transmit and receive antennas are isotropic,
2. refractive effects due to variations in air density are insignificant



3. vertical polarization only is considered, and
4. de-polarization effects can be ignored.

Of these assumptions, ignoring de-polarization effects has the greatest impact in the results. Including these effects would provide additional accuracy to the modelling but at the expense of considerably complicating the analysis, which is not considered warranted in this case.

Despite these assumptions and simplifications, the approach of subdividing the terrain still remains computationally intensive. For example, modelling the ground between the transmitter and receiver for ranges of several kilometers would require using an extremely large number of elemental reradiators which then becomes a daunting computational task. Consequently, rather than try to solve the entire multipath environment in this way, various simplified environments were explored which either allowed using a more manageable number of reradiators, or could be handled in a very computationally efficient way. From these explorations, analytical approaches were developed which could then be used to represent the simplified environments. More complex environments could then be represented by combining a number of these analytical approaches.

Central to the development of these analytical approaches is a proper understanding of their eventual intended purpose. This provides the basis for deciding which approximations can be made for the sake of computational simplicity, and which cannot. In this report, the main purpose for the development of the analytical approaches is to provide a better understanding of the various mechanisms which give rise to multipath, and to be able to produce a simulated environment which mimics the effects observed in the real world. There was no intention to be able to exactly predict real world results.

To illustrate the intended purpose, Figure 2a provides a measurement sample taken from multipath field trials described [2]. The measurement was taken from an experiment where a transmitter broadcast a CW signal at 62.5 MHz while slowly moving along a straight line. The receive system, called Osprey, was located approximately 2 km away from the transmitter in a position where the direct signal path was roughly perpendicular to the route followed by the transmitter. Figure 2a shows the received signal amplitude as a function of the distance travelled by the transmitter. Figure 2b is a simulation using the same transmitter-receiver geometry and assuming a large number of multipath sources (based on the model developed in Section 4.2) with dimensions on the order of one wavelength (4.8 meters). Figure 2c uses the same model but assumes the average

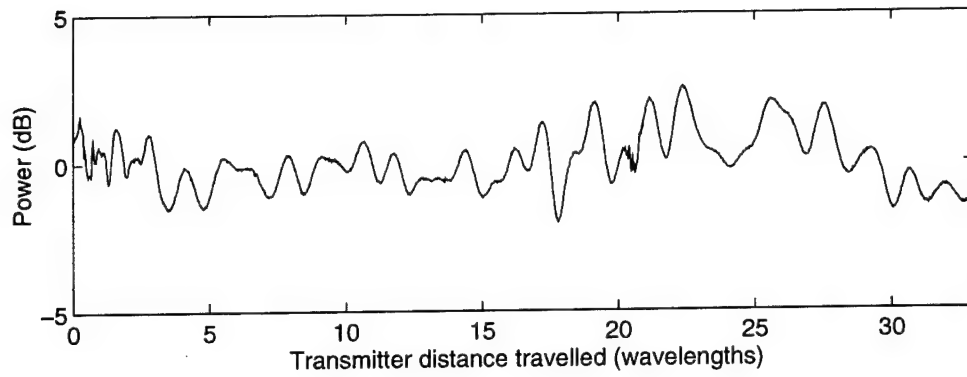
dimensions are on the order of five wavelengths. Although neither of the two simulated results exactly duplicate the actual result, Figure 2c better mimics the ripple behavior of the actual measurements, particularly in terms of the higher frequency content of the ripple, providing evidence that a significant portion of multipath was generated by objects with dimensions closer to one wavelength than four wavelengths.

An important assumption that was also used to produce simpler analytical expressions was the assumption that for terrestrial signal paths investigated in [2], large numbers of objects were typically involved in the production of multipath. This is based on field trial results, as discussed in Section 1.0, and visual surveys. Visually, the number of objects known to cause multipath that were scattered in and around the signal paths used in field trials was large (e.g. trees, bushes, fences, buildings, etc. – see [6] for a more extensive list of objects which cause multipath). Although not definitive proof, these observations suggest that assuming a large number of multipath sources is a very safe bet.

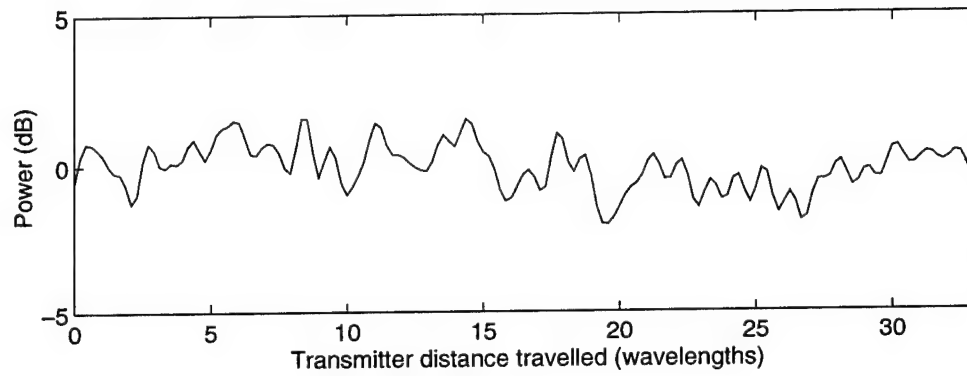
The advantage of this assumption is that since multipath is considered the result of contributions from a large number of objects, the characteristics that are the most important are the characteristics resulting from this collection of objects. The exact characteristics of each multipath source are then less important, and it is therefore only necessary to identify the most important characteristics which contribute to the collective effects.

## 1.2 Further Considerations

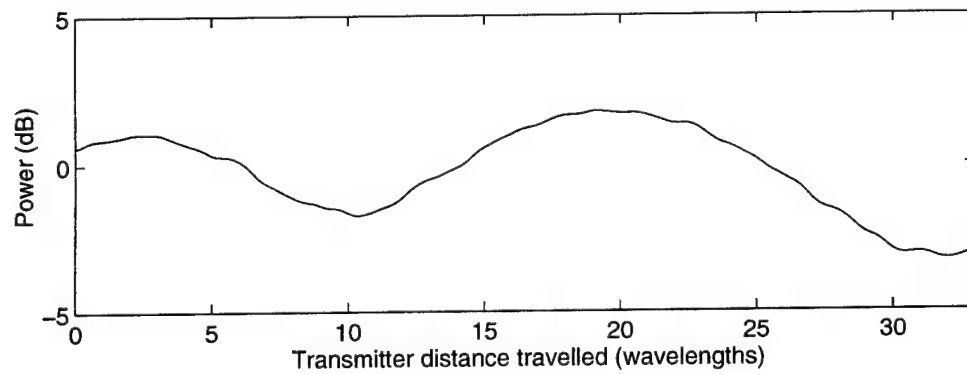
Before getting into a detailed mathematical analysis, it is useful to describe in more detail how the modelling with isotropics elements is done, and the limitations of this approach. To understand the approach that has been taken, it is useful to consider two simplifying examples of the real world environment. In the first example, the transmitter and receiver are on the ground and a few kilometers apart, the terrain is very flat, and the vegetation consists of scattered groves of trees and bushes. The signal arriving at the receiver will consist of the direct signal, plus a signal reflected off the ground as well as signals scattered off the vegetation. Since the ground is flat, it will likely be homogeneous (i.e. its electrical characteristics are the same everywhere), with the result that the ground reflected signal will be well behaved. In this case the ground could easily be modelled as a simple reflection plane. For the vegetation, a single tree or bush could be approximately modelled by a single large isotropic element, or more accurately modelled by subdividing



(a)



(b)



(c)

**Figure 2:** Signal power for a moving transmitter showing (a) actual measurements, and (b) simulated results for a large number of multipath sources with physical dimensions of one wavelength, and (c) four wavelengths.

the tree or bush into smaller parts and then modelling each part by separate appropriately sized isotropic elements.

In the second example, the transmitter and receiver are again a few kilometers apart, but vegetation is nonexistent and the ground is rolling. In this case the ground signal is not just a simple reflection, but reflections off many different parts of the ground. For modelling purposes, the ground surface itself is subdivided into many small sections, each section is then modelled by a suitably chosen isotropic element. The result is a huge grid of isotropic elements with elevation features identical to the actual ground.

Once the model has been setup, the next step is to compute the signal reradiated from each element. This requires solving for the signal incident on each isotropic element as the reradiated signal is directly proportional to this incident signal, or

$$s_{reradiated} = \beta s_{incident} \quad (1)$$

where  $\beta$  is the complex reradiation coefficient. The electromagnetic field would be related to these signals according to

$$s = \mu \varepsilon \quad (2)$$

where  $s$  represents either the incident or reradiated signal,  $\mu^2$  is the collection area of the isotropic element, and  $\varepsilon$  is the corresponding electric field. A similar real-world example would be the electrically short dipole which has a similar behaviour to an isotropic element, although its reradiation pattern is not isotropic. In the real-world example, the signals  $s_{reradiated}$  and  $s_{incident}$  would correspond to voltages setup in the antenna,  $\mu$  would correspond to the length of the antenna, and  $\beta$  would be related to the mismatch between antenna and freespace impedances.

Determining the incident signal for each isotropic element provides the greatest difficulty in this modelling approach, but once it has been done, the signal arriving at the receiver is simply the sum of the contributions from each source. For a receiving system consisting of an array of antennas, this summation would need to be done for each antenna. (Note that the calculation of the incident signals for each isotropic element need only be done once, however, irrespective of the number of receiving antennas).

Two obvious features of the isotropic model are the parameters  $\mu$  and  $\beta$ , whose choice will obviously affect the value of the reradiated signals. Since  $\mu^3$  will be directly proportional to the volume of the physical object being modelled, it's determination is relatively straightforward. The choice of  $\beta$  would ideally be based on the electrical properties of

the object being modelled as well, however, no attempt has been made to explore this relationship. This is because in many cases a value of  $\beta = -1$  is sufficient for modelling purposes, and where this value is not appropriate, a better value can be derived by comparing real data with simulation data and then adjusting  $\beta$  to get the best match. If the adjustment approach is used, simple logic can also be applied to ensure the values of  $\beta$  make sense.

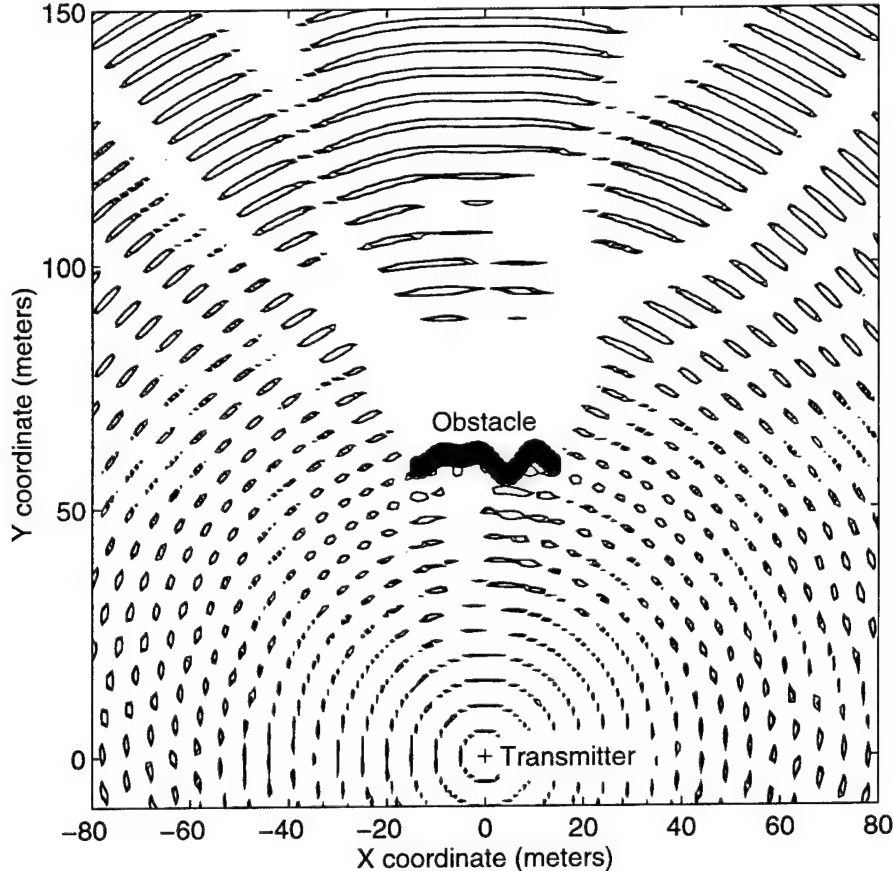


**Figure 3:** Overview of a signal impinging on a large obstacle

To understand when using  $\beta = -1$  is appropriate, irrespective of the electrical properties of the object being modelled, consider Figure 3. It shows a top view of a signal impinging on a large obstacle such as, for example, a row of trees, a fence, etc.. On the opposite side of the obstacle (the trailing edge), a shadow region forms (including diffraction effects) which disappears at some distance. At the trailing edge then, the electromagnetic field has dropped to virtually nothing. In modelling the obstacle, a large collection of isotropic sources could be used. The choice of  $\mu$  will clearly depend on the size of the isotropic element required, but the choice for  $\beta$  is not as clear. Noting, however, that the

electromagnetic field is near zero on the trailing edge then any isotropic element located on this edge will meet the condition

$$\mathcal{E}_{reradiated} + \mathcal{E}_{incident} \approx 0 \quad (3)$$

which is equivalent to

$$s_{reradiated} + s_{incident} \approx 0 \quad (4)$$

Given the relationship between the incident and reradiated signals (1) then

$$(1 + \beta)s_{incident} \approx 0 \quad (5)$$

which leads to  $\beta \approx -1$  assuming  $|s_{incident}| > 0$ . If  $|s_{incident}| \approx 0$  the choice of  $\beta$  is unimportant, i.e. choosing  $\beta = -1$  is still reasonable.

Letting  $\beta = -1$  will not be appropriate for all situations. On the other side of the obstacle in Figure 3 (on the side incident to the transmitter signal – the leading edge), a value of  $\beta = -1$  would result in a strong reflection, i.e. the obstacle would act like a bumpy reflector. However, if the obstacle absorbs some of the signal energy (e.g. conversion to heat energy – induced currents in the obstacle could cause ohmic heating) then the signal reflection would be weaker than expected. In this case it is more appropriate to use a smaller value for  $|\beta|$ . Additionally, the dielectric constant of the obstacle will affect the phase of the reflected signal which results in  $\beta$  taking on an imaginary component. Obviously in the reflection case it is more accurate to try and determine  $\beta$  from measured data, although  $\beta = -1$  provides a reasonable starting point.

The major failing of the isotropic element model is the inability to accurately model losses. For example a perfectly matched dipole will not produce any reflected signal. A shadow zone will still be setup since the dipole has extracted power from the incoming signal (i.e. the electric field signal is converted to an electrical signal). In the case of the isotropic element, there is no such mechanism to convert the incoming signal to another form of energy, only a mechanism to redirect the signal flow. This flaw could be overcome by changing the antenna pattern so that it is no longer isotropic. However, this introduces considerable complications to the analysis which were not considered warranted given the main purpose of the modelling discussed in this report.

To justify the last point, consider the fact that the main effects of a multipath source can be classified as shadowing or reflection. For a single multipath source, these two mechanisms are mutually exclusive from the perspective of the receiver (i.e. the receiver

can be affected by shadowing or reflection, but not both simultaneously). For multipath sources located between the transmitter and receiver, and near the signal path (ignoring the ground for the moment), shadowing will be the dominant mechanism, so that for modelling purposes  $\beta = -1$  is suitable. This results in strong reflected signals for the modelled multipath sources, but since these reflections will generally propagate in directions away from the receiver they will be of little importance. It is possible that multiply reflected signals could be directed towards the receiver, but these effects will be minor and can also be ignored.

Outside this shadow region, reflections are more likely to be the dominant mechanism. In this case, the choice of  $\beta$  will be made by comparing simulations with real measurements, as discussed previously, and will incorporate the effect of losses. In the case of high losses the choice of  $\beta$  may no longer be appropriate for the shadows, but since these shadows will be directed away from the receiver, this error is not important.

In the case of the ground, reflections will be very important regardless of location. For a flat ground with varying dielectric properties, reflection will be the only mechanism so  $\beta$  is chosen accordingly (if  $\beta \neq -1$  this will result in a signal below the surface, but since the receiver is above the surface, this signal can be ignored). For a ground which is not flat, both reflections and shadowing are possible mechanisms. For this, modelling is restricted to the case where the elevation varies but the surface is perfectly reflecting ( $\beta = -1$ ). In other words, terrain with both varying electrical characteristics and varying elevation is not addressed, although the effects could reasonably be inferred from the ground models that are developed in this report.

One final comment regarding the definition of multipath used in this report. The general definition used here is

$$S_{\text{multipath}} = S_{\text{receiver}} - S_{\text{ideal}} \quad (6)$$

In the freespace case, the ideal signal is the direct transmitter to receiver signal. In this case, multipath will be the signal that is reradiated, reflected, etc., by objects around the signal path. In the terrestrial case, the definition for the ideal signal used in this report is slightly different. Since all terrestrial signal paths will involve ground reflections, the ideal terrestrial signal is defined as the signal that occurs when the ground is perfectly flat and perfectly reflecting. Mathematically,

$$S_{\text{ideal}} = S_{\text{direct}} + S_{\text{reflected}} \quad (7)$$

Although the ideal ground reflected signal is technically a multipath signal, for terrestrial problems the ground reflected signal is inescapable so that the above definition is more analytically useful.

In the rest of this report, many of the discussions become embroiled in complex mathematical derivations. Given the rather random nature of the real world, and that the aim of this research to emulate but not duplicate real world effects, it might at first seem that the mathematics becomes unnecessarily involved. However, the detail is required in order to establish the theoretical underpinnings of the models, their limitations, and when various simplifying assumptions are justified.

To this end, a major portion of this report focuses on developing the mathematical theory of the isotropic model in a slow and determined manner. The development of the model may at first seem a little detached from the real-world, however this is necessary in order to examine and understand the various aspects of the model in more detail. At the end of this development, simulation examples are provided to illustrate how the various models and modelling approaches can be applied to real world problems.

The rest of this report is divided into six main parts. In Section 2.0, the isotropic reradiator in freespace is introduced, followed by an examination of a collection of reradiators in freespace. Based on this examination, size of the multipath source is shown to be an important characteristic, while shape is found to be relatively less important except when reflections occur. In Section 3.0, the effects of coupling are examined. Since the inclusion of coupling effects dramatically increases the computational requirements of modelling, ways of reducing the computations are also discussed. In Section 4.0, the effects of the ground on path loss and coupling are examined. This examination includes vegetation and terrain effects, as well as the effect of a nonhomogeneous ground. In Section 5.0, the models introduced in the three previous sections are summarized and their limitations noted. In Section 6.0, two examples are provided illustrating how the models could be used to investigate and better understand effects observed in real-world measurements. Finally, in Section 7.0, the concluding remarks are presented.



## 2.0 MULTIPATH SOURCE CHARACTERISTICS

In this part, multipath sources are modelled by dividing the source up into elemental isotropic reradiators. The discussion starts with the introduction of a simple mathematical model of a single elemental reradiator in freespace and its affect on a transmitter signal. This model is then evolved to include the effects of a collection of elemental reradiators in freespace. Using these collections to represent various shaped multipath sources, the characteristics of multipath sources are then analyzed and discussed. In presenting the effects of shape, shapes are limited to simple two-dimensional geometric shapes for convenience, however, the analysis could be easily extended to include real world objects such as bushes, trees, buildings, etc.

### 2.1 The Discrete Reradiator

In this section, the equations which describe the behaviour of an isotropic reradiating element are derived. Since these reradiators first receive an external signal which is subsequently retransmitted, it is useful to consider the receive response of the reradiator first.

For a radiating isotropic source in freespace, the radio wave expands in a spherical wave with the source at the center. Using an optics approach, the power extracted by a receiving antenna at a distance  $r$  can be computed by considering the area of the spherical wave intercepted by the antenna compared to the total area  $4\pi r^2$  of the spherical wave. The received power will be given by,

$$P_{rcvr} = P_{tx} \frac{\mu^2}{4\pi r^2} \quad (8)$$

where  $P_{rcvr}$  is the received signal power,  $P_{tx}$  is the power radiated by the transmitter,  $\mu^2$  is the effective collecting area of the receiving antenna, and it is assumed  $4\pi r^2 \gg \mu^2$ .

The complex amplitude  $s_{rcvr}$  of the received signal can also be related to that of the amplitude of the transmitted signal  $s_{tx}$  using the fact that  $|s| \propto P^{\frac{1}{2}}$  (where  $s$  and  $P$  represent signal amplitude and power respectively) and the phase delay is a function of the path length  $r$ . This leads to the result

$$s_{rcvr} = \frac{s_{tx}}{r} \left( \frac{\mu}{2\sqrt{\pi}} \right) e^{-j\frac{2\pi}{\lambda}r} \quad (9)$$

where it is again assumed that  $4\pi r^2 \gg \mu^2$  or equivalently  $r \gg \mu/2\sqrt{\pi}$ .

If the condition on  $r$  is not met, nearfield effects begin to affect the results and the above equations may be considered approximations only. In the extreme case where  $r < \mu/2\sqrt{\pi}$ , the above expressions break down completely since they predict that  $|s_{rcvr}| > |s_{tx}|$  and  $P_{rcvr} > P_{tx}$  which clearly makes no sense. In reality, to satisfy the law of physics, nearfield effects will ensure that the relationship  $|s_{rcvr}| \leq |s_{tx}|$  is always true. The exact nature of these nearfield effects will be dependent on the actual object being modelled (i.e. its shape, electrical properties, etc.) but can be approximated by

$$s_{rcvr} = s_{tx} e^{-j\frac{2\pi}{\lambda}r} \quad \text{for } r < \frac{\mu}{2\sqrt{\pi}} \quad (10)$$

More realistic nearfield equations have been tested but were found to have no effect on the results presented in this report.

Expressions (9) and (10) can be represented by the more general expression

$$s_{rcvr} = s_{tx} \rho(r) \quad (11)$$

where  $\rho(r)$  is called the *freespace* attenuation function in this report and represents the effect of path length on both amplitude and phase of the signal. For a discrete reradiator in freespace, the attenuation function is given by

$$\rho_{\alpha}(r) = \begin{cases} \frac{\mu}{2\sqrt{\pi}r} e^{-j\frac{2\pi}{\lambda}r} & \text{if } r \geq \frac{\mu}{2\sqrt{\pi}} \\ e^{-j\frac{2\pi}{\lambda}r} & \text{otherwise} \end{cases} \quad (12)$$

where the subscript  $\alpha$  has been added to identify it as the *freespace* attenuation function. The corresponding path loss is given by  $|\rho_{\alpha}(r)|^2$ . Other forms of the attenuation function (i.e. attenuation over a reflecting ground) are discussed in Sections 4.2 and 4.3.

If the receiving element is a reradiator, the above expression can be modified slightly to yield

$$s_{incident} = s_{tx} \rho_{\alpha m}(r_a) \quad (13)$$

where  $\rho_{\alpha m}(\cdot)$  is the freespace attenuation expression for the transmitter-reradiator path using  $\mu^2 = \mu_m^2$  for the collection area of the reradiator, and  $r_a$  is the range from the transmitter to the reradiator.

Once the signal has been received, it is reradiated. This can be introduced into the model by incorporating a complex reradiation coefficient  $\beta$  such that  $|\beta| \leq 1$ . The reradiated signal  $s_m$  measured at the reradiator will then be

$$s_m = s_{tx} \beta \rho_{\alpha m}(r_a) \quad (14)$$

The portion of the reradiated signal that arrives at the receiver can be determined by applying (13) to (14). Since this will be the multipath signal, the final result is given by,

$$s_{mult} = s_{tx} \beta \rho_{\alpha m}(r_a) \rho_{\alpha r}(r_b) \quad (15)$$

where  $\rho_{\alpha r}(\cdot)$  is the freespace attenuation expression for the reradiator-receiver path using  $\mu^2 = \mu_r^2$  for the collection area of the receiving antenna, and  $r_b$  is the range from the reradiator to the transmitter. A distinction has made between  $\rho_{\alpha r}(\cdot)$  and  $\rho_{\alpha m}(\cdot)$  since the collecting areas of the reradiating elements and the receiving antenna ( $\mu_m^2$  and  $\mu_r^2$  respectively) may be different.

For simplicity, the receiving antenna is treated as matched as well as isotropic (i.e. the size of the antenna is chosen so that no special matching network would be required). Under these conditions the effective collecting area is given by [7]

$$\mu_r^2 = \frac{\lambda^2}{4\pi} \quad (16)$$

## 2.2 Collections of Reradiators

A number of useful characteristics can be derived by simulating the effects of more complex multipath sources using a collection of isotropic sources. The received multipath signal will then be the sum of all the individual contributors

$$s_{mult} = \sum_{k=1}^N s_{mult_k} \quad (17)$$

where  $N$  is the total number of reradiators making up the multipath source and the subscript  $k$  is used to distinguish the contribution from individual reradiators. Applying (15) to each reradiator yields

$$s_{mult} = s_{tx} \beta \sum_{k=1}^N \rho_{\alpha m}(r_{ak}) \rho_{\alpha r}(r_{bk}) \quad (18)$$

The assumption is made here that the multipath source is homogeneous (its electrical properties are the same everywhere) so that  $\beta$  is the same for all the reradiators. Nonhomogeneous multipath sources can be modelled by breaking the source into small enough parts that each part is homogeneous.

To simplify later derivations, it is useful to redefine the path lengths  $r_a$  and  $r_b$  as the distance from the transmitter to the center of the multipath source and the distance from the center of the multipath source to the receiver, respectively. A reference signal can then be defined as

$$s_{ref} = s_{tx} \rho_{\alpha m}(r_a) \rho_{\alpha r}(r_b) \quad (19)$$

Additionally further simplifications result if  $r_a, r_b \gg D_{max}$  where  $D_{max}$  is the largest physical dimension of the multipath source. In this case  $|\rho_{\alpha m}(r_{ak})| \approx |\rho_{\alpha m}(r_a)|$  and  $|\rho_{\alpha r}(r_{bk})| \approx |\rho_{\alpha r}(r_b)|$  with the result that (18) can be rewritten as

$$s_{mult} = s_{ref} \beta \sum_{k=1}^N e^{-j \frac{2\pi}{\lambda} (r_{ak} - r_a + r_{bk} - r_b)} \quad (20)$$

Using the Cartesian coordinate system shown in Figure 4, where the origin corresponds to the center of the multipath source, then the following approximations can be used

$$\begin{aligned} r_{ak} &\approx r_a - (x_k \sin \phi_a \cos \psi_a + y_k \cos \phi_a \cos \psi_a + z_k \sin \psi_a) \\ r_{bk} &\approx r_b - (x_k \sin \phi_b \cos \psi_b + y_k \cos \phi_b \cos \psi_b + z_k \sin \psi_b) \end{aligned} \quad (21)$$

where  $\phi_a$  and  $\phi_b$  are the transmitter and receiver direction angles measured on the X-Y plane with respect to the X-axis, and  $\psi_a$  and  $\psi_b$  are the corresponding direction angles measured with respect to the Z-axis. Without loss of generality, the X-Y plane is assumed to be oriented so that the transmitter lies on the negative Y-axis ( $\phi_a = 180^\circ$  and  $\psi_a = 0^\circ$ ) as shown in the figure. Defining  $\phi = \phi_b$  and  $\psi = \psi_b$ , and using the preceding simplifications, (20) becomes

$$s_{mult} = s_{ref} \beta \sum_{k=1}^N e^{j \frac{2\pi}{\lambda} (x_k \sin \phi \cos \psi - y_k (1 - \cos \phi \cos \psi) + z_k \sin \psi)} \quad (22)$$

Since, in terrestrial applications, the X-Y plane will generally be approximately parallel to the ground, then  $\phi$  and  $\psi$  are respectively called the azimuth angle and the elevation angle (of the receiver) here.

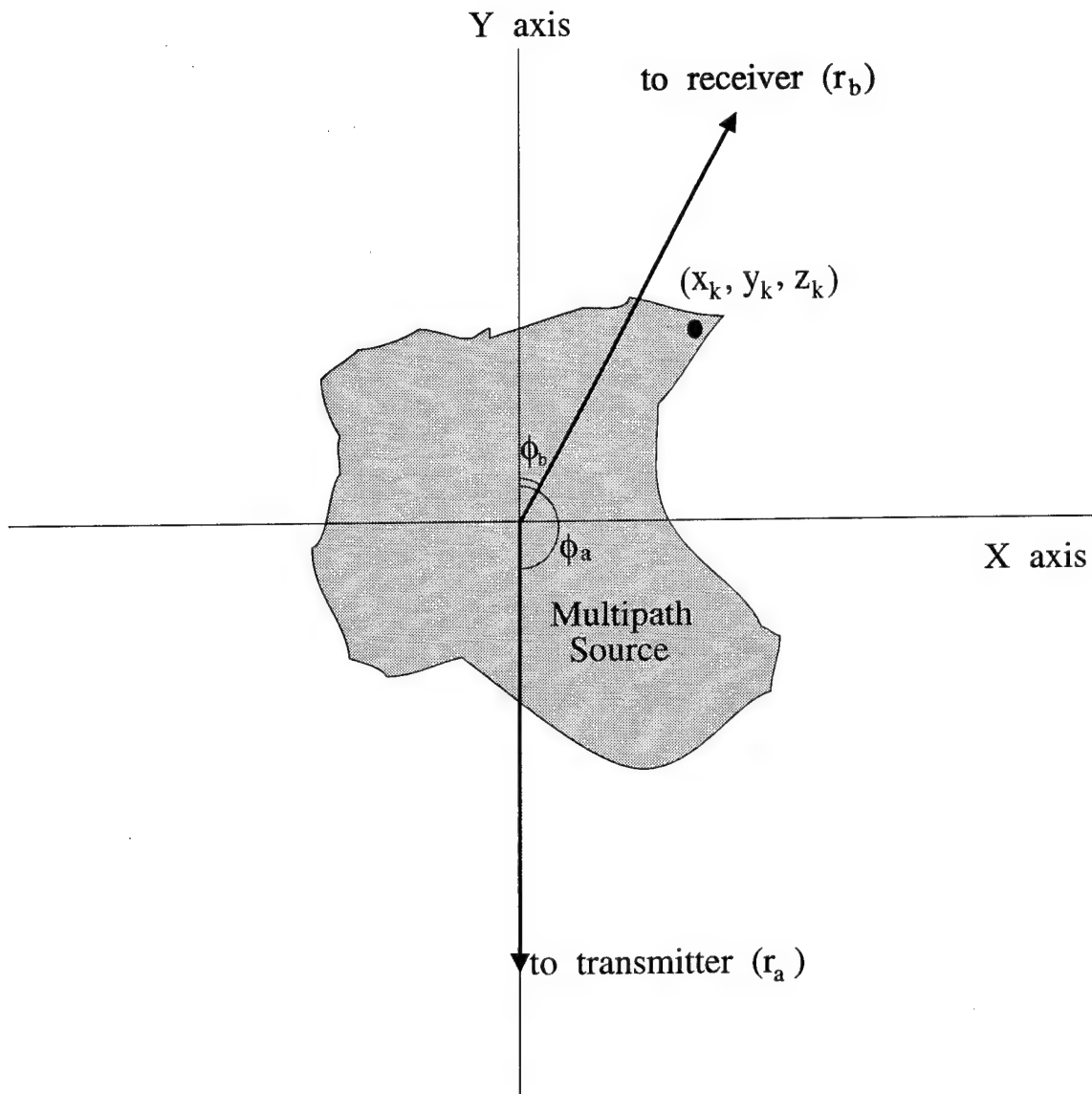


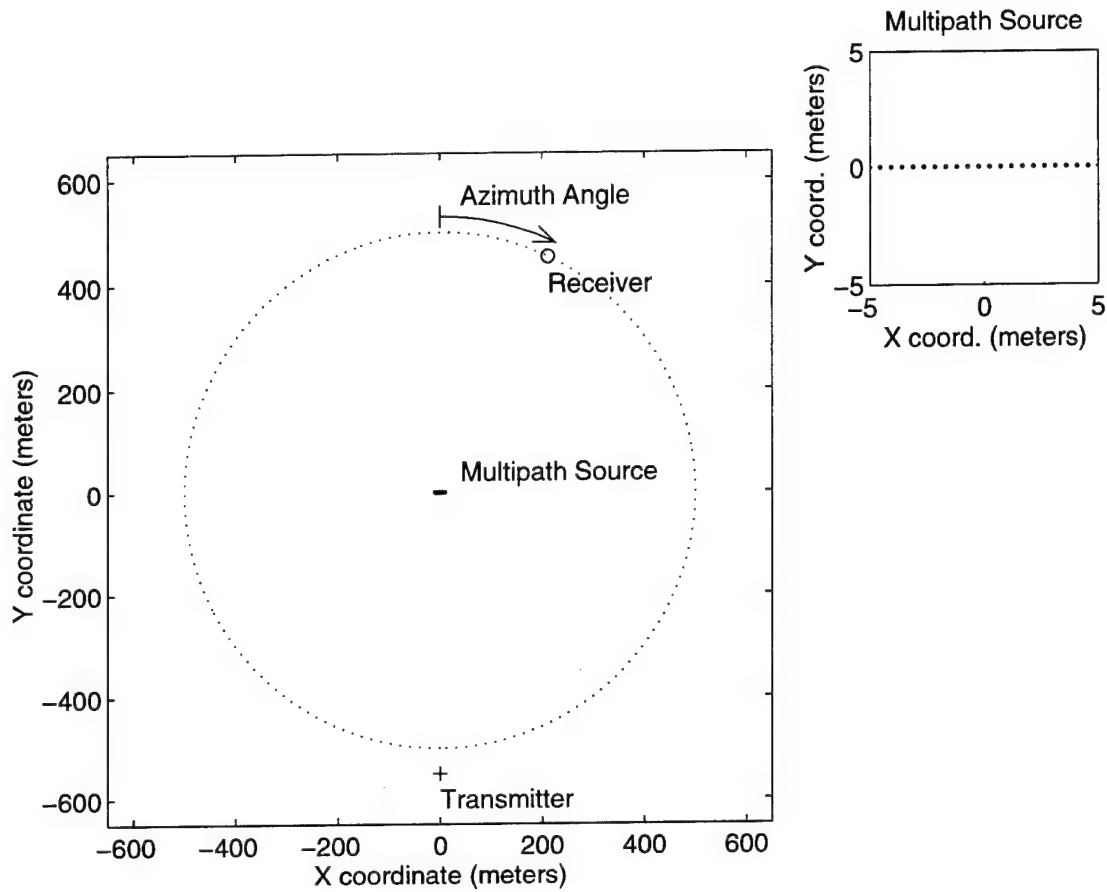
**Figure 4:** Cartesian coordinate system representation for multipath source position. The Z-axis (not shown) projects upwards normal to this page.

### 2.3 Characterizing Multipath Sources

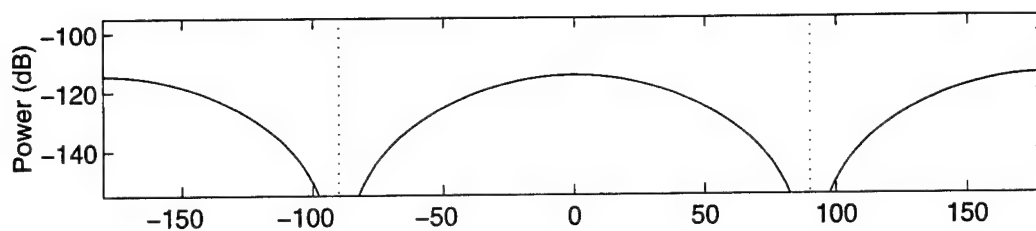
Various characteristics can be inferred from (22), however, before performing any further mathematical manipulations, it is useful to first examine some simulation results in order to provide an idea of which characteristics are the most important. Figure 5 shows the geometry of a simulation experiment carried out using (18). In this experiment the receiver was moved in a circle around a multipath source while the transmitter position was kept fixed. The transmitter, receiver, and multipath source were all placed on the X-Y plane. The multipath source consisted of a linear array of  $N = 10$  reradiators (see blow-up in the upper right hand corner of the figure) where the spacing  $d$  between adjacent reradiators was chosen to be a small fraction of a wavelength, namely,  $d = 0.1\lambda$  m. Since coupling effects are not taken into account here,  $\mu_m$  was chosen so that each reradiator represents a contiguous area, neither overlapping nor spread apart. This leads to  $\mu_m = d$ . Using a transmitter frequency of 62.5 MHz, then  $\lambda = 4.8$  m and  $d = \mu = 0.48$  m. A value of  $\beta = -1$  was also chosen.

Figure 6a shows the power of the multipath signal measured as a function of the receiver azimuth angle. Figure 6b shows the received power for the same experiment except using a line array of 20 reradiators with the same spacing, while Figure 6c shows the received power for a line array of 40 reradiators (also with the same spacing). Figure 7 shows the corresponding received signal phases measured relative to  $s_{ref}/\beta$  (i.e. the phase of the summation term in (20)).

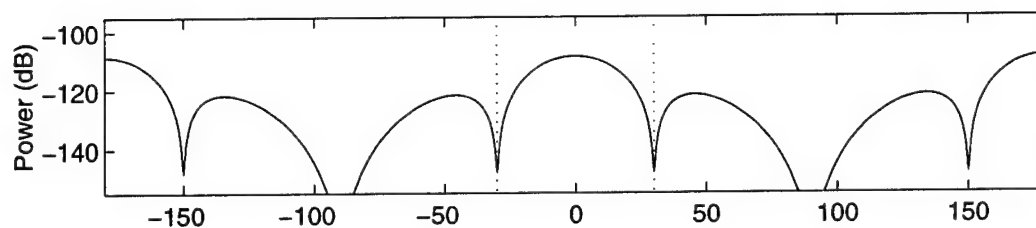
Examining the three cases shown in Figures 6 and 7 the outputs have a lobed structure (where adjacent lobes are separated by nulls) with the two largest lobes lying in the directions  $0^\circ$  and  $180^\circ$ . In this report, the lobe at  $0^\circ$  is called the main beam and would correspond to the electromagnetic shadow cast by the multipath source. Lobes of comparable power (such as the one at  $180^\circ$ ) but in different directions are called reflection beams. In beamformer terminology, the remaining lobes are called sidelobes while in optics they are called diffraction lobes. In any case, since most of the multipath power will be concentrated in the main and reflection beams, most of the multipath effects observed by the receiver will be due to these two beams. Hence characterizing these beams goes a long way towards providing an effective means of characterizing the most important features of a multipath source. To this end, the maximum power of the main beam, its beamwidth, and the phase variation across the beam are investigated in detail in Sections 2.3.1-2.3.3, while the corresponding characteristics of the reflection beam are dealt with in Section 2.3.4. Finally, in Section 2.3.5 the general notation used in this report for the



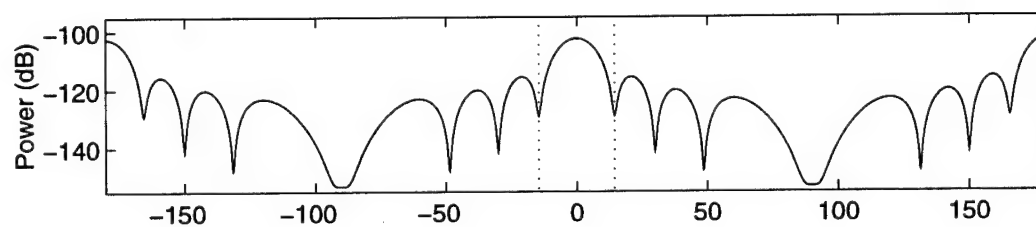
**Figure 5:** Geometry of simulation experiment to determine multipath source output as a function of receiver azimuth (as shown in large plot). Small plot at upper right is a  $10\text{m} \times 10\text{m}$  blow-up showing the geometry of the multipath source. Dots represent the positions of individual isotropic reradiators in this blow-up.



(a)



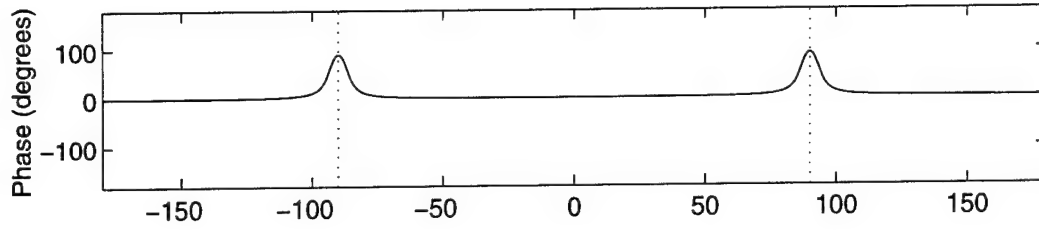
(b)



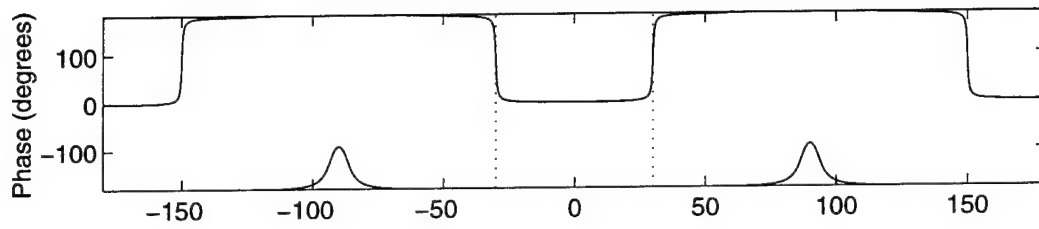
(c)

**Figure 6:** Multipath signal power as a function of receiver azimuth angle for multipath line sources represented (a) 10 reradiators, (b) 20 reradiators, and (c) 40 reradiators.

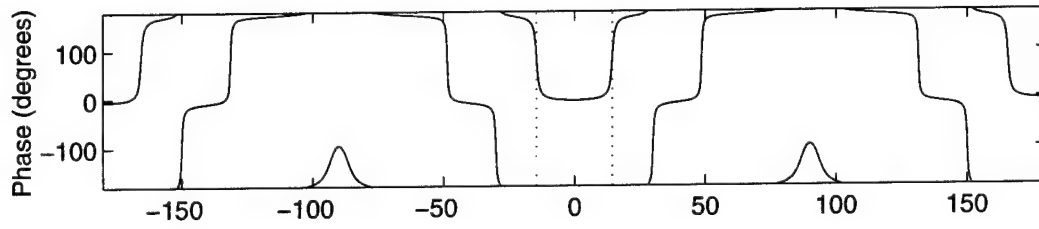




(a)



(b)



(c)

**Figure 7:** Multipath signal phase as a function of receiver azimuth angle for multipath line sources represented (a) 10 reradiators, (b) 20 reradiators, and (c) 40 reradiators.

multipath source model is introduced.

### 2.3.1 Beam Power

The power of the received multipath signal is defined here as

$$P = |s_{mr}|^2 \quad (23)$$

Inspecting (22), power is clearly maximized when the amplitude of the summation term

$$\sum_{k=1}^N e^{j\frac{2\pi}{\lambda}(x_k \sin \phi \cos \psi - y_k(1 - \cos \phi \cos \psi) + z_k \sin \psi)} \quad (24)$$

is maximized. Since this term represents the sum of a series of complex values, each with unit amplitude, the maximum possible amplitude occurs when the summation terms all have the same phase. This will always be true for  $\phi = 0$  and  $\psi = 0$  (the main beam direction) and possibly true for other azimuth and elevation angles depending on the shape of the multipath source (e.g. for the line sources simulated in Figure 6, a strong reflection beam occurs at  $\phi = 180^\circ$ ). For these directions, the amplitude of the summation term is  $N$  and the corresponding power given by

$$P_m = |s_{ref}\beta N|^2 = \left(s_{tx}\beta \frac{N\mu_m\mu_r}{4\pi r_a r_b}\right)^2 \quad (25)$$

### 2.3.2 Beamwidth

The null beamwidth of the main beam with respect to  $\phi$ , or the azimuth beamwidth, is the angular distance measured between the two closest nulls straddling the azimuth angle  $\phi = 0^\circ$  while keeping the elevation angle fixed at  $\psi = 0$ . In Figure 6, for example, the azimuth beamwidth is marked by the dotted lines. The null beamwidth of the beam with respect to  $\psi$ , or the elevation beamwidth, is defined in the same way except that the azimuth is fixed at  $\phi = 0$ . By symmetry, the azimuth and elevation beamwidths can be analyzed in the same manner so, for simplicity, the main discussion is limited to the azimuth beamwidth. The corresponding results for the elevation beamwidth are then inferred at the end of this discussion.

The null beamwidth of the main beam provides a measure of how much dispersion

occurs in the reradiating beam (the greater the beamwidth the greater the dispersion and the lower the power that is redirected towards the receiver). The nulls occur when  $s_m = 0$  which, in azimuth, corresponds to

$$\sum_{k=1}^N e^{j \frac{2\pi}{\lambda} (x_k \sin \phi - y_k (1 - \cos \phi))} = 0 \quad (26)$$

where the fact that  $\psi = 0^\circ$  was used. The solution to the above expression can be determined geometrically by representing each summation term as a unit vector on the complex plane. For  $\phi = 0$ , these vectors are all aligned with the real axis, as illustrated in Figure 8a (using the same array as used to produce Figure 6), which maximizes the amplitude of the summation term. As  $\phi$  is increased, these vectors spread out (in terms of the phase angle) on the complex plane (Figure 8b) and the summation amplitude decreases. As the azimuth is increased further, the spreading increases until the vectors cancel each other out (Figure 8c) and a null occurs. In this last state, the vectors can be seen to have achieved a state of “balance”.

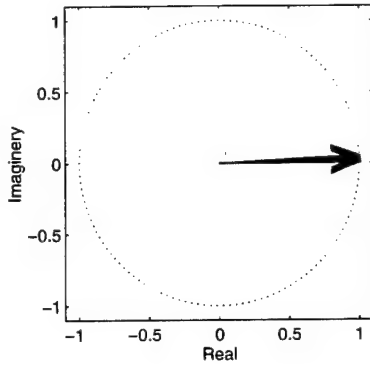
To provide a better understanding of the relationship between multipath shape and beamwidth, it is useful to examine the phase angles of the summation terms in more detail. For a fixed direction  $\phi = \phi'$ , the relationship between phase  $\theta$  and reradiator position  $(x, y)$  is given by

$$\theta = \frac{2\pi}{\lambda} (x \sin \phi' - y(1 - \cos \phi')) \quad (27)$$

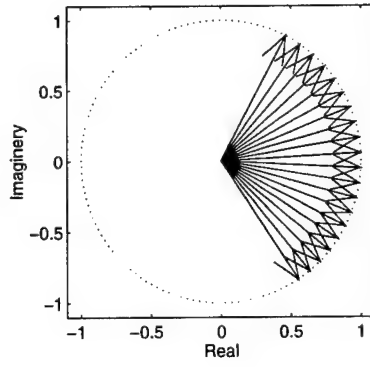
The above expression represents a plane in 3 dimensions,  $(x, y, \theta)$ , of which two examples are plotted in Figure 9. The contour lines in the figure represent lines of constant phase  $\theta$ . The zero-phase ( $\theta = 0^\circ$ ) contour line can be expressed as

$$x \sin \phi' - y(1 - \cos \phi') = 0 \quad (28)$$

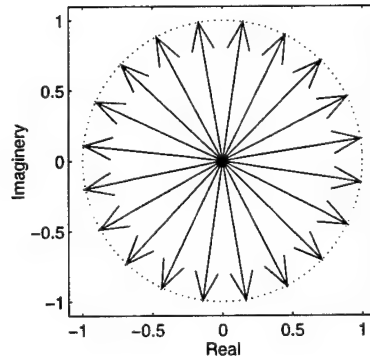
Based on the two expressions above, as well as Figure 9, it can be stated that the phase for any position is proportional to the perpendicular distance of the position from the zero-phase line. Using this concept, it is now possible to analyze various multipath shapes in more detail. In particular, three different multipath sources representing different extremes in shape will be analyzed. Note that these shapes were not chosen due to any correspondence to real-world shapes, but were chosen to illustrate certain concepts which can then be applied to a large variety of shapes. Additionally, the shapes were all chosen to be flat since from (27),  $z$  has no effect on the phase, and consequently no effect on the



(a)

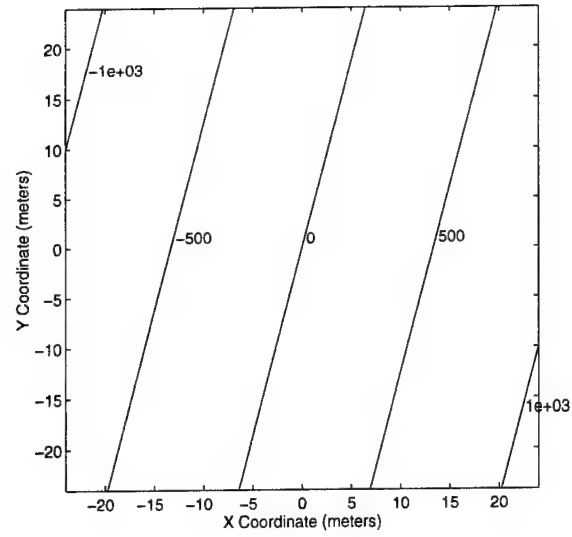


(b)

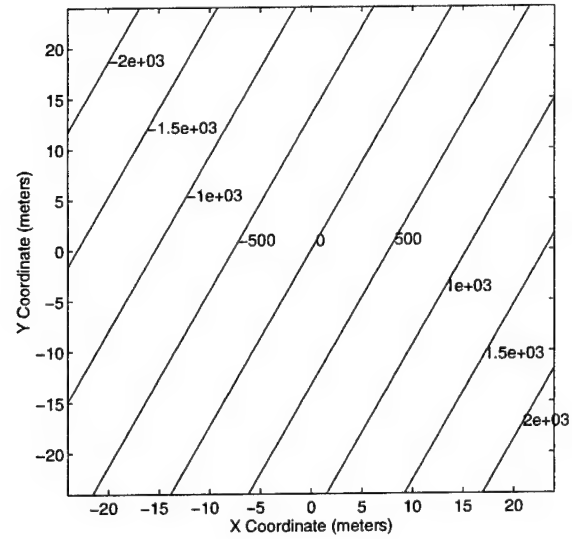


(c)

**Figure 8:** Vector representation of summation terms for a line source ( $N = 20$ ) and for receiver azimuth angles of (a)  $0^\circ$ , (b)  $10^\circ$ , and (c)  $30^\circ$ .



(a)



(b)

**Figure 9:** Map showing phase contours (labeled in degrees) as a function of position relative to the center of the multipath source at  $(x, y) = (0, 0)$  and for a receiver azimuth of (a)  $30^\circ$ , and (b)  $60^\circ$ .

azimuth beamwidth (it would, however, effect the elevation beamwidth).

The first shape is again the line source example. Figure 10a shows a case with  $N = 20$  with the zero-phase line drawn for  $\phi' = 30^\circ$ . This particular receiver azimuth corresponds to the main beam null marked by the dotted line in Figure 10b. It is quite evident that the perpendicular distance from the zero-phase line to consecutive reradiators varies in a linear manner. This will be true regardless of the orientation of the line source or the direction  $\phi'$ . To achieve a state of balance as discussed previously, the phases must be evenly spread through  $360^\circ$  as in Figure 8c. This leads to the result

$$\Delta_\theta = 2\pi \frac{N-1}{N} \quad \text{radians} \quad (29)$$

where  $\Delta_\theta$  is the difference between the maximum and minimum reradiator phase, or

$$\Delta_\theta = \max\{\theta_0, \dots, \theta_{N-1}\} - \min\{\theta_0, \dots, \theta_{N-1}\} \quad (30)$$

with  $\theta_k$  representing the phase of the  $k^{\text{th}}$  reradiator. In the real world, multipath sources are generally continuous which can best be modelled as  $N \rightarrow \infty$ . Hence for a continuous line source

$$\Delta_\theta = 2\pi \quad \text{radians} \quad (31)$$

The above expression will also be true for any shape which is uniformly distributed with respect to the zero-phase line of a main beam null.

The second shape to be considered is the dumbbell shown in Figure 11a. The zero-phase line for  $\phi' = 27.2^\circ$  has also been drawn. This receiver bearing corresponds to the main beam null marked by the dotted line in Figure 11b. From the relationship of the zero-phase line to the position of the reradiators, it is possible to predict that the phases of the summation terms will be non-uniformly spread with the phases concentrated towards the minimum and maximum values. This is verified by the vector diagram shown in Figure 12 with two groups of phase terms centered around phase angles of approximately  $-\pi/2$  and  $\pi/2$ . In this case, the total spread in the balanced state will be less than for the line source but still great enough that balancing can occur (i.e. the minimum spread will be  $\pi$ ). Therefore, for a multipath source with the main reradiation near the ends and away from the zero-phase line,

$$\pi \leq \Delta_\theta < 2\pi \quad (32)$$

The concentration of the phase angles about  $-\pi/2$  and  $\pi/2$  corresponds to the two concentrations of reradiators at opposite ends of the dumbbell shape. The farther apart the

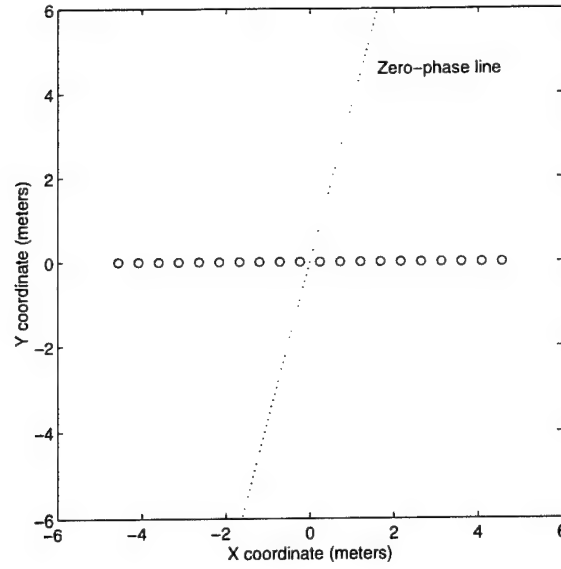


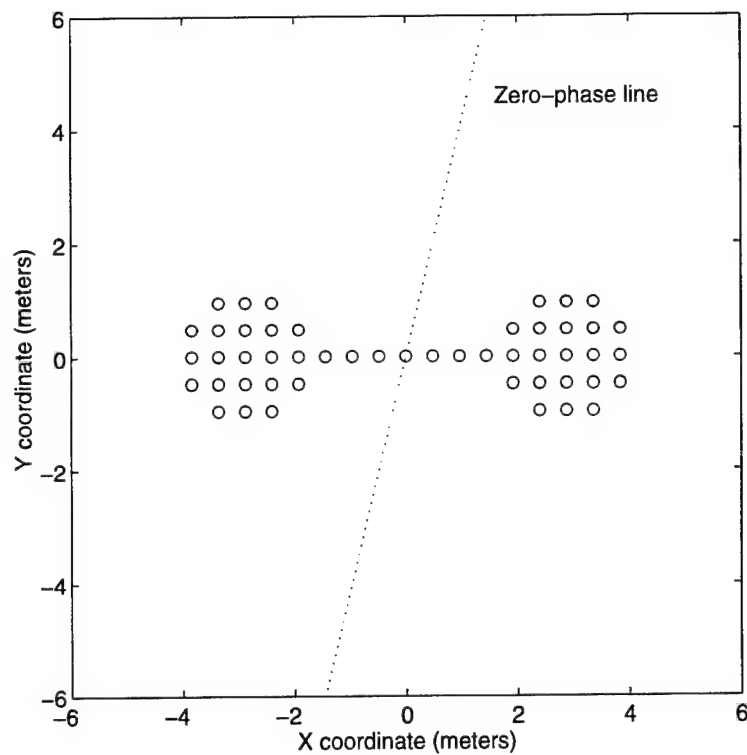
**Figure 10:** Geometry of line multipath source (open circles) and zero-phase line (dotted line) for  $\phi' = 30^\circ$ .

two concentrations are relative to the areas occupied by the reradiators, the closer  $\Delta_\theta$  moves towards  $\pi$ . The limiting case ( $\Delta_\theta = \pi$ ) is achieved for two reradiators.

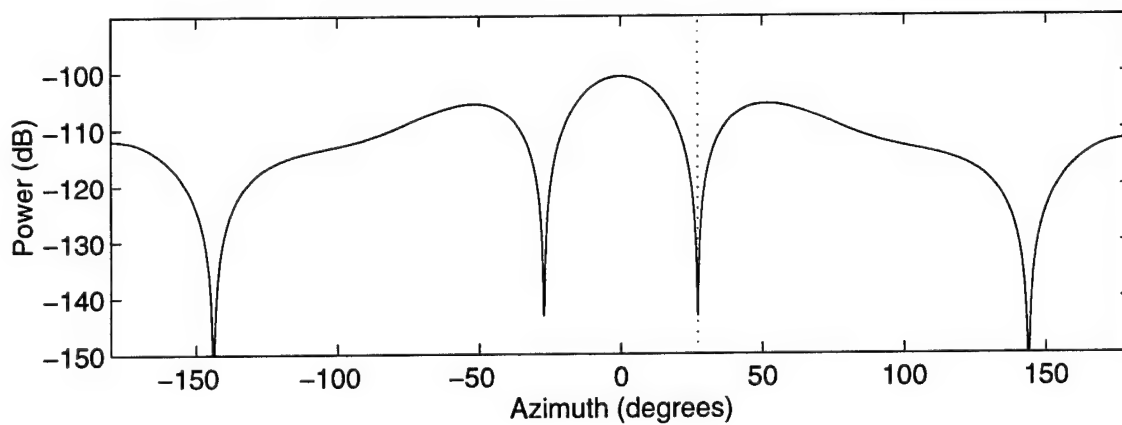
The third shape is the bent cross shown in Figure 13a. The zero-phase line is shown for  $\phi' = 43.2^\circ$ , the receiver azimuth of the null marked in Figure 13b. Note that the lack of symmetry of this multipath shape about the Y-axis results in an asymmetric power plot with respect to  $\phi = 0^\circ$ . The bent arm of the cross was purposely chosen to nearly align with the zero-phase line corresponding to the null so that the phase terms would be non-uniformly spread with a large concentration around  $\omega = 0$ . By inspection, it might be expected that the total spread of the summation term phases in the balanced state would exceed the spread for the line source in order to compensate for the concentration of phases near 0. This is indeed the case, as shown in Figure 14 where the dashed arrows indicate terms that have wrapped around (exceeded  $\pm\pi$ ). Therefore, for a source with the main concentration of reradiation near the zero-phase line

$$\Delta_\theta > 2\pi \quad (33)$$

In this example, an upper limit can be placed on  $\Delta_\theta$  as well. For example, phase terms where  $\frac{3}{2}\pi < |\theta_k| < \frac{5}{2}\pi$  for  $k = 0, 1, \dots, N-1$  no longer serve to counterbalance the effects of the phase terms concentrated around 0. Assuming the concentration of phase terms is



(a)



(b)

**Figure 11:** Dumbbell multipath source showing (a) geometry and zero-phase line for  $\phi' = 27.2^\circ$ , and (b) multipath power as a function of  $\phi$ .



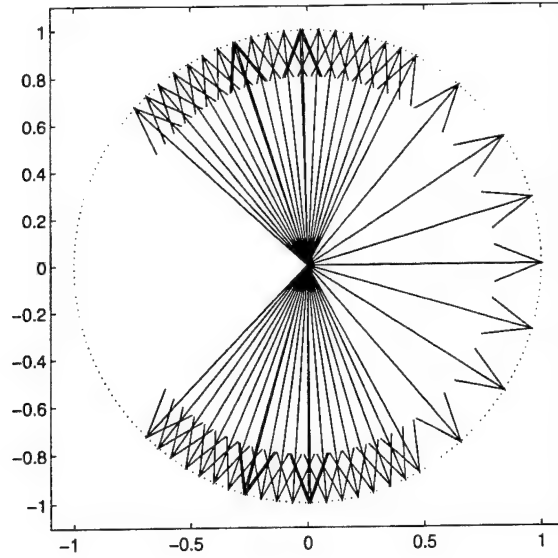


**Figure 12:** Dumbbell source vector diagram for  $\phi' = 27.2^\circ$ .

not too high, then

$$2\pi < \Delta_\theta \leq 3\pi \quad (34)$$

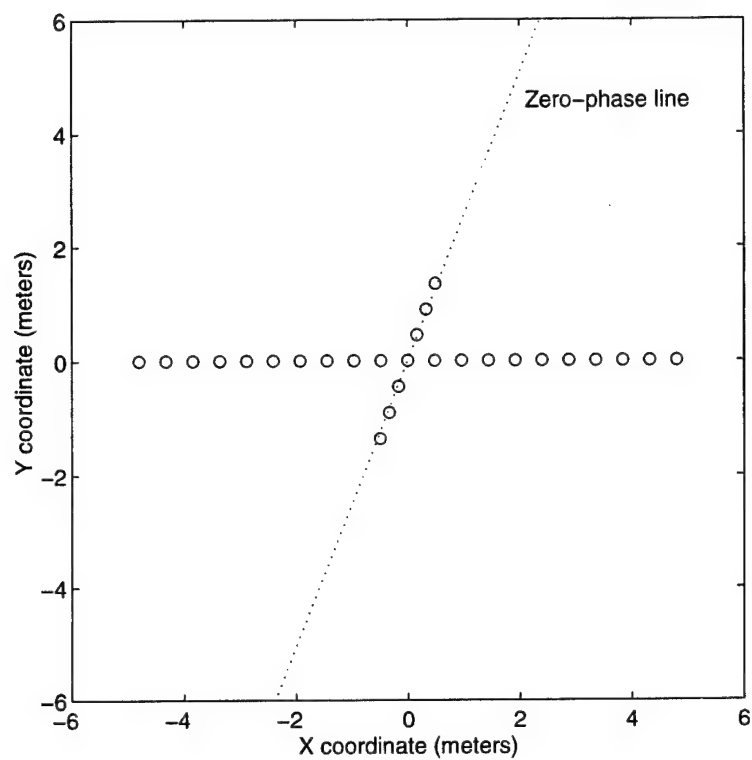
Increasing the number of phase terms concentrated around 0 (i.e. adding more reradiators to the bent arms of the cross) causes the null to fill in (which it has already begun to do – see Figure 13b) until it disappears. At that point, the upper limit in the above relationship will no longer be valid. This is seen as a very special condition since it requires that a large number of reradiators be aligned with the zero-phase line corresponding to a main (or reflection) beam null. For a randomly oriented cross, this would not be true most of the time.

Given that the above shapes represent various extremes (i.e. completely uniform concentration of reradiators, concentration near the ends, and concentration near the middle), the predictions of phase spreading for other shapes will fall somewhere in between the predictions made above. It can therefore be stated that, in general, the phase spreading will be limited according to

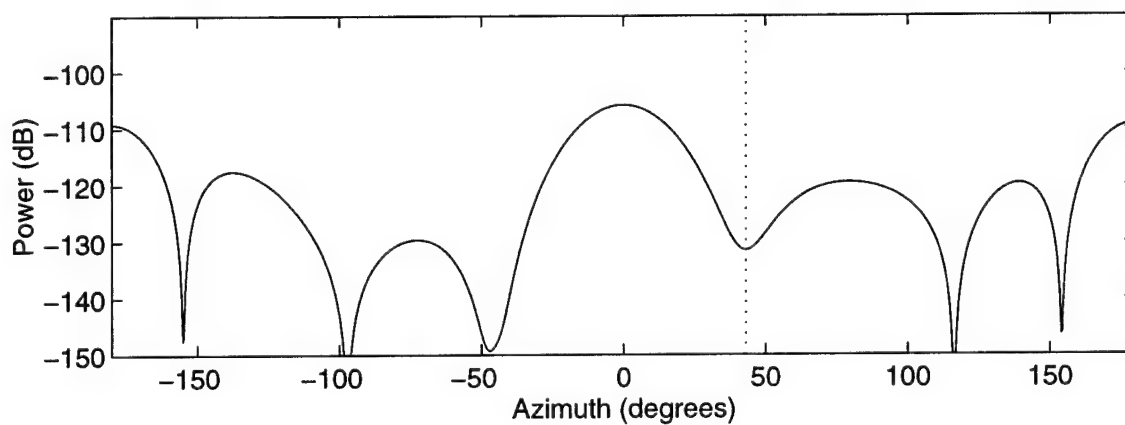
$$\pi \leq \Delta_\theta \leq 3\pi \quad (35)$$

The exception having been discussed previously in the analysis of the bent cross.

Once the phase spread  $\Delta_\theta$  has been determined (or estimated) the corresponding main beam null can be calculated by first identifying  $(x_m, y_m)$  and  $(x_n, y_n)$ , the positions corresponding to the summation terms with minimum and maximum phases respectively.



(a)



(b)

**Figure 13:** Bent cross multipath source showing (a) geometry and zero-phase line for  $\phi' = 43.2^\circ$ , and (b) multipath power as a function of  $\phi$ .

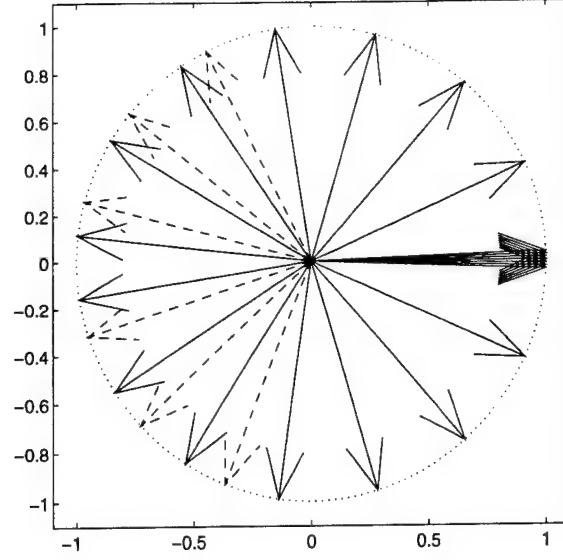


**Figure 14:** Bent cross source vector diagram for  $\phi' = 43.2^\circ$ .

The phase spread is then defined in terms of these positions by computing the individual phases using (27) and then taking the difference to get

$$\Delta_\theta = \frac{2\pi}{\lambda}((x_n - x_m) \sin \phi' - (y_n - y_m)(1 - \cos \phi')) \quad (36)$$

Converting the quantities  $x_n - x_m$  and  $y_n - y_m$  to polar coordinates then

$$\begin{aligned} D \cos \alpha &= x_n - x_m \\ D \sin \alpha &= y_n - y_m \end{aligned} \quad (37)$$

where

$$\begin{aligned} D &= \sqrt{(x_n - x_m)^2 + (y_n - y_m)^2} \\ \alpha &= \arctan \left( \frac{y_n - y_m}{x_n - x_m} \right) \end{aligned} \quad (38)$$

The parameter  $D$  can be interpreted as the physical aperture of the array in azimuth measured perpendicular to the zero-phase line, and  $\alpha$  is the angle that the line joining  $(x_m, y_m)$  to  $(x_n, y_n)$  makes with the X-axis. Substituting  $D$  and  $\alpha$  into (36) then

$$\Delta_\theta = \frac{2\pi D}{\lambda}(\sin(\phi_{null} + \alpha) - \sin \alpha) \quad (39)$$

and finally rearranging in terms of  $\phi_{null}$  results in

$$\phi_{null} = \arcsin \left( \frac{\Delta_\theta \lambda}{2\pi D} + \sin \alpha \right) - \alpha \quad (40)$$

Using the minimum and maximum values for  $\Delta_\theta$  to calculate the minimum and maximum values of  $\phi_{null}$  for the main beam null, and noting that the null beamwidth will be twice these values of  $\phi$ , then

$$2 \left| \arcsin \left( \frac{\lambda}{2D} + \sin \alpha \right) - \alpha \right| \leq \phi_{bw} \leq 2 \left| \arcsin \left( \frac{3\lambda}{2D} + \sin \alpha \right) - \alpha \right| \quad (41)$$

In the realworld, large multipath sources ( $D \gg \lambda$ ) will usually have both width and depth (relative to the transmitted signal direction) so that  $\alpha \approx 0$ . Under these conditions the expression above simplifies to

$$\frac{\lambda}{D} \leq \phi_{bw} \leq \frac{3\lambda}{D} \quad (42)$$

The most notable thing in either expression is that as  $D$  increases the beamwidth decreases. Therefore the smaller the multipath source, the greater the scattering of the reradiated signal.

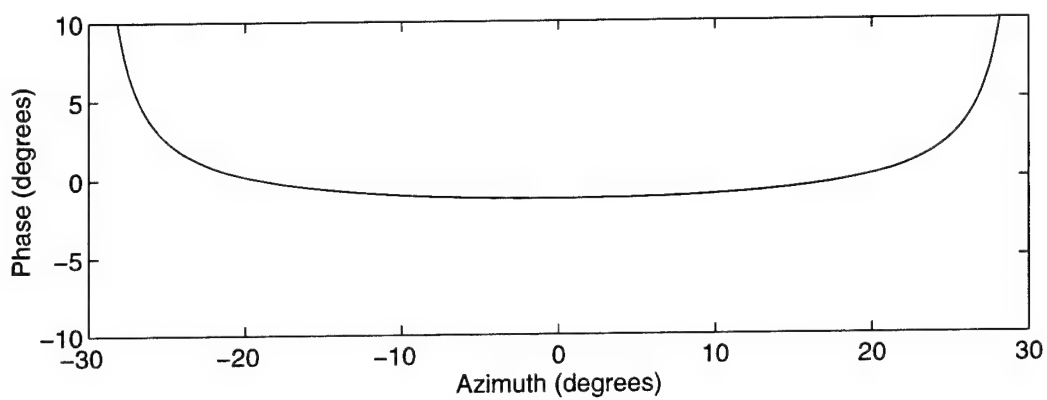
As mentioned previously, the above analysis also applies to the elevation beamwidth  $\psi_{bw}$  except that the X and Z axes are interchanged. The main effects on the results is that the X coordinates of the reradiators constituting a multipath source will have no effect on the elevation beamwidth, and  $D$  will be the elevation aperture.

### 2.3.3 Beam Phase

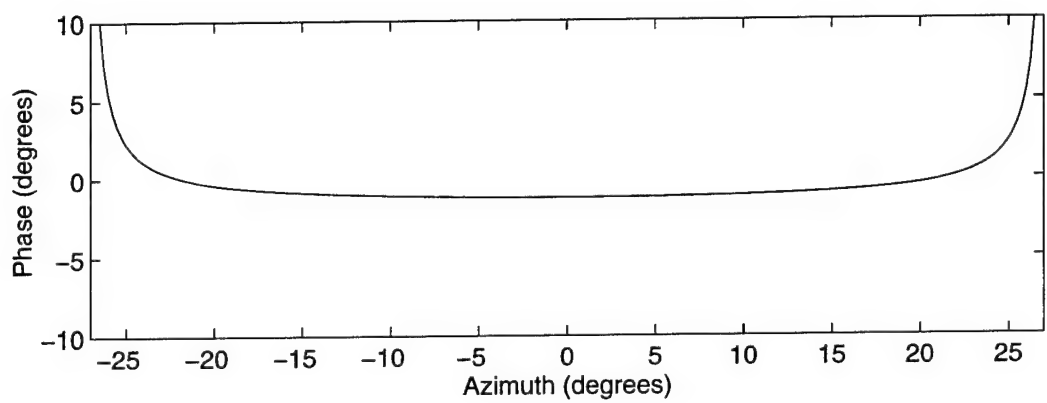
Figure 15 shows the phase (measured relative to  $s_{ref}/\beta$ ) of the three representative multipath sources described in the previous section. Only receiver azimuth angles corresponding to the main beam are shown. In all three cases the phase is well behaved, being zero at  $\phi = 0^\circ$  and gradually changing as a function  $\phi$  until near the beam edges where it changes more rapidly.

### 2.3.4 Reflections

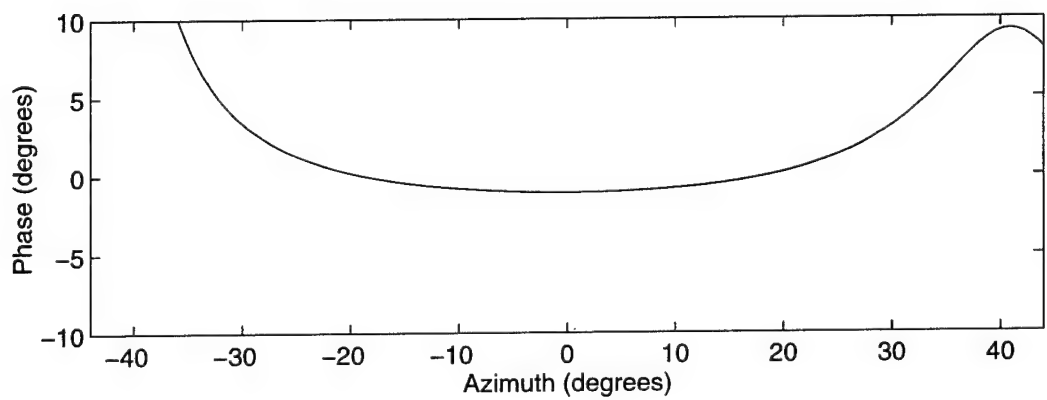
Up to this point, the analysis of multipath source shape and size has been restricted



(a)



(b)



(c)

**Figure 15:** Multipath source main beam phase for the (a) line source, (b) dumbbell, and (c) bent cross.

to the characteristics of the main beam. In general, this analysis is also applicable to the reflection beam except that the shape of a multipath source and its orientation has a pronounced effect on the direction and power of the reflection beam. In the linear source case, for example, the electrical symmetry of the array along the length of the line source dictates that the main beam will be duplicated symmetrically about a line running the length of the line source. This second beam is defined here as a reflection beam. Examples are shown in Figure 16 for three orientations of the line source. For the  $0^\circ$  and  $45^\circ$  orientations, the center of the reflection lobes correspond to  $180^\circ$  and  $90^\circ$  in azimuth, respectively. For the  $90^\circ$  orientation the line source is aligned with the signal direction so that the main and duplicate beams become one and the same.

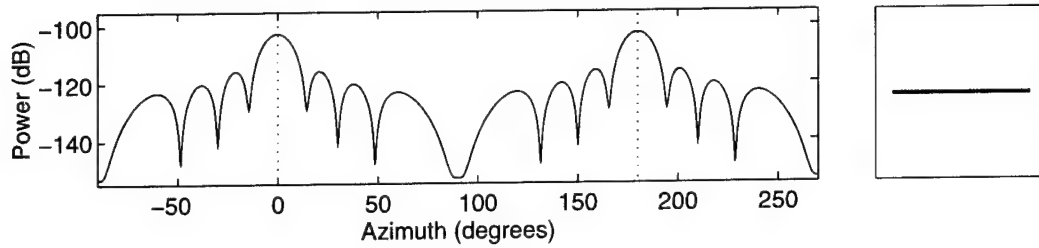
Figure 17 shows a comparison between the reflection beam generated by a line source, a rectangular shaped source, and a square shaped source. As has already been implied, in the case of the line source, the amplitude of the reflection beam is the same as the main beam. In the case of the thin rectangular shaped source (three rows of reradiators), the reflection beam is still generated although lower in amplitude than the main beam. Finally, in the case of the thicker rectangular shaped source (ten rows of reradiators), there is no obvious reflection beam.

Two important points are illustrated by these examples. The first is that reflection beams tend to be generated if the multipath source is thin with respect to the direction of the transmitted signal. In the case of the thick rectangle, a signal is reflected backwards from each row of reradiators, but since the signals from different rows travel different distances, these signals tend to cancel each other. For example, a signal reflected off the first row and the  $k^{th}$  row will have a phase difference of

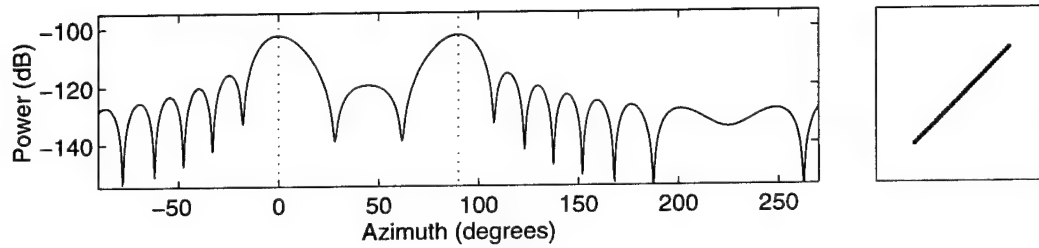
$$\theta_{1k} = \frac{4(k-1)\pi d}{\lambda} \quad (43)$$

If the distance between the two rows is  $(k-1)d = \lambda/4$  the two signals will cancel. Hence for a strong reflection beam "thin" means less than  $\lambda/4$ .

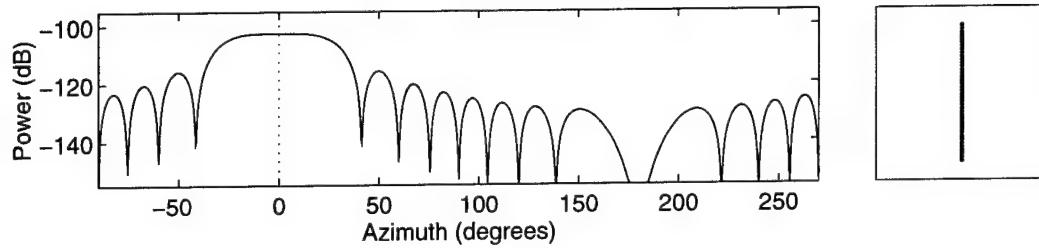
The second point is that since the mechanism that generates the reflection beam is similar to the main beam, the preceding analysis can be applied. The only difference is that the direction of the reflection beam will be different from  $\phi = 0$  (by definition) and the apparent value of the reradiation constant for the reflection beam ( $\beta_r$ ) may be lower (i.e.  $\beta_r \leq \beta$ ).



(a)



(b)



(c)

**Figure 16:** Reflection beam generated by a line source with orientations relative to the transmitter signal of (a)  $0^\circ$  (broadside), (b)  $45^\circ$ , and (c)  $90^\circ$  (in line or endfire). Dotted lines show positions of both the main lobe (at  $0^\circ$  azimuth) and reflection lobe (if present). Line source orientations are also plotted in small boxes on righthand side.

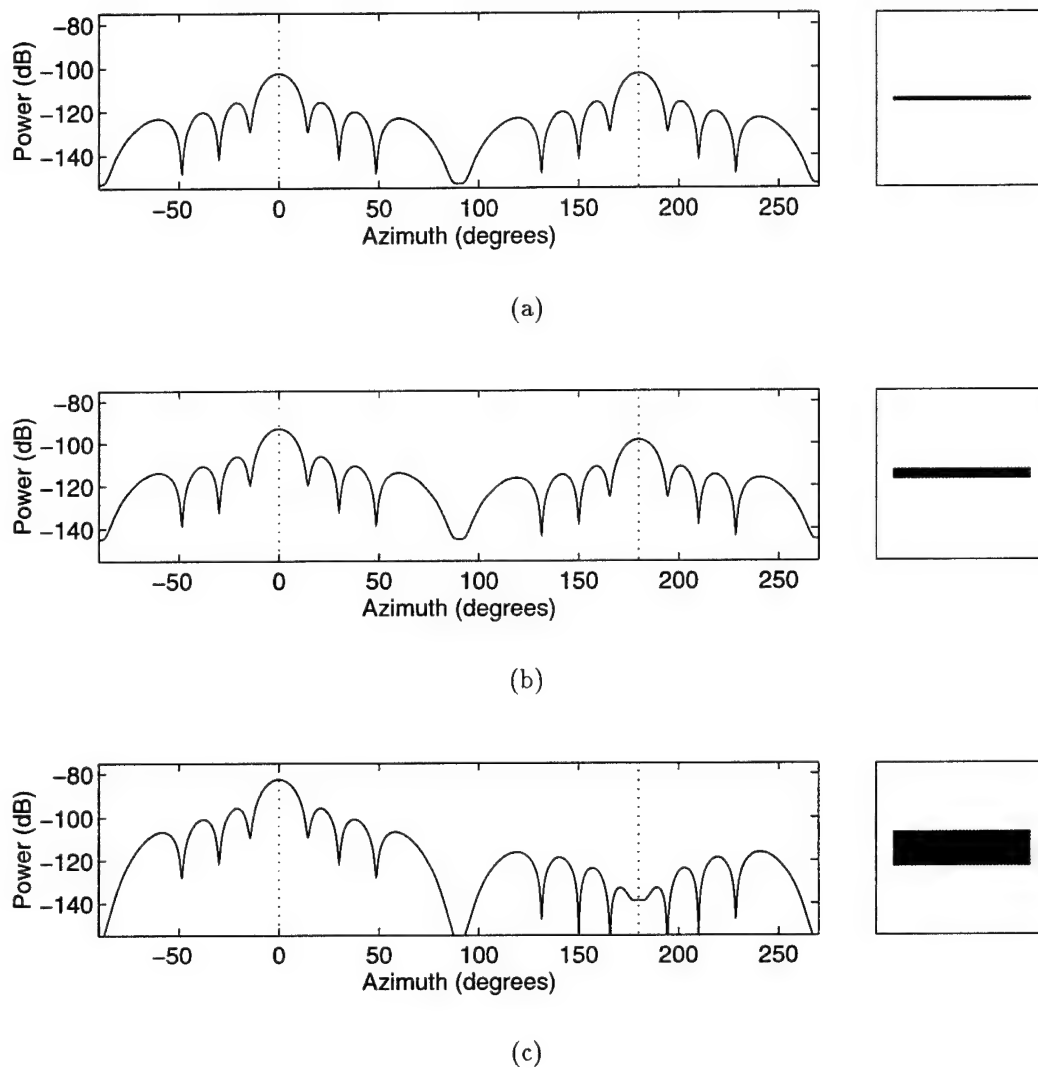


**Figure 17:** Comparison of the reflection beam generated by (a) a line source, (b) a thin rectangular shaped source, and (c) a thicker rectangular shaped source. Dotted lines show the position of the main beam ( $0^\circ$ ) and expected position of reflection beam ( $180^\circ$ ). Source shapes and orientations are shown in small boxes on righthand side.



### 2.3.5 The Beam Model

Based on the previous analysis, a multipath source (consisting of a collection of identical reradiators) could be modelled using

$$s_{mult} = s_{tx} \beta \rho_{\alpha m}(r_a) \rho_{\alpha r}(r_b) f(\phi, \psi) \quad (44)$$

where  $f(\phi, \psi)$  is the beam pattern of the multipath source and is given by

$$f(\phi, \psi) = \frac{1}{\rho_{\alpha m}(r_a) \rho_{\alpha r}(r_b)} \sum_{k=1}^N \rho_{\alpha m}(r_{ak}) \rho_{\alpha r}(r_{bk}) \quad (45)$$

In the case where  $r_a$  and  $r_b$  are much larger than the largest physical dimension of the multipath source, and the coordinate system is chosen so that the transmitter lies on the negative Y-axis (as in Figure 5), the beam pattern can be approximated by

$$f(\phi, \psi) = \sum_{k=1}^N e^{j \frac{2\pi}{\lambda} (x_k \sin \phi \cos \psi - y_k (1 - \cos \phi \cos \psi) + z_k \sin \psi)} \quad (46)$$

### 3.0 COUPLING EFFECTS

Previously, the effects of coupling were ignored. However, since the elemental reradiators have an isotropic reradiation pattern, the incident signal for each reradiator will not only include the transmitter signal but also include contributions from all other reradiator. Incorporating these additional contributions into the multipath model is the subject of the following sections. Additionally, since the effects of coupling are not always immediately obvious from an inspection of the mathematics, the changes to the multipath source characteristics discussed previously (e.g. power, beamwidth, etc.) are also examined using examples to support this discussion.

Following the discussion on coupling for a single multipath source, the coupling for more than one multipath source is discussed. Although the modelling can be handled simply by extending the method used for single multipath sources, this can lead to a high computational load. Hence the discussion focuses on methods which simplify the processing requirements when certain conditions are met.

#### 3.1 Coupling within a Multipath Source

In the case where  $N$  discrete reradiators are in the same vicinity, the received signal for any one reradiator will be the contribution from the transmitting antenna plus contributions from each of the other reradiating sources. That is, applying (14) to each of the sources and adding the results yields the following system of equations

$$\begin{aligned} s_{m1} &= \beta_1(s_{tx}\rho_{\alpha m}(r_{a1}) + s_{m2}\rho_{\alpha m}(r_{12}) + s_{m3}\rho_{\alpha m}(r_{13}) + \dots + s_{mN}\rho_{\alpha m}(r_{1N})) \\ s_{m2} &= \beta_2(s_{tx}\rho_{\alpha m}(r_{a2}) + s_{m1}\rho_{\alpha m}(r_{21}) + s_{m3}\rho_{\alpha m}(r_{23}) + \dots + s_{mN}\rho_{\alpha m}(r_{2N})) \\ &\vdots \\ s_{mN} &= \beta_N(s_{tx}\rho_{\alpha m}(r_{aN}) + s_{m1}\rho_{\alpha m}(r_{1N}) + s_{m2}\rho_{\alpha m}(r_{2N}) + \dots + s_{mN}\rho_{\alpha m}(r_{N-1,N})) \end{aligned} \quad (47)$$

where  $s_{mk}$  represents the signal reradiated by the  $k^{th}$  reradiator,  $\beta_k$  is the reradiation coefficient for the  $k^{th}$  reradiator,  $r_{ak}$  is the distance from the transmitter to the  $k^{th}$  reradiator, and  $r_{kl}$  is the distance between the  $k^{th}$  and  $l^{th}$  reradiator. Rearranging these equations so that all terms involving  $s_{tx}$  are on the left hand side and all terms involving  $s_{mk}$  for  $k = 0, 1, \dots, N$  are on the right hand side gives (using matrix notation)

$$s_{tx}\mathbf{p}_\alpha = \mathbf{C}_\alpha \mathbf{s}_m \quad (48)$$

where  $\mathbf{p}_\alpha$  is the  $N \times 1$  vector representing the attenuations from the transmitter to each of the reradiators ( $s_{tx}\mathbf{p}_\alpha$  represents the incident signal) with elements  $p_1, p_2, \dots, p_N$  defined by

$$p_k = -\rho_{\alpha m}(r_{ak}) \quad (49)$$

$\mathbf{s}_m$  is the  $N \times 1$  vector representing the reradiated signal with elements  $s_{m1}, s_{m2}, \dots, s_{mN}$ , and  $\mathbf{C}_\alpha$  is the  $N \times N$  coupling matrix with elements

$$c_{kl} = \rho_{\alpha m}(r_{kl}) \quad \text{for } k \neq l, \quad k, l = 1, 2, 3, \dots, N \quad (50)$$

and

$$c_{kk} = \frac{-1}{\beta_k} \quad (51)$$

The solution for the reradiated signals can be determined by solving the system of equations represented by (47), or by rearranging (48) to get

$$\mathbf{s}_m = s_{tx}\mathbf{C}_\alpha^{-1}\mathbf{p}_\alpha \quad (52)$$

Finally, the received multipath signal will be the sum of all the reradiated signals with the appropriate corrections made for the losses incurred over the reradiator to the receiver paths. To represent this mathematically, the reradiator-receiver attenuations are represented by the  $N \times 1$  vector  $\mathbf{q}_\alpha$  whose elements  $q_1, q_2, \dots, q_N$  are defined by

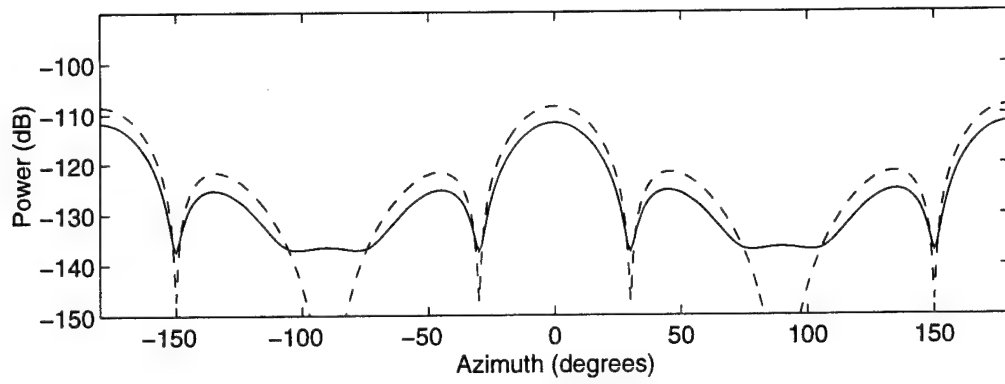
$$q_k = \rho_{\alpha r}(r_{bk}) \quad (53)$$

where  $r_{bk}$  represents the distance from the  $k^{th}$  reradiator to the receiver. The multipath signal at the receiver is then given by

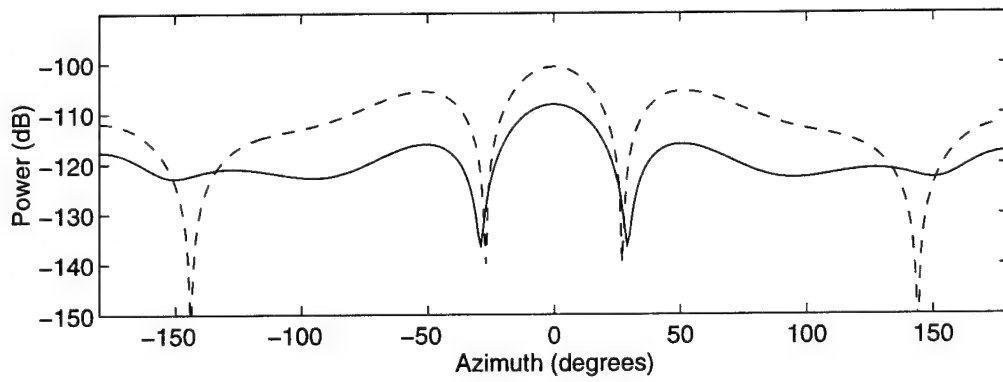
$$s_{mult} = s_{tx}\mathbf{q}_\alpha^T\mathbf{C}_\alpha^{-1}\mathbf{p}_\alpha \quad (54)$$

This is called the freespace multipath expression in this report. For a single reradiator this expression reduces to (15).

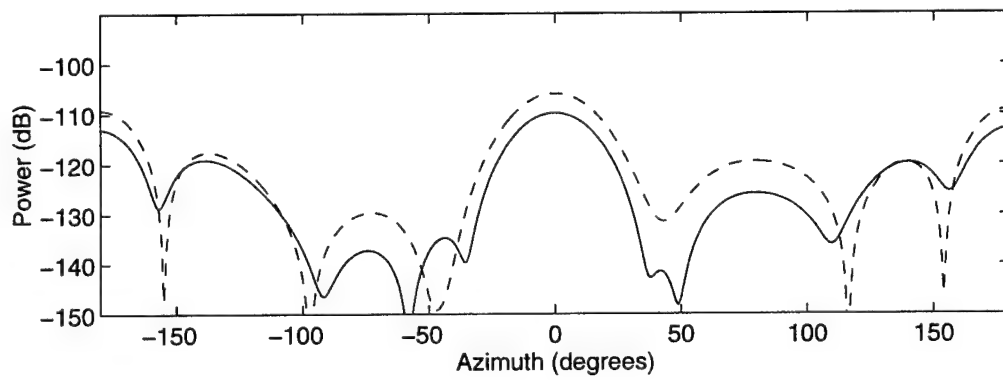
Using this last expression to calculate the signals generated by various multipath sources, Figures 18 and 19 show some results. In Figure 18, the amplitudes of the multipath signals for the three shapes discussed in the previous section are plotted including the uncoupled (dashed lines) and coupled cases (solid lines). Figure 19 shows the corresponding phases. In both Figures, coupling clearly has an effect on the multipath signals.



(a)

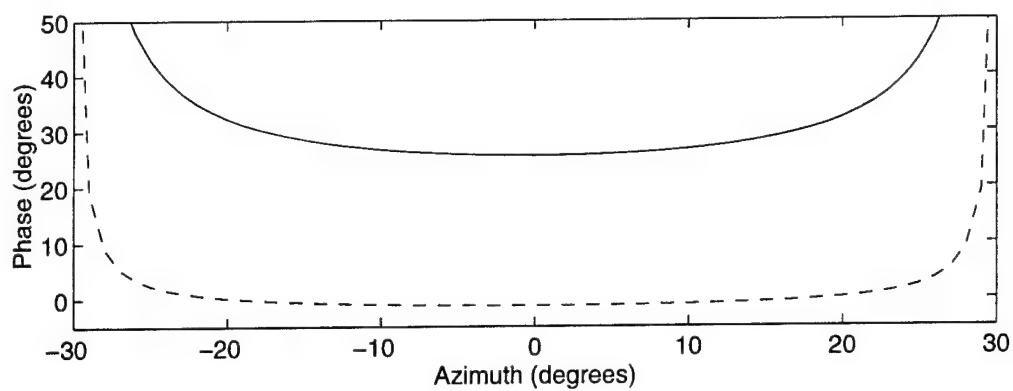


(b)

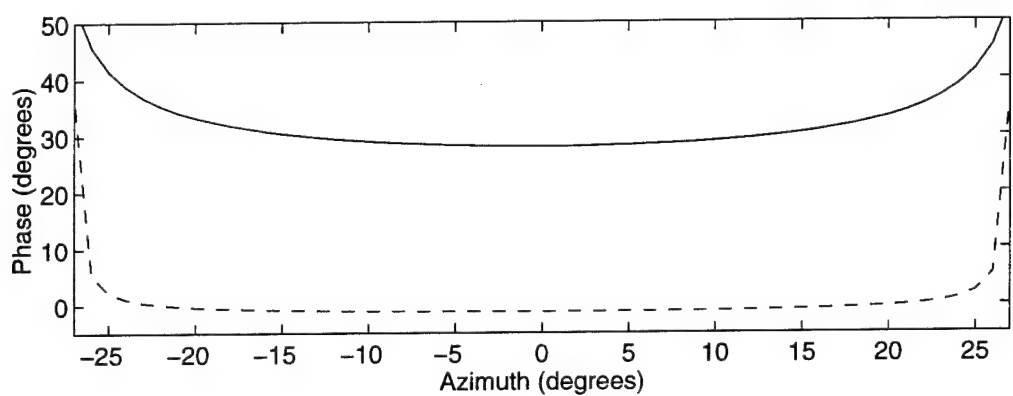


(c)

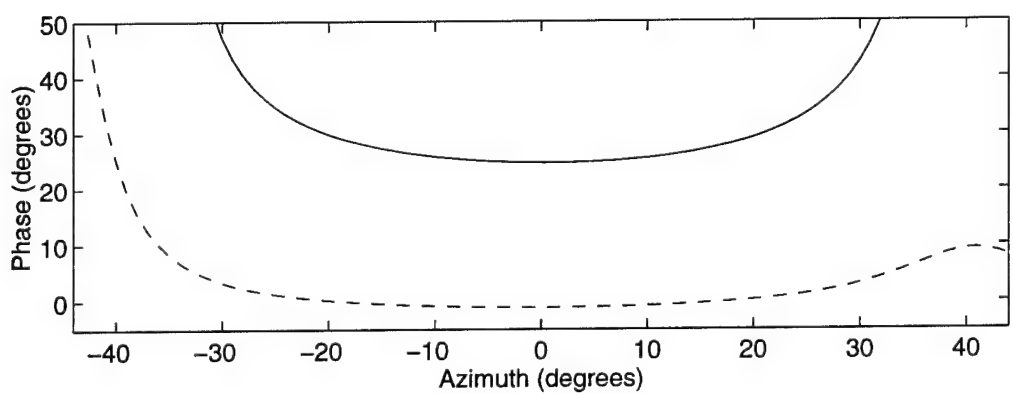
**Figure 18:** Multipath source power (with coupling effects included) as a function of azimuth for the (a) line source, (b) dumbbell, and (c) bent cross.



(a)



(b)



(c)

**Figure 19:** Multipath source main beam phase (with coupling effects included) for the (a) line source, (b) dumbbell, and (c) bent cross.

### 3.2 Characteristics of a Coupled Multipath Source

In many ways the derived characteristics of a multipath source are very similar when coupling effects are taken into account as when they are ignored. As a result, a multipath source can be characterized in exactly the same manner. This is the subject of the following sections. In addition, the important differences between the coupled and uncoupled cases are also highlighted.

#### 3.2.1 Effect on Power

In terms of power, the maximum power of the signal reradiated from the coupled systems in the main and side lobes is less than for the uncoupled system. Additionally, the nulls also tend to become filled in as well. The reduction in power can be explained by considering a single reradiator, the  $k^{th}$  reradiator, in a collection of reradiators. The incident signal will be the sum of the transmitter signal plus contributions from the surrounding reradiators. Since the contributions from the surrounding reradiators will generally be out-of-phase with the direct signal, the incident signal is reduced compared to the no coupling case. As a result, the reradiated signal from the  $k^{th}$  reradiator will also be reduced. Applying this logic to all the reradiators, then a decrease in the combined reradiated signal amplitude and power would occur when coupling is taken into account.

Borrowing ideas from optics, the reduction in power due to coupling could be interpreted as a reduction in the illuminated area of the multipath source compared to the sum of the collection areas of the individual reradiators. For example, as the spacing is increased between reradiators, the collection areas of the individual reradiators will overlap less and less so that the collection area of the multipath source approaches  $N\mu_m^2$ . Conversely, if the spacing is reduced to zero, the reradiators completely overlap and the collection area of the multipath source is reduced to that of a single reradiator.

One way to test this optics analogy is to predict the effect of spacing and compare to actual results. For example, approximating the reradiator collection area as square with dimensions  $\mu_m \times \mu_m$  the total collection area of the line source would be

$$\mu_M^2 = \begin{cases} \mu_m^2 + (N-1)\mu_m d & \text{if } d \leq \mu_m \\ N\mu_m^2 & \text{otherwise} \end{cases} \quad (55)$$

The maximum reradiated power  $P'_m$  for the coupled system would then be given by

$$P'_m = P_m \frac{\mu_M^2}{n\mu_m^2} \quad (56)$$

where  $P_m$  is the maximum power for an uncoupled system computed using (25).

Figure 20 shows a comparison between the predicted results and simulation results. The dashed line represents the predicted value for  $\mu_M^2/N\mu_m^2$  using (55) to determine  $\mu_M^2$ . The solid line represents the simulation value of  $P'_m/P_m$  (which is equivalent to  $\mu_M^2/N\mu_m^2$ ) as a function of  $d$ . Examining the results, the optics approach reasonably predicts the drop in amplitude for  $d < \mu_m$ , although the predicted values are approximately 3 dB too high. This error is probably attributable to the fact that the collection area of a single reradiator was modelled as being square, whereas, in fact, it is circular with no well defined boundaries. The result is that there is still some overlapping of the collection areas of the reradiators even when  $d = \mu_m$ . Adjusting (54) accordingly, a better approximation for the line source is given by

$$\mu_M^2 = \begin{cases} \mu_m^2 + 0.5(N-1)\pi\mu_m d & \text{if } d \leq 0.5\pi\mu_m \\ N\mu_m^2 & \text{otherwise} \end{cases} \quad (57)$$

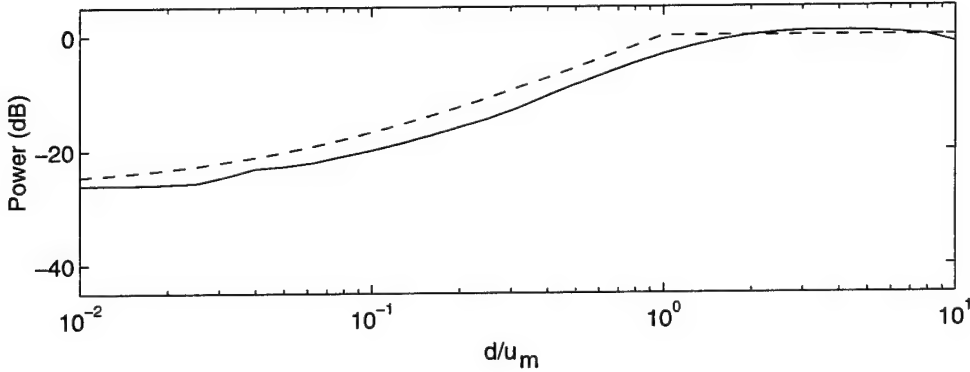


**Figure 20:** Maximum power for the line source as the reradiator spacing  $d$  is varied while  $\mu_m^2$  is kept constant. Solid line shows the simulated result and the dashed line shows the predicted result when the reradiator collection area is assumed to be square.

Based on the preceding analysis alone, the predicted decrease in maximum amplitude would be -3 dB for all three shapes. This is not true, particularly in the case of the

dumbbell. Returning to the example of the  $k^{th}$  reradiator, two other factors which reduces the incident signal are the number of other surrounding reradiators and the location of these other reradiators. The decrease in incident signal as the number of surrounding reradiators increases needs no explanation. Location plays a role in terms of distance from the  $k^{th}$  reradiator as well as orientation with respect to the line joining the transmitter and  $k^{th}$  reradiator. For example, a second reradiator lying anywhere along this line but between the transmitter and the  $k^{th}$  reradiator will produce a signal which is out-of-phase with the direct signal. On the opposite side of the reradiator, away from the transmitter (but still on the line), the signal phases from the individual reradiators will quickly change in phase as a function of distance from the  $k^{th}$  reradiator. This can be summarized mathematically as,

$$\theta_{kl} = \begin{cases} 0 & \text{same side as transmitter} \\ \frac{4\pi r_{kl}}{\lambda} & \text{opposite side} \end{cases} \quad (58)$$

where  $r_{kl}$  is the distance between the  $k^{th}$  and  $m^{th}$  reradiators, and  $\theta_{kl}$  is the change in phase due to this distance. Taking path attenuations into account, it follows that the incident signal on the  $k^{th}$  reradiator will be affected by all the reradiators between it and the transmitter but only the reradiators out to a distance of  $\lambda/4$  in the opposite direction (beyond this distance the alternating phase greatly diminishes the contribution of reradiated signals). Extending this analysis to all possible locations for the  $m^{th}$  reradiator results in regions as illustrated in Figure 21 where the white regions corresponds to  $\theta_{kl} \leq \pi$  and the dark regions to  $\theta_{kl} \geq \pi$  (where it is assumed  $\theta_{kl}$  is normalized to the range  $0 \leq \theta_{kl} < 2\pi$ ). The central white region, which encompasses the transmitter and  $k^{th}$  reradiator, is called the first Fresnel zone [8]. The surrounding black is the second Fresnel zone, the next white region is the third Fresnel zone, and so on. Reradiators located in the first Fresnel zone will have the most effect on the incident signal of the  $k^{th}$  reradiator given the size of this zone and its proximity to the transmitter and  $k^{th}$  reradiator. Within this region, path losses will favour reradiators that are closer to either the transmitter or the  $k^{th}$  reradiator.

This “shadowing” effect is important since the net result is that the row of reradiators closest to the transmitter will be the least affected (highest incident signal) and will therefore reradiate the highest signal. Each successive row will reradiate less and less as more and more reradiators move into the first Fresnel zone. Comparing the three different shapes used to produce Figures 18 and 19, the Fresnel zone effect will play the strongest role for the dumbbell and the weakest for the line source. This is reflected in



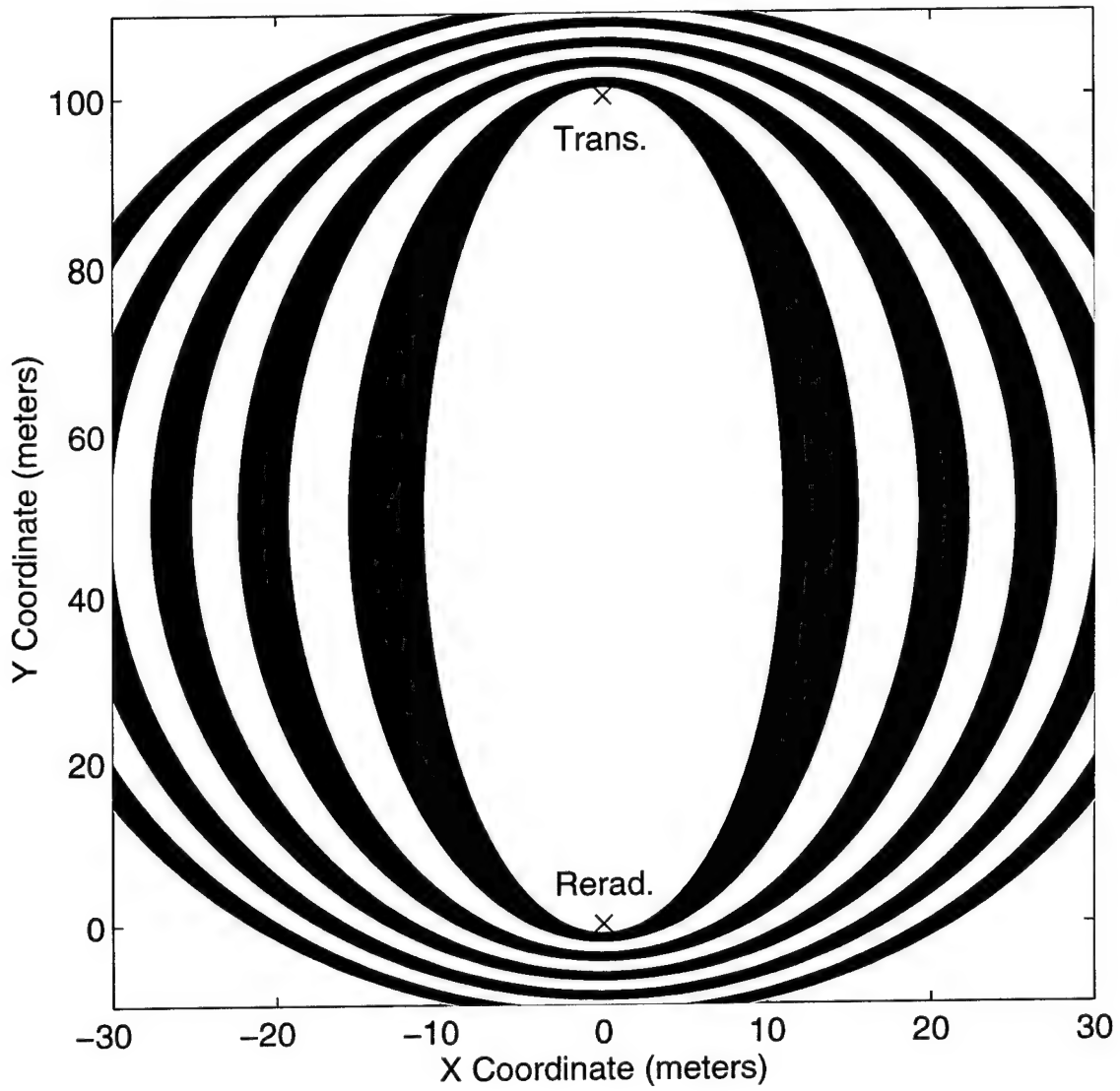


**Figure 21:** Depiction of the first ten Fresnel zones for a transmitter and the  $k^{th}$  reradiator. The innermost region, which contains both the transmitter and the  $k^{th}$  reradiator, is the first Fresnel zone.

the amplitude differences which were -7.5 dB, -3.9 dB, and -3.2 dB for the dumbbell, the bent cross, and the line shapes, respectively.

### 3.2.2 Effect on Beamwidth

Despite the changes in power and phase, and some filling in of the nulls, the shape of the main beam remains relatively unaffected. As a result, the characterization of beamwidth discussed in Section 2.3.2 remains valid.

### 3.2.3 Effect on Phase

The main affect on phase observed in Figure 19 is a constant offset of 20°-30°, and a more gentle roll-off near the label nulls. The offset is due to the effect of the reradiators contributing to the incident signal. For example, the incident signal for the  $k^{th}$  reradiator is the transmitter signal plus the contribution of the surrounding reradiators. Since the reradiator signals will tend to involve extra path lengths compared to the transmitter signal, the resultant incident signal will tend to be phase shifted slightly. For example, consider one of the central reradiators in the line source, the  $k^{th}$  reradiator. Given that the greatest coupling is between its nearest neighbours (the  $(k-1)^{th}$  and the  $(k+1)^{th}$  reradiators), then for the sake of this discussion, all other reradiators can be ignored. Based on this simplification and using (47) the reradiated signal from the  $k^{th}$  reradiator is given by,

$$s_{mk} = \beta_k(s_{tx}\rho_{\alpha m}(r_{ak}) + s_{mk-1}\rho_{\alpha m}(r_{kk-1}) + s_{mk+1}\rho_{\alpha m}(r_{kk+1})) \quad (59)$$

Given the translational symmetry of the line source, except near the ends, then  $s_{mk-1} \approx s_{mk} \approx s_{mk+1}$ . Using this approximation and the fact that  $r_{kk-1} = r_{kk+1} = \mu_m$ , the above expression can be simplified to

$$\begin{aligned} s_{mk} &= \beta_k(s_{tx}\rho_{\alpha m}(r_{ak}) + 2s_{mk}\rho_{\alpha m}(\mu_m)) \\ &= \beta_k\left(s_{tx}\rho_{\alpha m}(r_{ak}) + \frac{s_{mk}}{\sqrt{\pi}}e^{-j\frac{2\pi}{\lambda}\mu_m}\right) \end{aligned} \quad (60)$$

Rearranging to solve for  $s_{mk}$  yields

$$s_{mk} = \frac{\beta_k s_{tx} \rho_{\alpha m}(r_{ak})}{1 - \frac{\beta_k}{\sqrt{\pi}} e^{-j \frac{2\pi}{\lambda} \mu_m}} \quad (61)$$

Letting  $s'_{mk}$  represent the value when coupling is ignored where

$$s'_{mk} = \beta_k s_{tx} \rho_{\alpha m}(r_{ak}) \quad (62)$$

then

$$\frac{s_{mk}}{s'_{mk}} = \frac{1}{1 - \frac{\beta_k}{\sqrt{\pi}} e^{-j \frac{2\pi}{\lambda} \mu_m}} \quad (63)$$

For a value of  $\beta_k = -1$  and  $\mu_m = \lambda/10$  the above formula predicts a value of  $s_{mk}/s'_{mk} = 0.653 + j0.149$ , or a phase difference between the coupled and uncoupled cases of  $12.8^\circ$ . Although somewhat smaller than the value of  $26.9^\circ$  shown for the line source in Figure 18a (attributable to the fact that coupling effects were restricted to the two nearest neighbours) it does demonstrate the mechanism by which the phase offset arises.

### 3.2.4 Enhancement of Reflections

In Section 2.3.4, it was shown that the thickness of the multipath source (i.e. the extent of the multipath source measured in the same direction as the transmitter signal) had a strong effect on the power of the reflection beam, with thin sources having a stronger reflection than thick sources. When coupling is taken into account, the reradiators on the surface or edge closest to the transmitter receive the greatest illumination while reradiators in successive rows behind receive less and less illumination due to shadowing effects. The result is the reflection beam generated by the first row is not completely cancelled by the reflections from successive rows, because successive reflections become weaker and weaker (especially compared to the uncoupled case).

Figure 22 illustrates this phenomena showing the same results as in Figure 17 except including coupling effects. The dashed lines represent the original results from Figure 17 which have been included for comparison. The effect of coupling on the reflection beam is most obvious in Figure 22c where the reflection beam has been reduced but not eliminated as happened in the uncoupled case.

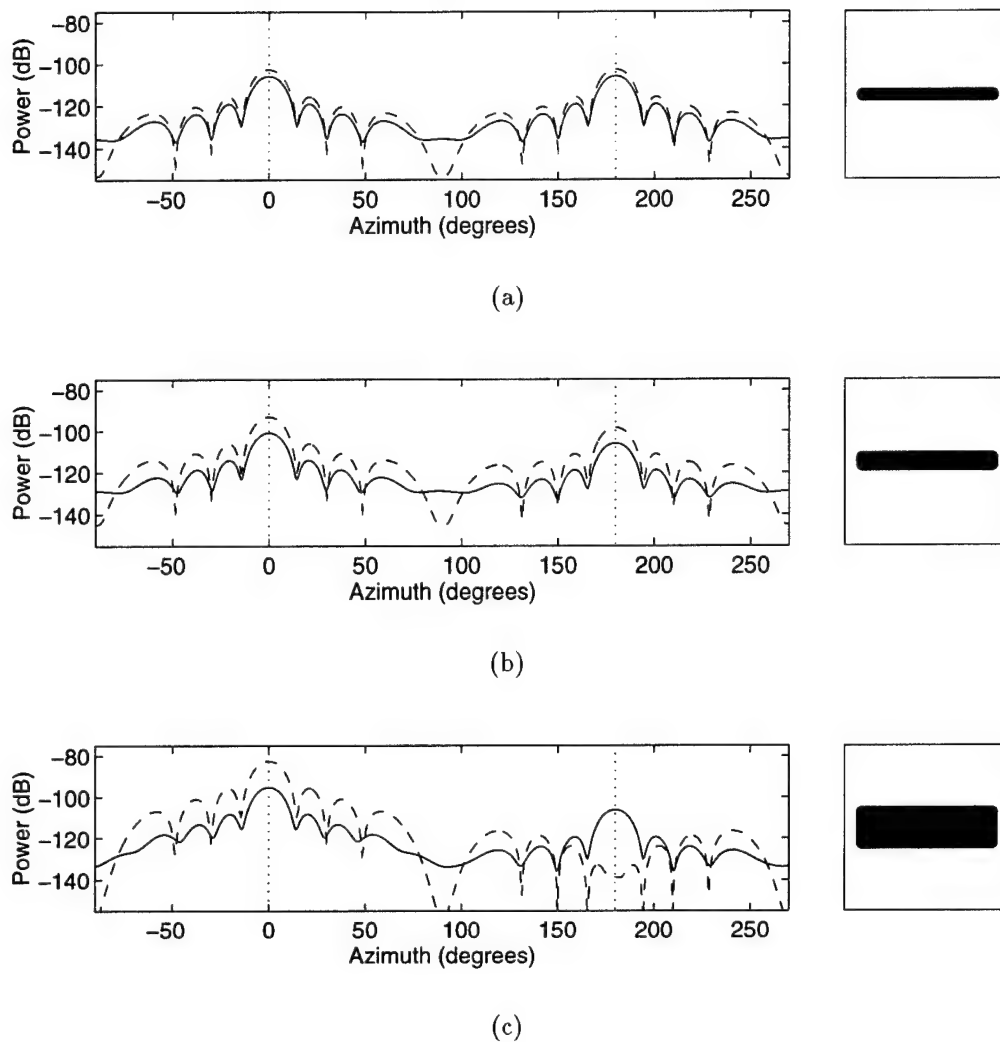


**Figure 22:** Comparison of the reflection beam generated by (a) a line source, (b) a thin rectangular shaped source, and (c) a thicker rectangular shaped source. Solid line shows results for a coupled system and the varying dashed line shows the results when coupling is ignored. The vertical dotted lines show the position of the main beam ( $0^\circ$ ) and expected position of reflection beam ( $180^\circ$ ). Source shapes and orientations are shown in small boxes on righthand side.

### 3.2.5 The Modified Beam Model

As in the case where coupling was ignored, the multipath source can be modelled using (44), which is repeated here as

$$s_{mult} = s_{tx} \beta \rho_{\alpha m}(r_a) \rho_{\alpha r}(r_b) f(\phi, \psi) \quad (64)$$

The main difference from the coupled case is the determination of  $f(\phi, \psi)$ . Taking coupling effects into account, (45) becomes

$$f_k(\phi, \psi) = \mathbf{e}(\phi_b, \psi_b)^H \mathbf{C}_\alpha^{-1} \mathbf{e}(\phi_a, \psi_a) \quad (65)$$

where  $\phi$  and  $\psi$  are the azimuth and elevation angles defined in Section 2.3.5, the superscript  $H$  denotes conjugate transpose,  $\mathbf{C}$  is the coupling matrix, and  $\mathbf{e}(\cdot)$  is an  $N \times 1$  normalized signal vector (a “steering” vector) whose elements are defined as

$$e_i(\phi_c, \psi_c) = \frac{\rho_{\alpha m}(r_{ci})}{\rho_{\alpha m}(r_c)} \quad i = 1, 2, \dots, N \quad (66)$$

In the above definition, the subscript  $c$  is used to represent the letters  $a$  or  $b$ . If the dimensions of the multipath source are small compared to the path lengths  $r_a$  and  $r_b$ , and the X-Y plane is oriented so the transmitter lies on the negative Y axis ( $\phi_a = 180^\circ$  and  $\psi_a = 0^\circ$ ) with the multipath source at the origin, then  $e_i(\phi, \psi)$  can be simplified to

$$e_i(\phi_c, \psi_c) = e^{j \frac{2\pi}{\lambda} (x_i \sin \phi_c \cos \psi_c + y_i \cos \phi_c \cos \psi_c + z_i \sin \psi_c)} \quad i = 1, 2, \dots, N \quad (67)$$

### 3.3 Processing for More Than One Multipath Source

When dealing with more than one multipath source, coupling effects can be computed by considering the individual coupling effects between all reradiators and using the equations developed in Section 3.1 with  $\beta$  appropriately modified for each multipath source. This leads to a large increase in computations, as two multipath sources with  $N$  reradiators would result in a  $2N \times 2N$  coupling matrix. Adding more and more multipath sources can quickly lead to a very large unwieldy coupling matrix. Under some conditions, approximations can be introduced which allow much simpler processing methods to be used. Two such methods are discussed in the following sections. Some examples are also included to illustrate the strengths and weaknesses of the two methods compared to the

approach that has already been developed (called the *full coupling method* here).

### 3.3.1 Coupling between Multipath Sources

If the distance between multipath sources is much greater than the largest dimensions of the individual multipath sources (i.e. farfield conditions), then an alternate approach is to treat each multipath source as a fundamental unit, rather than as a collection of individual reradiators. Consider, for example, the multipath contribution of the  $k^{th}$  source in a group of  $K$  multipath sources. A part of the contribution from this source will be the signal travelling from the transmitter to the receiver via the  $k^{th}$  multipath source. This is given by

$$s_{tx}\beta'_k\rho_{\alpha m}(r_{ak})f_{akb}\rho_{\alpha r}(r_{bk}) \quad (68)$$

where  $f_{xyz}$  is the beam function for the  $y^{th}$  multipath source ( $y = 1, 2, \dots, K$ ) with the incoming signal direction denoted by  $x$  ( $x = a$  represents the transmitter as the signal source, and  $x = 1, 2, \dots, K$  represents one of the multipath objects as the signal source), and the outgoing signal direction denoted by  $z$  ( $z = b$  represents the receiver as the destination, and  $z = 1, 2, \dots, K$  represents one of the multipath objects as the destination). Other components will be the result of signals radiated from the other multipath sources to the receiver via the  $k^{th}$  multipath source. Summing these components gives

$$\beta'_k \sum_{\substack{m=1 \\ m \neq k}}^K s_{mk} f_{mkb} \rho_{\alpha r}(r_{bk}) \quad (69)$$

where  $s_{mk}$  is the signal incident on the  $k^{th}$  reradiator that was generated by the  $m^{th}$  reradiator, and  $K$  is the total number of multipath sources. Combining the above two expressions gives

$$s_{mult_k} = \beta'_k \rho_{\alpha r}(r_{bk}) \left( s_{tx} \rho_{\alpha m}(r_{ak}) f_{akb} + \sum_{\substack{m=1 \\ m \neq k}}^K s_{mk} f_{mkb} \right) \quad (70)$$

Although similar in form to (47), directional dependencies have been introduced which result in an additional  $K(K - 1)$  unknown parameters represented by  $s_{mk}$ . In dealing with isotropic reradiating elements as was done previously,  $s_{m1} = s_{m2} = s_{m3} = \dots = s_{mK}$

since the  $m^{th}$  reradiator radiates the same signal in all directions. Introducing directional dependencies has complicated the solution somewhat.

The solution for the signal component  $s_{mk}$  can be found by considering all the signals incident on the  $m^{th}$  reradiator and the resultant component reradiated towards the  $k^{th}$  reradiator. To solve requires setting up a system of  $K(K - 1)$  equations similar in form to (70) except that the receive element is the  $k^{th}$  multipath source rather than the receive antenna. This new system of equations is represented by

$$s_{mk} = \beta'_m \rho_{\alpha m}(r_{mk}) \left( s_{tx} \rho_{\alpha m}(r_{am}) f_{amk} + \sum_{\substack{i=1 \\ i \neq k}}^K s_{im} f_{imk} \right) \quad (71)$$

where  $m, k = 1, 2, \dots, K$  and  $m \neq k$ . Rearranging so that all terms involving  $s_{mk}$  or  $s_{im}$  are on right hand side, and all terms involving  $s_{tx}$  are on the left hand side then

$$s_{tx} \rho_{\alpha m}(r_{am}) f_{amk} = \frac{s_{mk}}{\beta'_m \rho_{\alpha m}(r_{mk})} - \sum_{\substack{i=1 \\ i \neq k}}^K s_{im} f_{imk} \quad (72)$$

This expression can also be written in matrix format as

$$s_{tx} \mathbf{p}_M = \mathbf{C}_M \mathbf{s}_M \quad (73)$$

where  $\mathbf{p}_M$  is the  $K(K - 1) \times 1$  loss vector (which accounts for the beam pattern and attenuation ) with elements defined by

$$p_n = \rho_{\alpha m}(r_{am}) f_{amk} \quad (74)$$

$\mathbf{s}_M$  is the  $K(K + 1) \times 1$  signal vector with elements  $s_n = s_{mk}$ , and  $\mathbf{C}_M$  is the  $K \times K$  directional coupling matrix with elements defined by

$$c_{nl} = \begin{cases} -f_{imk} & (m - 1)(K - 1) + 1 \leq l \leq m(K - 1) \\ 1 / (\beta'_m \rho_{\alpha m}(r_{mk})) & l = n \\ 0 & \text{otherwise} \end{cases} \quad (75)$$

The relation between the indices in the above definitions are as follows: the sequence

$$n = 1, 2, \dots, K(K - 1) \quad (76)$$

corresponds to the sequence

$$(m, k) = (1, 2), (1, 3), \dots, (1, K), (2, 1), (2, 3), (2, 4), \dots, (K - 1, K) \quad (77)$$

while the sequence

$$l = (m - 1)(K - 1) + 1, (m - 1)(K - 1) + 1, \dots, m(K - 1) \quad (78)$$

corresponds to

$$i = 1, 2, \dots, m - 1, m + 1, m + 2, \dots, K \quad (79)$$

The matrix solution for  $\mathbf{s}_M$  is given by

$$\mathbf{s}_M = s_{tx} \mathbf{C}_M^{-1} \mathbf{p}_M \quad (80)$$

Once the solution for  $\mathbf{s}_M$  has been computed, the elements of  $\mathbf{s}_M$  can be plugged into (68) to compute the values of  $s_{mult_k}$ . The total multipath signal arriving at the receiver is simply the sum of all values of  $s_{mult_k}$ , or

$$s_{mult} = \sum_{k=1}^K s_{mult_k} \quad (81)$$

In computing the received multipath in this manner, the main computation involves solving (72) or (73) which deal with the  $K(K - 1) \times K(K - 1)$  directional coupling matrix  $\mathbf{C}_M$ . By comparison, the approach discussed in Section 3.1 deals with the coupling matrix  $\mathbf{C}$  which for the multiple multipath source case would have dimensions of  $K\bar{N} \times K\bar{N}$  where  $\bar{N}$  is the average number of reradiating elements needed to represent each multipath source. At the very least, when  $K < \bar{N}$ , the solution involving  $\mathbf{C}_M$  involves less computations. Additionally, considering  $\mathbf{C}_M$  is a sparse matrix (there are only  $K$  nonzero elements in each row of  $K(K - 1)$  elements), further computational savings are possible.

Additional savings can be achieved by ignoring coupling effects when they clearly have no significant effect on the final results. For example, consider two multipath sources,  $k$  and  $l$ , both along the direct signal path where the  $k^{th}$  multipath source is near the



transmitter and the  $l^{th}$  multipath source is near the receiver. The  $k^{th}$  multipath source will radiate a signal towards  $l^{th}$  which will travel a path of similar length to the direct signal. Since the  $l^{th}$  source will be in the main beam of this signal the losses will be related to the value of  $\beta'_k$  and the beamwidth. Given that the losses are minimized in this case, the effect of the  $k^{th}$  multipath source on the  $l^{th}$  multipath source needs to be considered. By comparison, the signal reradiated from the  $l^{th}$  multipath source will be considerably weaker. This reradiated signal involves the incident signal travelling from the transmitter to the  $l^{th}$  multipath source, followed by the reradiated signal travelling from  $l^{th}$  multipath source back to the  $k^{th}$ . A trip approximately double the length of the direct signal path resulting in a considerable attenuation of the reradiated signal. Additionally, the  $k^{th}$  reradiator will not be in the main beam of the reradiated signal (except for a very small multipath source), and unless there is a strong reflection beam, further attenuation will result. In this case, the effect of the  $l^{th}$  multipath source on the  $k^{th}$  multipath source could be ignored. In other words,  $s_{lk}$  can be set equal to zero (it will still be necessary to calculate  $s_{kl}$ , however).

Throughout the rest of this report, the preceding approach is referred to as the *multipath source coupling* method.

### 3.3.2 Internal Coupling

Under some conditions, particularly when the multipath sources are some distance from each other as well as from the transmitter and receiver, coupling effects between the multipath sources can be ignored. The received contribution from each multipath source can then be computed individually using an expression similar to (54). The individual contributions are then summed to get the total multipath signal at the receiver. Mathematically, this approach can be represented by

$$s_{mult} = s_{tx} \sum_{k=1}^K \mathbf{q}_k^T \mathbf{C}_k^{-1} \mathbf{p}_k \quad (82)$$

where  $\mathbf{p}_k$  and  $\mathbf{q}_k$  are the transmitter-reradiator and reradiator-receiver pathloss vectors associated with the  $k^{th}$  multipath source,  $\mathbf{C}_k$  is the coupling matrix for the reradiators composing the  $k^{th}$  multipath source, and  $K$  is the total number of multipath sources.

Since in the above approach only coupling effects within each multipath source are treated, it is called the *internal coupling* method.

### 3.3.3 Comparing Coupling Methods

To determine the utility and limitations of the methods developed thus far, a large number of comparative simulations were carried out. From these simulations, a few examples were chosen which best illustrate the strengths and weaknesses of the methods.

In the first simulation, the simulated multipath environment shown in Figure 23 was created. In this example, a single transmitter was moved through a distance of 80 meters while the receiver was left stationary. Two identical wall-like reradiator structures were used as the sources of multipath and were positioned along the direct signal path but well separated from each other. Since this example was chosen to illustrate shadowing effects, the shape of the multipath sources is not important. Size is, however, since the larger the size the smaller the main beam beamwidth (and the longer the shadow). In this case size was chosen to be representative of the side of a small building. The configuration of the two multipath sources is shown in Figure 24. For these multipath sources, the following parameters were also applicable:  $\beta = -1$ ,  $\mu_m = \lambda/5$ ,  $d = \mu_m$  (where  $d$  was the vertical and horizontal grid spacing). The transmitter signal had a wavelength of  $\lambda = 4.8\text{m}$ . The received multipath signal was calculated using three different methods and then combined with the calculated direct signal to give the total received signal. For display purposes, the amplitude values of the total received signal were plotted relative to the direct signal as shown in Figure 25a-c.

The results in Figure 25a were calculated using the the full coupling method (Section 3.1). Since the total number of reradiators was  $2 \times 14 \times 14 = 392$ , the computations for this method involved the inversion of a coupling matrix  $C_\alpha$  with dimensions  $392 \times 392$ . Given that (54) is the most complete form of the coupling equations, Figure 25a is used to compare the other methods.

The results in Figure 25b were calculated using the multipath source coupling method discussed in Section 3.3.1 since the multipath sources were sufficiently distant from each other that farfield approximations could be used. In this case the coupling matrix had dimensions of  $2 \times 2$  so that the main computations involved calculating the beamfunction of the individual multipath sources (which were identical in this case). This was done using (65) where  $C_\alpha$  represented the coupling of the reradiators in a single multipath source and had dimensions  $196 \times 196$ . Comparing the results of Figure 25b to Figure 25a shows the results to be nearly identical.

The results in Figure 25c were calculated using the internal coupling method (discussed

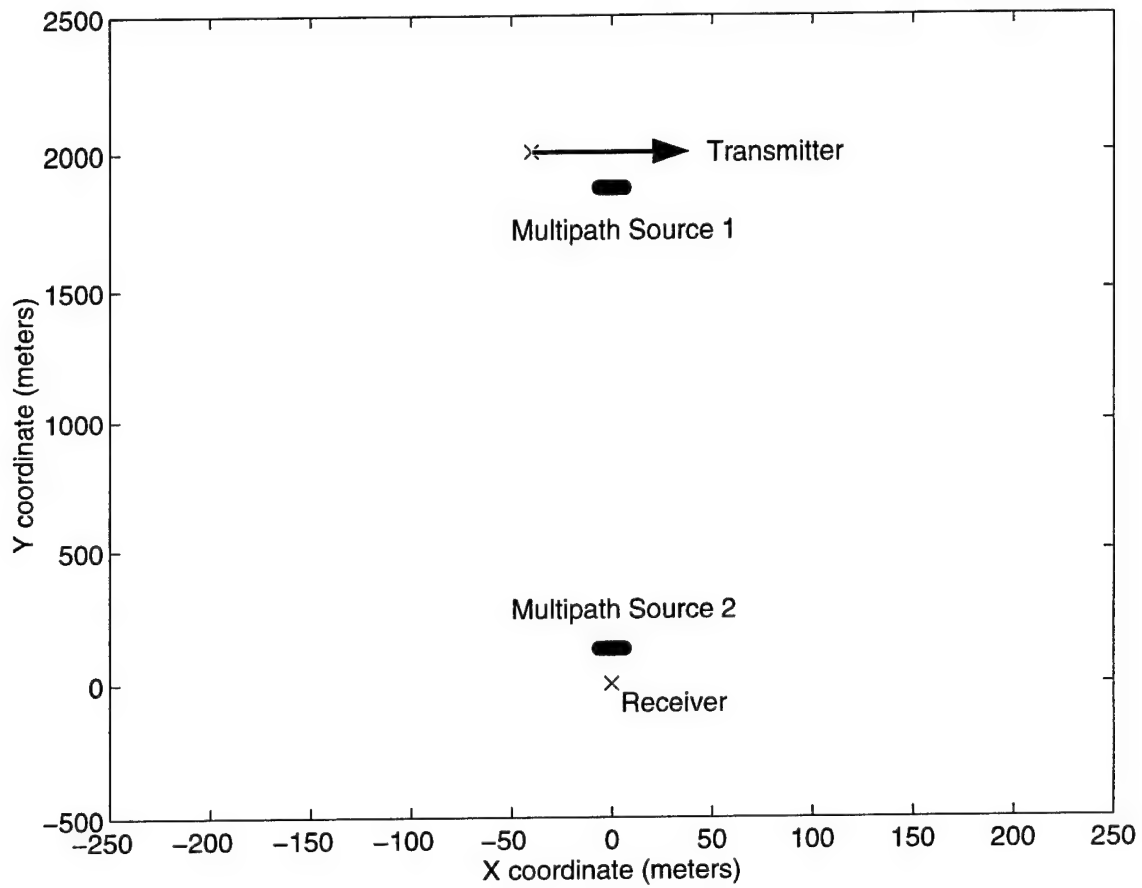


**Figure 23:** Map used for simulation purposes and showing the geometry of the transmitter, receiver, and two multipath sources.

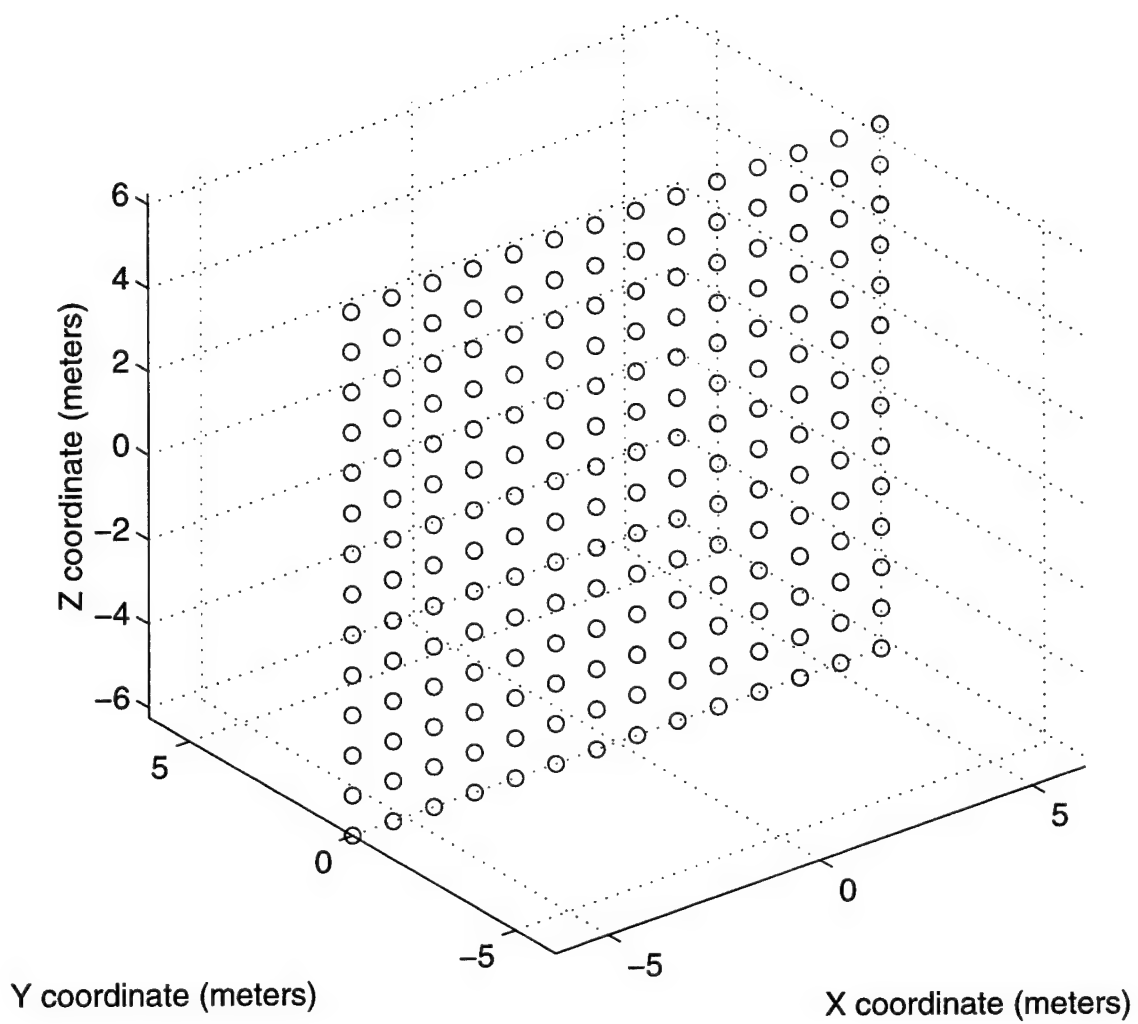
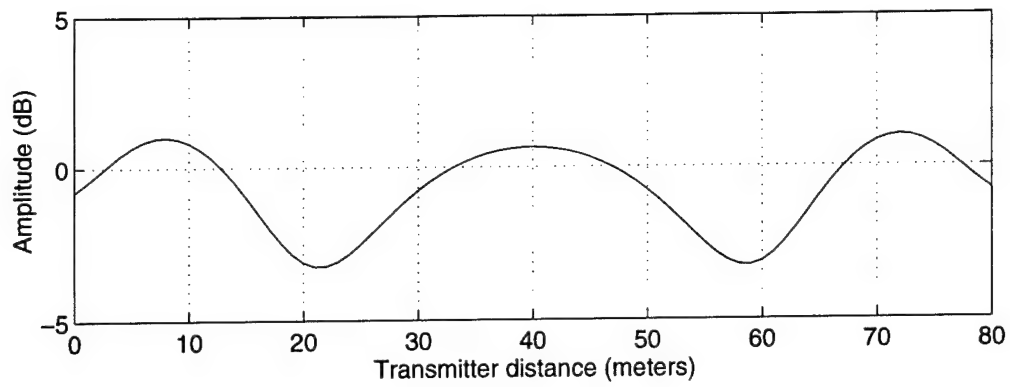
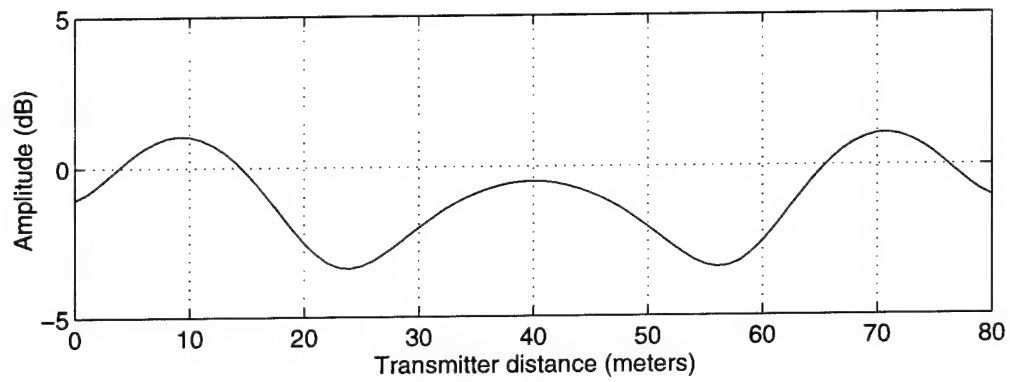


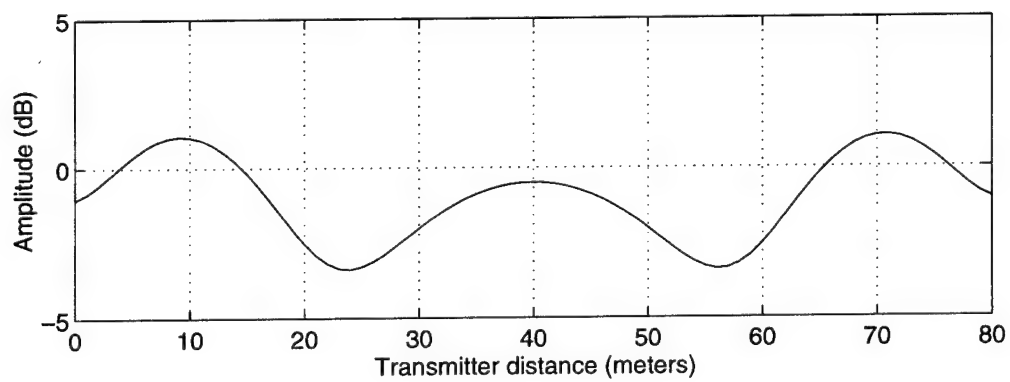
**Figure 24:** Configuration of reradiators used to create a wall-like multipath source.



(a)



(b)



(c)

**Figure 25:** Relative amplitude of signal at receiver calculated using (a) the full coupling method, (b) the multipath source coupling method, and (c) the internal coupling method.

in Section 3.3.2). Given the large separation between the two multipath sources, the approximations used in this method might at first appear justified. However comparing the results of Figure 25c with Figures 25a and b, reveals that the signal amplitude when the transmitter is at the middle of its path (40m) has been over-estimated. This is due to the fact that in this method multipath source 1 and 2 are assumed to contribute equally, whereas in fact, multipath source 1 shadows multipath source 2, so that the contribution from multipath source 2 should be less than multipath source 1. This shadowing effect could be reduced by ensuring that the multipath sources are not placed too close to the transmitter and receiver.

To investigate the question of accuracy versus spacing, the previous simulation was rerun a number of times while multipath source 1 and 2 were moved apart. Initially the two multipath sources were located close together near the center of the direct signal path as shown in Figure 26. The transmitter was then moved along the same path as before. By using the results of the full method as a reference, the mean squared error for the two other methods was computed using the expression

$$mse = \frac{\sum_i (x(i) - \hat{x}(i))^2}{\sum_i x(i)^2} \quad (83)$$

where  $x(i)$  was the received signal calculated for transmitter position  $i$  using the full method and  $\hat{x}(i)$  was the corresponding value calculated using one of the simpler methods. The multipath sources were then moved further apart and the process repeated giving the results shown in Figure 27. As might be expected, the results improve as the distance between the two multipath sources increases. The increase in error centered around a spacing of 2000 meters occurs because the multipath sources are in close proximity to the transmitter and receiver. This is a relatively small effect for the multipath source coupling method, but a major effect for the internal coupling method, emphasizing the remarks made earlier that the multipath sources cannot be placed too close to the transmitter and receiver if accurate results are desired using the internal coupling method.

Based on this and other simulations (involving different sized multipath sources, different relative positions, etc.), as well as the standard near-field/far-field boundary definition used in antenna theory (see for example [7]), a useful minimum spacing constraint is given by

$$\frac{4D^2}{\lambda} \quad (84)$$

(which is 2 times the standard near-field/far-field boundary definition). In the above

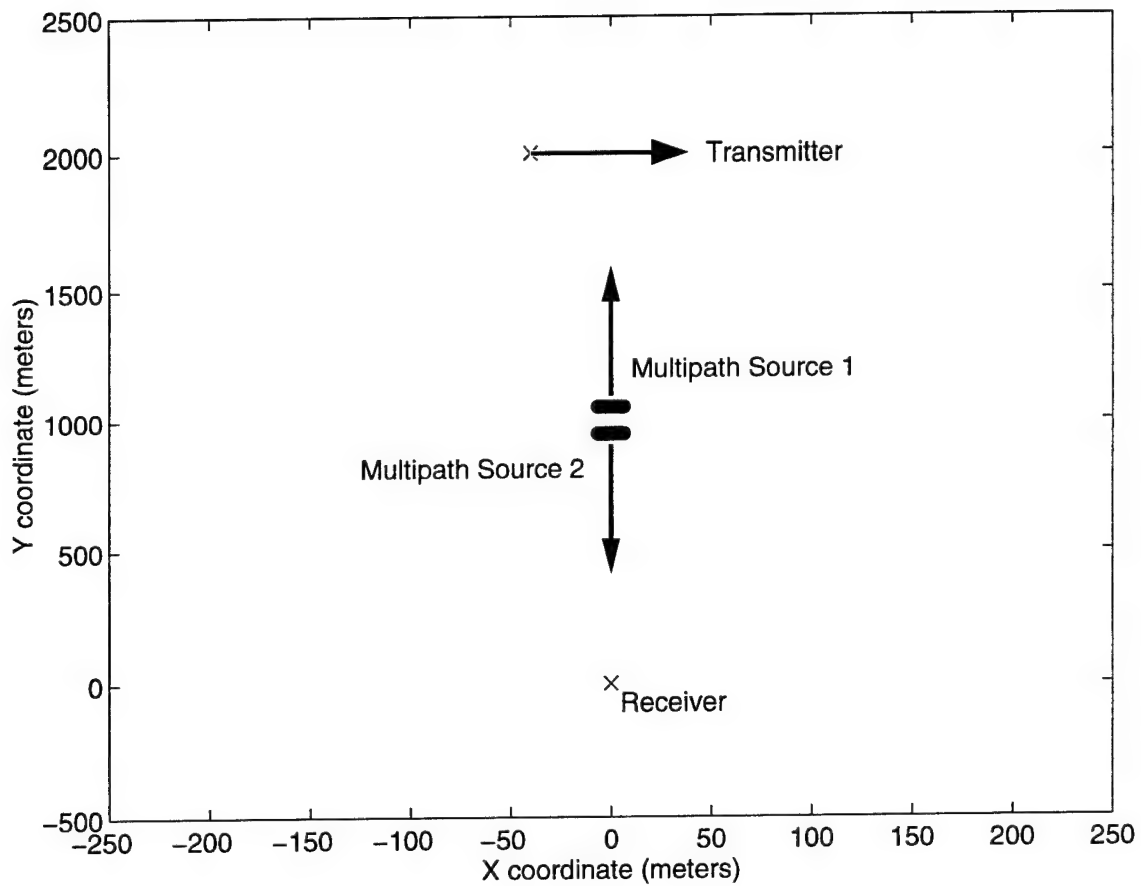


**Figure 26:** Map of locations of transmitter, receiver, and multipath sources used in simulation to investigate effect of spacing.

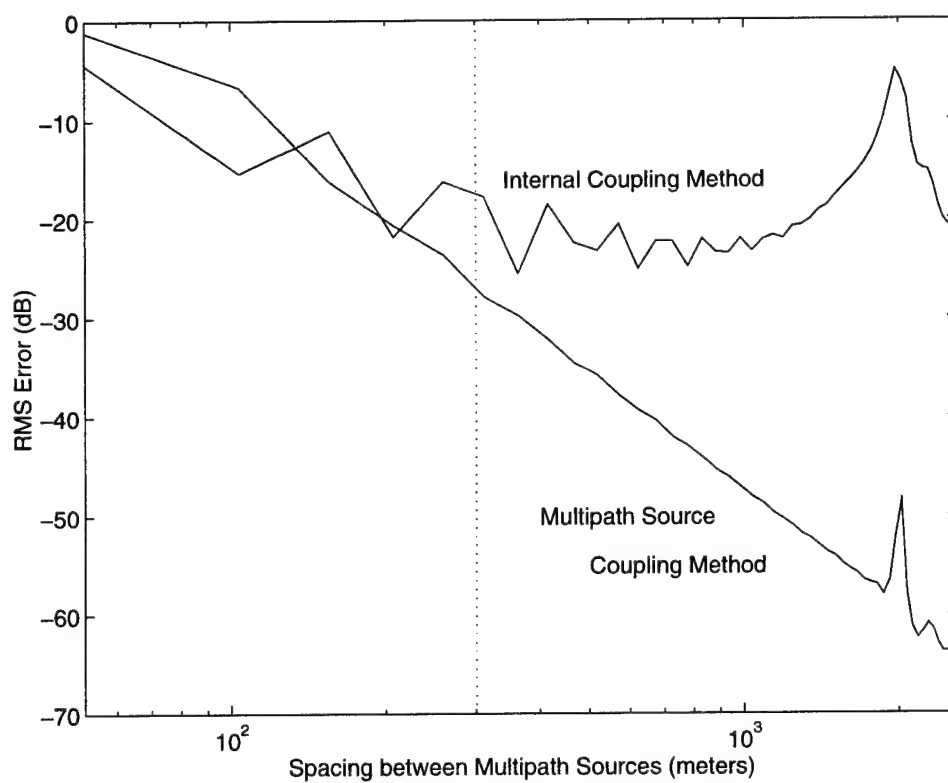


**Figure 27:** Mean squared error results for two approximate methods as a function of spacing between multipath sources.



expression  $D$  is the “aperture” of the multipath source which can be reasonably approximated by the largest dimension of the multipath source measured perpendicular to the signal direction (or more accurately determined using the approach discussed in Section 2.3.2. For example, for the multipath source model used to produce the results in Figures 25 and 27, and illustrated in Figure 24, the aperture was approximately 19 meters (measured diagonally). Based on this aperture, the minimum spacing constraint was calculated according to (84) and plotted as a vertical dotted line in Figure 27.

For this choice of minimum spacing between multipath sources, the error introduced by the multipath source method is less than 10% (-20 dB) of the total multipath signal. If this constraint is used to also include the spacing between the transmitter and the nearest multipath source, or the receiver and the nearest multipath source, the accuracy of the internal coupling method (relative to the full coupling method) will typically be below 20% (-14 dB).

A final example involving 7 multipath sources (the same wall-like structures as before except with dimensions of  $8 \times 8$  reradiators) and a moving transmitter is illustrated in Figure 28. The minimum spacing constraint was employed when placing the multipath sources near each other or near the transmitter or receiver. The results are shown in Figure 29, and as would be expected, the multipath source coupling method gives almost exactly the same results as the full method, and the source coupling gives results which are only slightly different.

For spacings appreciably less than  $\frac{4D^2}{\lambda}$  the performance of the multipath source coupling method (as well as the internal coupling method) rapidly degrade as near-field effects begin to dominate. For these smaller spacings, more work needs to be done on the development of computationally efficient and accurate approaches.

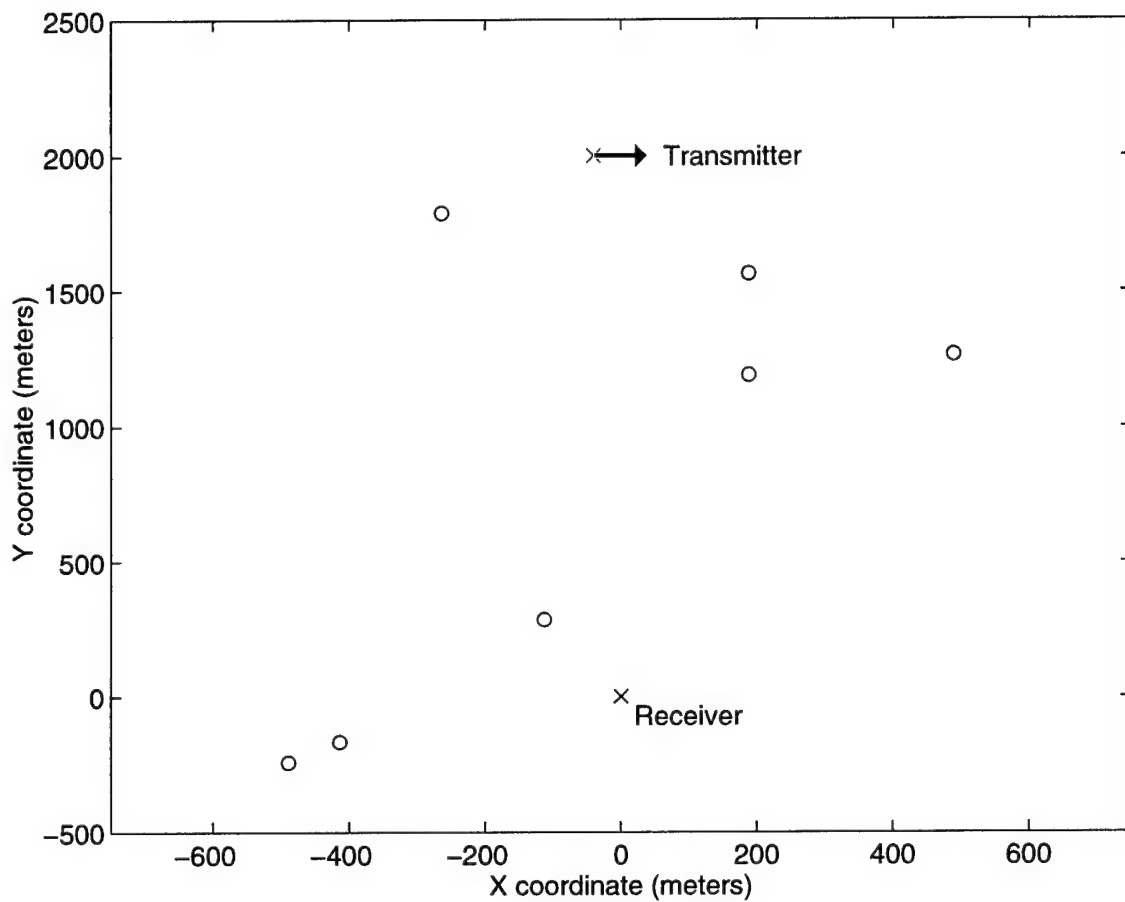
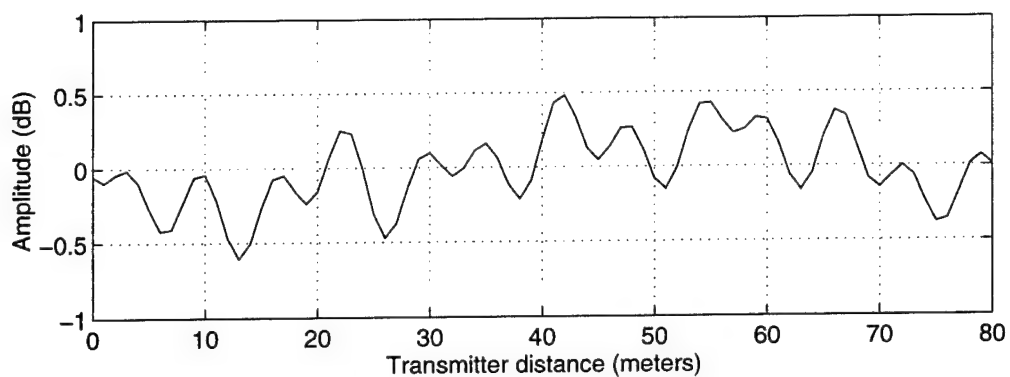
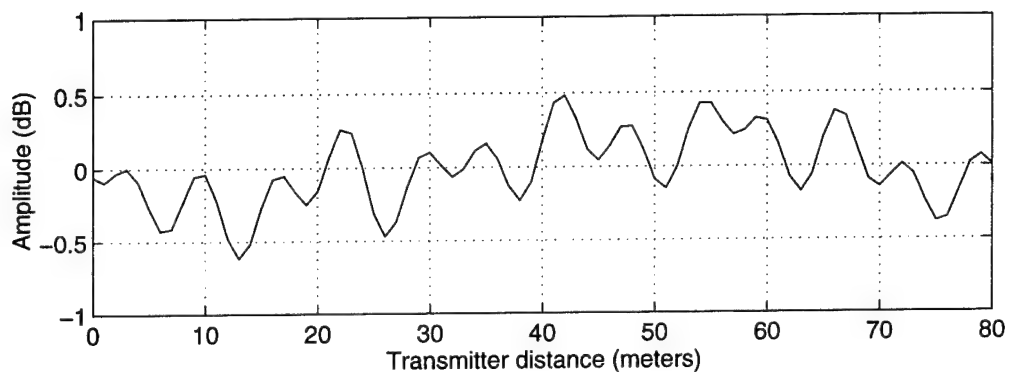


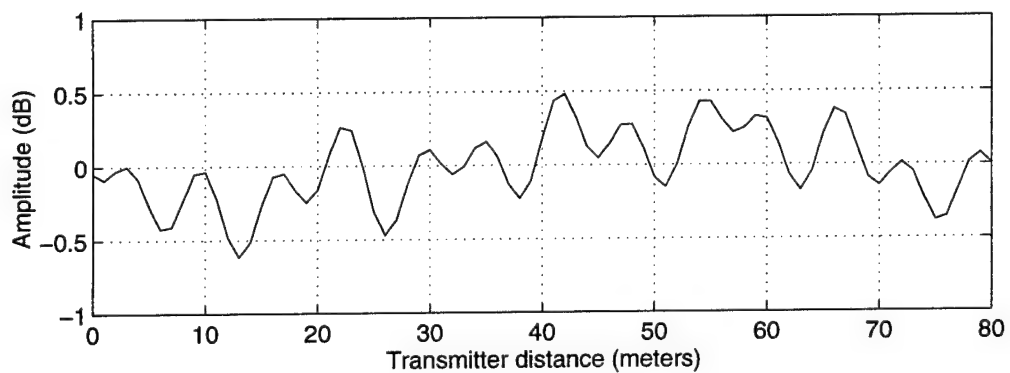
**Figure 28:** Map showing setup used for multipath simulation involving seven multipath sources (denoted by 'o').



(a)



(b)



(c)

**Figure 29:** Multipath simulation showing relative amplitude of signal at the receiver calculated using (a) the full coupling method, (b) the multipath source coupling method, and (c) the internal coupling method.

## 4.0 THE GROUND PLANE

Up until this point, freespace propagation has been assumed. For the exact solutions, the most significant expressions are embodied by (15) for the case of a single reradiator, and (54) for the case of a collection of reradiators. In the case of terrestrial propagation, reflections of the signal off the ground play a significant role. Although the freespace equations could be used in this case, the sheer size of the ground introduces a prohibitive number of computations into the modelling problem. For example, using a spacing between reradiators of  $\lambda/10$ , a grid representing a small patch of ground with dimensions  $10\lambda \times 10\lambda$  would require 10,000 reradiators. Determining coupling effects would then require inverting a  $10,000 \times 10,000$  matrix – by no means a simple computation! As the patch size is increased, the computational requirements quickly gets out-of-hand.

An alternate approach employed here is to consider the ground as an infinite, perfectly flat, and perfectly reflecting plane. Imperfections can then be introduced into this plane to model the effects of terrain features, vegetation, and variations in the dielectric constant of the ground. Ideally, once the characteristics of a perfect ground plane have been determined and understood, it remains only to model the effects of the imperfections and not the entire ground.

In the next section, the properties of an ideal ground plane are determined using large flat grids of reradiators and extrapolating from the results. Once the characteristics of an ideal ground have been determined, the effects of elevation, vegetation, and changes in the dielectric constant of the ground are analyzed and discussed in the following two sections (Sections 4.2 and 4.3).

Note that the discussion and analysis of multipath effects is limited to considering either terrain/vegetation effects, or variations in the dielectric constant of a flat ground. In particular, for terrain effects, the ground is assumed to remain perfectly reflecting. This simplifies the mathematics since solving for terrain effects and variations in the dielectric constant of the ground would require a more rigorous (and extremely difficult) treatment based on Maxwell's equations.

### 4.1 The Ideal Ground Plane

The ideal ground plane is defined here as a perfectly flat, perfectly reflecting plane. Figure 30 illustrates the reflected signal from an ideal ground plane. Letting this plane be

represented by an infinite grid of reradiators, the reradiation coefficients of the individual reradiators can be determined by considering that below the ground plane, no signal exists. Since the signal reradiated by the ground plane will be symmetric above and below the surface of the plane (i.e. the reflected signal and the signal marked by the dashed line in Figure 30), the signal reradiated by the ground plane at and below the surface will be exactly cancelled out by the direct signal. The reradiated signal must therefore be of equal amplitude but  $180^\circ$  out of phase with the direct signal, i.e. the reradiation coefficient  $\beta_k = -1$  for all values of  $k$ .

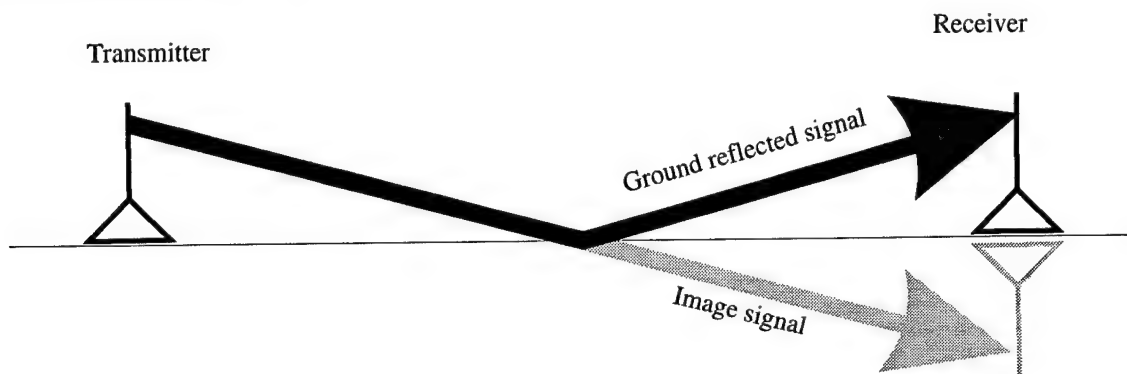


**Figure 30:** Ideal ground plane showing direct and reflected signals.

Having established the reradiation coefficients associated with an ideal ground plane, the flat circular grid shown in Figure 31 is now considered. A transmitter, located above the center of this grid, radiates a signal outward. The incident signal at each reradiator is the sum of the transmitter signal plus the reradiated signals from all the other reradiators. To determine the reradiated signals, equation (54) could be used, however as pointed out previously, the computational requirements become prohibitive for large grids. This problem can be overcome somewhat by recognizing that the grid in Figure 31 has circular symmetry so that the incident and reradiated signals for any reradiator at a distance  $r$  from the center of the grid will be the same as any other reradiator that is also at distance  $r$  from the center. A grid with a radius of  $10\lambda$  would then only require inversion of a  $100 \times 100$  matrix (assuming  $\lambda/10$  spacing).

Figure 32 shows the results generated using this simplifying approach for a grid with a radius of  $10\lambda$ , a grid spacing of  $\lambda/100$ , and a transmitter height of  $0.1\lambda$ . The reradiated signal is well behaved as a function of range, except towards the edge of the grid. Based on this and other simulations where the transmitter height ( $h_a$ ), grid spacing ( $d$ ), and

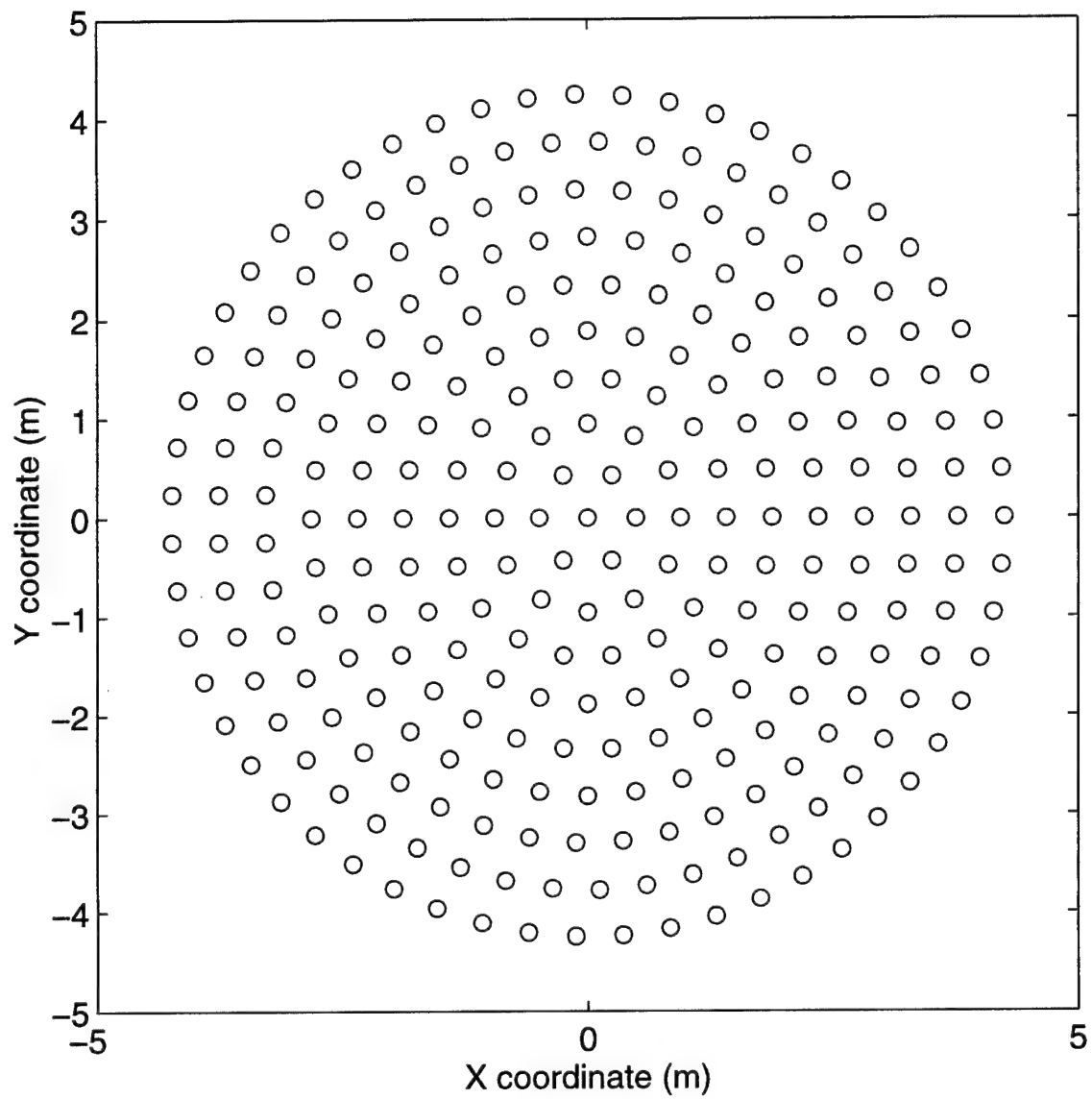


**Figure 31:** Geometry of a circular grid used for ground simulations.

reradiator collection area ( $\mu_m$ ), were varied, the following approximation was developed

$$s_{grid} = -s_{tx} \frac{\mu_m^2 h_a}{\lambda} \left( \frac{j}{r_a^2} + \left(1 - \frac{2\mu_m h_a}{\lambda^2}\right) \frac{\lambda}{2\pi r_a^3} \right) e^{-j\frac{2\pi}{\lambda} r_a} \quad (85)$$

A more accurate approximation would also contain a small real component in the  $r^{-2}$  term resulting in a term of the form  $(j - \kappa\mu^2)/r_a^2$ . Since this component rapidly disappears as  $\mu_m \rightarrow 0$ , it is considered to be an error resulting from the quantization of a continuous medium (the ground) and is therefore ignored.

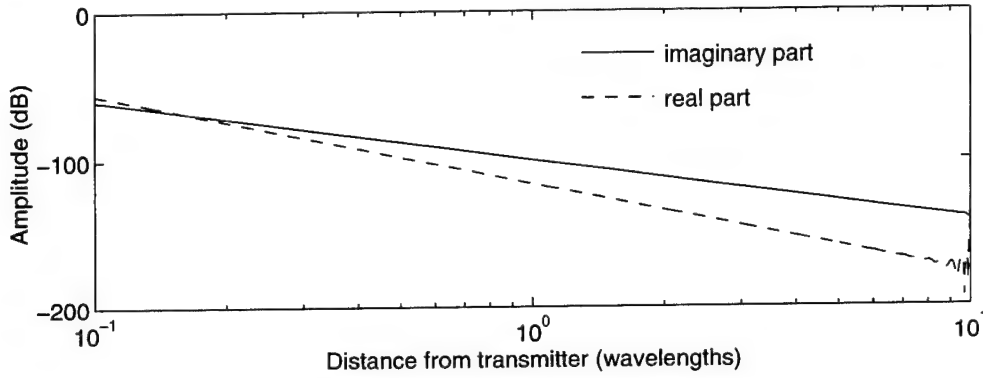


**Figure 32:** Results of ground simulation for  $\beta = -1$  showing the magnitude of the reradiator signals as a function of distance from the transmitter. The magnitude of both the real and imaginary parts of these signals are plotted relative to the magnitude of the incident transmitter signal. A logarithmic scale has been used for the X-axis to illustrate the  $r^N$  relationship between signal magnitude and distance from the transmitter.

The matrix equation for the signals reradiated from a collection of reradiators was developed in the previous section (equation (52)). With slight modifications, the expression for the ground grid is repeated here as

$$\mathbf{s}_i = s_{tx} \mathbf{C}_i^{-1} \mathbf{p}_i \quad (86)$$

where the subscript  $i$  has been used to denote values associated with an ideal ground plane. Using the results from (85), the solution for the elements of  $\mathbf{s}_i$  is given by

$$s_{ik} = -s_{tx} \frac{\mu_m^2 h_a}{\lambda} \left( \frac{j}{r_{ak}^2} + \left(1 - \frac{2\mu_m h_a}{\lambda^2}\right) \frac{\lambda}{2\pi r_{ak}^3} \right) e^{-j\frac{2\pi}{\lambda} r_{ak}} \quad (87)$$

where  $r_{ak}$  represents the distance from the transmitter to the  $k^{th}$  reradiator.

At the receiver, the signal due to the grid reradiators can be computed using (54) to

give

$$s_{ri} = s_{tx} \mathbf{q}_i^T \mathbf{C}_i^{-1} \mathbf{p}_i \quad (88)$$

Incorporating the results given in (87), and the definition for the elements of  $\mathbf{q}_i$  (53), then the solution is given by the summation of the individual paths

$$s_{ri} = -s_{tx} \sum_k \frac{\mu_m^2 \mu_r h_a}{2\sqrt{\pi} \lambda r_{bk}} \left( \frac{j}{r_{ak}^2} + \left(1 - \frac{2\mu_m h_a}{\lambda^2}\right) \frac{\lambda}{2\pi r_{ak}^3} \right) e^{-j\frac{2\pi}{\lambda}(r_{ak}+r_{bk})} \quad (89)$$

Alternatively, the solution for  $s_{ri}$  can also be computed by considering the fact that since the ground grid was set up to be a perfect reflector, the resultant received signal will be the same as a direct (unreflected) signal which travels a path of the same length but with a  $180^\circ$  phase reversal (due to the reflection). This leads to,

$$s_{ri} = s_{tx} \rho_{\alpha r}(r_i) \quad (90)$$

where the path length is given by

$$r_i = \sqrt{(r_a + r_b)^2 + (h_a + h_b)^2} \quad (91)$$

Given the derivation for the ideal ground plane grid, it is useful at this point to provide a mathematical definition of multipath. As mentioned in the introduction, reflections off the ground plane are an unavoidable consequence of terrestrial propagation. Hence, multipath is defined as the difference between the actual received signal and the received signal in the ideal case, or

$$s_{mult} = s_{receiver} - s_{ideal} \quad (92)$$

Since the direct signal is the same in the ideal and nonideal cases, then multipath reduces to the difference between the received grid signals in the two cases. Mathematically

$$s_{mult} = s_{rg} - s_{ri} \quad (93)$$

where  $s_{rg}$  is the actual signal received from the ground grid (including multipath sources). Exploring ways to simplify the above expression, given different assumptions about the ground, is the topic of the next section.



## 4.2 Vegetation and Terrain Features

In this section, vegetation and terrain effects are considered. Figure 33 illustrates an example consisting of a single multipath source, a tree in this case, located on top of an ideal ground plane. The relevant signal paths have also been shown. This situation is considerably more complex than in the freespace cases discussed in Section 2.0 due to the presence of the ground. In the freespace case, there are only the transmitter-multipath source and multipath source-receiver signals ( $s_a$  and  $s_b$ ) to contend with. With the ground plane, these two signals are joined by their corresponding reflections off the ground plane ( $s'_a$  and  $s'_b$ ) plus a reflection of the reradiated signal off the ground plane back to the reradiator ( $s'_c$ ). The situation becomes even more complicated when more than one isotropic element is used to model the multipath source or more than one multipath source is involved.

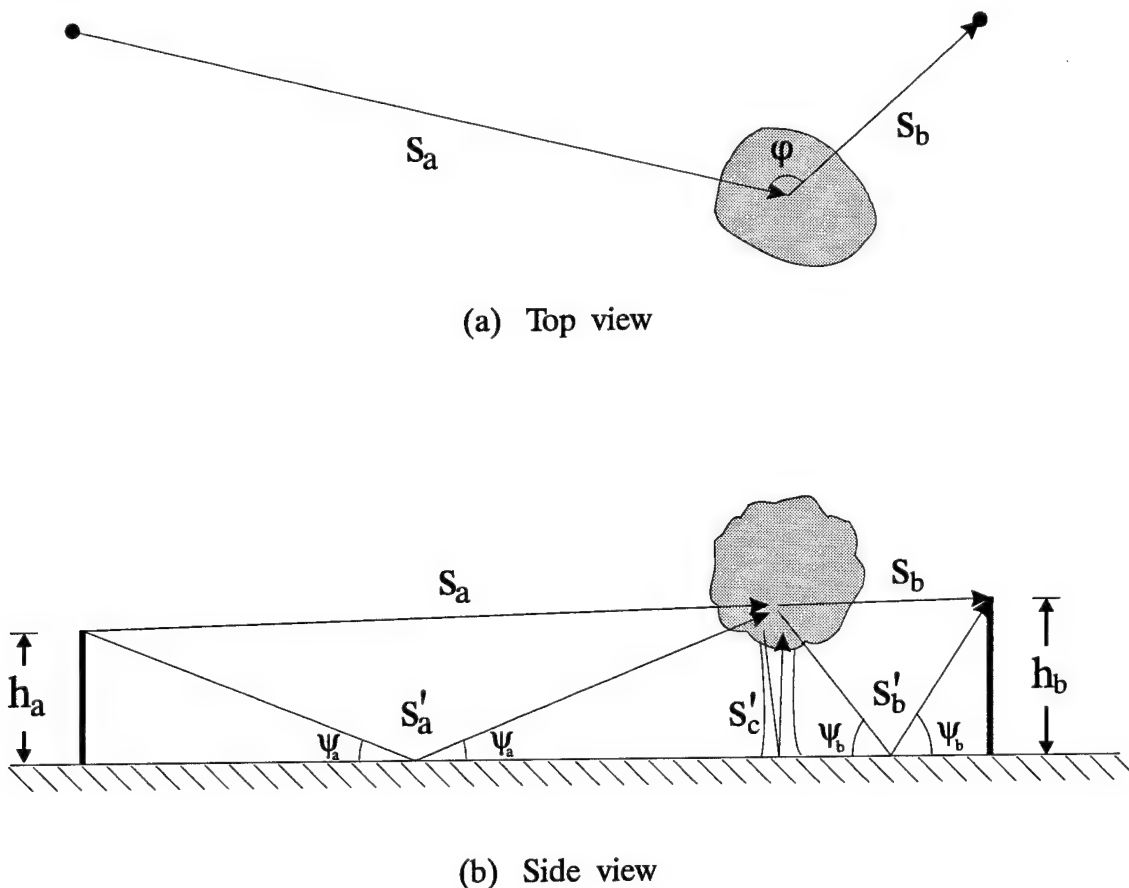


**Figure 33:** Above ground multipath source model.

To tackle this problem, the ground is again assumed to consist of a giant grid of

isotropic reradiators. In the absence of any multipath sources, the received signal is given by (88) which is repeated here as,

$$s_{ri} = s_{tx} \mathbf{q}_i^T \mathbf{C}_i^{-1} \mathbf{p}_i \quad (94)$$

If vegetation and/or terrain features exist on top of or above (not below) the ground plane, then each feature can be modelled by collections of isotropic reradiators. The received signal in this case is given by the freespace equation, namely,

$$s_{rg} = s_{tx} \mathbf{q}_\alpha^T \mathbf{C}_\alpha^{-1} \mathbf{p}_\alpha \quad (95)$$

This expression gives very little insight into the effect of the new reradiators so that it is useful to re-express  $\mathbf{p}_\alpha$ ,  $\mathbf{q}_\alpha$ , and  $\mathbf{C}_\alpha$ , in terms of the ideal ground parameters  $\mathbf{p}_i$ ,  $\mathbf{q}_i$ , and  $\mathbf{C}_i$ . Accordingly,  $\mathbf{p}_\alpha$  becomes

$$\mathbf{p}_\alpha = \begin{bmatrix} \mathbf{p}_i \\ \mathbf{p}_m \end{bmatrix} \quad (96)$$

the attenuation vector  $\mathbf{q}_i$  becomes

$$\mathbf{q}_\alpha = \begin{bmatrix} \mathbf{q}_i \\ \mathbf{q}_m \end{bmatrix} \quad (97)$$

and the coupling matrix  $\mathbf{C}$  becomes

$$\mathbf{C}_\alpha = \begin{bmatrix} \mathbf{C}_i & \mathbf{M} \\ \mathbf{M}^T & \mathbf{C}_m \end{bmatrix} \quad (98)$$

where  $\mathbf{M}$  represents the coupling between the new reradiators and the ground plane, and  $\mathbf{C}_m$  represents the mutual coupling between the new reradiators.

The inversion of the expanded form of  $\mathbf{C}$  can be accomplished using the matrix inversion formula [9] which is repeated here as

$$\begin{bmatrix} \mathbf{A} & \mathbf{D} \\ \mathbf{C} & \mathbf{B} \end{bmatrix}^{-1} = \begin{bmatrix} \mathbf{A}^{-1} + \mathbf{A}^{-1} \mathbf{D} \mathbf{\Delta}^{-1} \mathbf{C} \mathbf{A}^{-1} & -\mathbf{A}^{-1} \mathbf{D} \mathbf{\Delta}^{-1} \\ -\mathbf{\Delta}^{-1} \mathbf{C} \mathbf{A}^{-1} & \mathbf{\Delta}^{-1} \end{bmatrix} \quad (99)$$

where  $\Delta = \mathbf{B} - \mathbf{C}\mathbf{A}^{-1}\mathbf{D}$ . Applying this formula to  $\mathbf{C}$  then

$$\mathbf{C}^{-1} = \begin{bmatrix} \mathbf{C}_i^{-1} + \mathbf{C}_i^{-1}\mathbf{M}\mathbf{R}^{-1}\mathbf{M}^T\mathbf{C}_i^{-1} & -\mathbf{C}_i^{-1}\mathbf{M}\mathbf{R}^{-1} \\ -\mathbf{R}^{-1}\mathbf{M}^T\mathbf{C}_i^{-1} & \mathbf{R}^{-1} \end{bmatrix} \quad (100)$$

In this expression  $\mathbf{R}$  is given by

$$\mathbf{R} = \mathbf{C}_m - \mathbf{M}^T\mathbf{C}_i^{-1}\mathbf{M} \quad (101)$$

Before continuing, the expression for  $\mathbf{R}$  deserves closer attention. The first term obviously represents the mutual coupling among the new reradiators. The second term is not so readily classified, however some insight can be gained by first representing it as

$$\mathbf{C}'_m = \mathbf{M}^T\mathbf{C}^{-1}\mathbf{M} \quad (102)$$

Next,  $c_{kn}$ , the element in the  $k^{th}$  row and  $n^{th}$  column of  $\mathbf{C}'_m$  is given by

$$c_{kn} = \mathbf{m}_k^T\mathbf{C}_i^{-1}\mathbf{m}_n \quad (103)$$

where  $\mathbf{m}_k$  and  $\mathbf{m}_n$  represent the  $k^{th}$  and  $n^{th}$  columns of  $\mathbf{M}$  respectively. Given that  $\mathbf{m}_k$  and  $\mathbf{m}_n$  are attenuation vectors of the same form as  $\mathbf{p}_i$  and  $\mathbf{q}_i$  in (94), and that  $\mathbf{C}_i$  represents an ideal ground plane, then the above expression represents the attenuation of a signal emitted by the  $n^{th}$  reradiator, reflected off the ground plane, and then received by the  $m^{th}$  reradiator. More precisely, (103) gives the freespace attenuation from the  $n^{th}$  reradiator to the image of the  $k^{th}$  reradiator. From this, it is readily apparent that  $\mathbf{C}'_m$  represents the coupling between the new reradiators and their images in the ground plane.

Based on the expansions for  $\mathbf{p}_\alpha$ ,  $\mathbf{q}_\alpha$ , and  $\mathbf{C}_\alpha$ , equation (95) becomes

$$\begin{aligned} s_{rg} = s_{tx} & \left( \mathbf{q}_i^H\mathbf{C}_i^{-1}\mathbf{p}_i + \mathbf{q}_i^H\mathbf{C}_i^{-1}\mathbf{M}\mathbf{R}^{-1}\mathbf{M}^T\mathbf{C}_i^{-1}\mathbf{p}_i - \mathbf{q}_m^H\mathbf{C}_i^{-1}\mathbf{M}\mathbf{R}^{-1}\mathbf{p}_m \right. \\ & \left. - \mathbf{q}_m^H\mathbf{R}^{-1}\mathbf{M}^T\mathbf{C}_i^{-1}\mathbf{p}_i + \mathbf{q}_m^H\mathbf{R}^{-1}\mathbf{p}_m \right) \end{aligned} \quad (104)$$

The form of this expression suggests some further definitions. The first is

$$\mathbf{p}'_m = \mathbf{M}^T\mathbf{C}_i^{-1}\mathbf{p}_i \quad (105)$$

where  $\mathbf{p}'_m$  represents the attenuation from the transmitter to the images of the new reradiators. Similarly

$$\mathbf{q}'_m = \mathbf{M}^T \mathbf{C}_i^{-1} \mathbf{q}_i \quad (106)$$

where  $\mathbf{q}'_m$  represents the attenuation from the new reradiators to the receiver. Using these definition, and the fact that the first term on the right hand side of (104) is the ideal ground reflected signal  $s_{ri}$ , then

$$s_{rg} = s_{ri} + s_{tx} \left( \mathbf{q}'_m{}^H \mathbf{R}^{-1} \mathbf{p}'_m - \mathbf{q}'_m{}^H \mathbf{R}^{-1} \mathbf{p}_m - \mathbf{q}_m{}^H \mathbf{R}^{-1} \mathbf{p}'_m + \mathbf{q}_m{}^H \mathbf{R}^{-1} \mathbf{p}_m \right) \quad (107)$$

Replacing  $\mathbf{R}$  by  $\mathbf{C}_m - \mathbf{C}'_m$  and reorganizing yields

$$s_{rg} = s_{ri} + (\mathbf{q}_m - \mathbf{q}'_m)^T (\mathbf{C}_m - \mathbf{C}'_m)^{-1} (\mathbf{p}_m - \mathbf{p}'_m) \quad (108)$$

Using the previous definition for multipath (93) then

$$s_{mult} = (\mathbf{q}_m - \mathbf{q}'_m)^T (\mathbf{C}_m - \mathbf{C}'_m)^{-1} (\mathbf{p}_m - \mathbf{p}'_m) \quad (109)$$

The advantage of this form (compared to (93)) is that it involves only the new reradiators and their images – calculations involving the ground grid reradiators are not required. Assuming that the ground plane is not completely covered in vegetation and/or terrain features, this results in a considerable savings in computations. An important constraint when using this approach is that all features must be above the ground plane (not below) – the ground plane must represent the lowest point in elevation. Hence modelling a small depression on an otherwise flat plane will result in very little computational savings since the ground plane must be at the same elevation or below the bottom of the depression.

Equation (109) is very similar in form to the freespace version (54). In fact, the differences in the two expressions can be isolated to the difference in the determination of the attenuations and the reradiation coefficients. In the presence of a ground plane the freespace attenuation function  $\rho_\alpha(r)$  is replaced by the *elevated earth* attenuation function given by

$$\rho_z(r) = \rho_\alpha(r) - \rho_\alpha(r') \quad (110)$$

where  $r$  is the distance from the transmitting to the receiving element and is the corresponding distance to the image given, or

$$r' = \sqrt{r^2 + 4hz} \quad (111)$$

where  $h$  is the height of the transmitting element and  $z$  is the height of the receiving element. The ground plane attenuation function definitions  $\rho_{zm}(\cdot)$  and  $\rho_{zr}(\cdot)$  are also used to differentiate between the transmitter-reradiator (or reradiator-reradiator) path and the reradiator-receiver path. For cases where  $r \gg h, z$  the following power series approximation can be used

$$\rho_z(r) = \frac{2\sqrt{\pi}\mu h z}{\lambda} \left( \frac{j}{r^2} + \left(1 + \frac{4\pi^2 h z}{\lambda^2}\right) \frac{\lambda}{2\pi r^3} \right) e^{-j\frac{2\pi}{\lambda}r} \quad (112)$$

(where the above expression was derived using the software package Mathematica [11]). By inspection, it is apparent that for increasing distances  $r$ , the presence of the ground plane increases attenuation from  $r^{-1}$  to  $r^{-2}$  and introduces a  $90^\circ$  phase shift.

The freespace reradiation coefficient  $\beta$  can also be replaced by the effective elevated earth reradiation coefficient given by

$$\beta_z = \frac{\beta}{1 + \beta\rho_{\alpha m}(2z)} \quad (113)$$

where  $z$  is the height of the receiving element above the ground plane. The modification to the reradiation coefficient is caused by coupling of the receive element with its image in the ground plane, consequently as  $z$  becomes larger,  $\beta_z$  moves towards its freespace counterpart  $\beta$ .

Using the preceding definitions for the attenuation and effective reradiation coefficient, any of the methods described in Sections 2.0 or 3.0 can be used simply by substituting  $\rho_\alpha(r)$  and  $\beta$  by  $\rho_z(r)$  and  $\beta_z$  respectively. For example, (109) can be represented by

$$s_{mult} = \mathbf{q}_z^T \mathbf{C}_z^{-1} \mathbf{p}_z \quad (114)$$

where, after making the appropriate substitutions, the elements of the elevated earth attenuation vectors  $\mathbf{q}_z$  and  $\mathbf{p}_z$  are computed using (49) and (53) respectively, and the elements of the elevated earth coupling matrix  $\mathbf{C}_z$  are computed using (50) and (51).

### 4.3 Variations in the Reradiation Properties

To model variations in the electrical properties of the ground, the ground is again represented by a flat grid of isotropic reradiators. Unlike the ideal ground grid, however, the values of the reradiation coefficient are allowed to vary. This modifies the boundary

conditions at the ground-air interface, much the same thing that happens if the resistance or dielectric properties of the ground vary in the real world. No attempt is made here to relate the values of the reradiation coefficients to the corresponding dielectric and resistance values of the ground since in the real world these values are rarely known to any degree of precision. It is assumed instead, that the reradiation coefficients can be adjusted to reproduce the same effects observed in real world propagation and DF experiments (see the examples in Section 6.0).

Since the location of the ground grid reradiators is not modified, only the reradiation coefficients, the solution for the received signal is easily derived from the coupling equation (54) and is given by

$$s_{rg} = s_{tx} \mathbf{q}_i^T \mathbf{C}^{-1} \mathbf{p}_i \quad (115)$$

where in this case  $\mathbf{C}$  represents the coupling matrix for the grid where the reradiation coefficients have been modified.

To shed more light on the ramifications of this expression, the coupling matrix is divided into an ideal component and a difference component

$$\mathbf{C} = \mathbf{C}_i + \Delta_c \quad (116)$$

where  $\Delta_c$  represents the difference between the actual coupling matrix and the ideal one. If the reradiators are numbered so that the first  $K$  reradiators (out of a total of  $N$ ) are modified, then  $\Delta_c$  can be represented by

$$\Delta_c = \mathbf{U} \mathbf{\Upsilon} \mathbf{U}^T \quad (117)$$

where  $\mathbf{U}$  is a  $N \times K$  matrix with all ones in the main diagonal and zeros everywhere else, and  $\mathbf{\Upsilon}$  is a  $K \times K$  diagonal matrix whose diagonal elements are given by  $v_1, v_2, \dots, v_K$  using the definition  $v_k = -1 - \beta_k^{-1}$ . The inversion of  $\mathbf{C}$  can be carried out by taking advantage of another variant of the matrix inversion formula given by [9]

$$(\mathbf{A} + \mathbf{BCD})^{-1} = \mathbf{A}^{-1} - \mathbf{A}^{-1} \mathbf{B} (\mathbf{D} \mathbf{A}^{-1} \mathbf{B} + \mathbf{C}^{-1})^{-1} \mathbf{D} \mathbf{A}^{-1} \quad (118)$$

where  $\mathbf{A}$  and  $\mathbf{C}$  are invertible. Using the above equality, along with the relationships expressed in (116) and (117), the received grid signal given by (115) becomes,

$$s_{rg} = s_{tx} \mathbf{q}_i^T \mathbf{C}_i^{-1} \mathbf{p}_i - s_{tx} \mathbf{q}_i^T \mathbf{C}_i^{-1} \mathbf{U} (\mathbf{U}^T \mathbf{C}_i^{-1} \mathbf{U} + \mathbf{\Upsilon}^{-1})^{-1} \mathbf{U}^T \mathbf{C}_i^{-1} \mathbf{p}_i \quad (119)$$

At this point some simplifications are in order. The first is the recognition that the first term on the righthand side of (119) is the ideal received signal,  $s_{ri}$ . A second simplification is the two new definitions

$$\mathbf{p}_\epsilon = -\mathbf{U}^T \mathbf{C}_i^{-1} \mathbf{p}_i \quad (120)$$

and

$$\mathbf{q}_\epsilon = -\mathbf{U}^T \mathbf{C}_i^{-1} \mathbf{q}_i \quad (121)$$

where  $\mathbf{p}_\epsilon$  and  $\mathbf{q}_\epsilon$  are the *dielectric* propagation vectors for the modified reradiators (the first  $K$  reradiators) in the grid. The inclusion of the minus signs has no affect on the calculation of  $s_{rg}$ , but results in a set of expressions which are consistent with previously developed expressions. The quantity  $s_{tx} \mathbf{C}_i^{-1} \mathbf{p}_i$  was defined earlier as  $\mathbf{s}_i$ , so that  $\mathbf{U}^T \mathbf{C}_i^{-1} \mathbf{p}_i$  represents the first  $K$  elements of this vector divided by  $s_{tx}$ . The elements of  $\mathbf{s}_i$  were also determined earlier (equation (86)), consequently the  $k^{th}$  element of  $\mathbf{p}_\epsilon$  can be approximated by

$$p_{\epsilon k} = \frac{\mu_m^2 h_a}{\lambda} \left( \frac{j}{r_{ak}^2} + \left(1 - \frac{2\mu_m h_a}{\lambda^2}\right) \frac{\lambda}{2\pi r_{ak}^3} \right) e^{-j\frac{2\pi}{\lambda} r_{ak}} \quad (122)$$

where  $k = 1, 2, \dots, K$ . In a similar fashion, the  $k^{th}$  element of  $\mathbf{q}_\epsilon$  can be approximated by

$$q_{\epsilon k} = \frac{-\mu_m \mu_r h_b}{\lambda} \left( \frac{j}{r_{bk}^2} + \left(1 - \frac{2\mu_m h_b}{\lambda^2}\right) \frac{\lambda}{2\pi r_{bk}^3} \right) e^{-j\frac{2\pi}{\lambda} r_{bk}} \quad (123)$$

where  $r_{bk}$  represents the distance from the  $k^{th}$  reradiator to the receiver, and  $h_b$  is the height of the receiving antenna.

In addition to these definitions, one further definition is in order, namely

$$\mathbf{C}_G = \mathbf{U}^T \mathbf{C}_i^{-1} \mathbf{U} \quad (124)$$

This matrix  $\mathbf{C}_G$  is a  $K \times K$  submatrix of  $\mathbf{C}^{-1}$  containing the first  $K$  rows and first  $K$  columns of  $\mathbf{C}^{-1}$ . Since a simple expression for the elements of  $\mathbf{C}_i^{-1}$  is unknown, a reasonable approach would be to approximate  $\mathbf{C}_i$  by  $\hat{\mathbf{C}}_i$  using a grid of finite (instead of infinite) extent, but several times larger than the portion of the grid embodied by  $\mathbf{C}_G$ . To avoid edge effects,  $\mathbf{C}_G$  could then be taken from the part of  $\hat{\mathbf{C}}_i^{-1}$  corresponding to the central portion of the grid. An example for a circular grid is shown in Figure 34 which plots the coefficients of  $\hat{\mathbf{C}}_i^{-1}$  as a function of distance between reradiators  $k$  and  $l$ . In this case the matrix  $\mathbf{C}_G$  for a multipath source of up to  $10\lambda$  could be reasonably approximated. Ignoring the edge effects, the behaviour of the coefficients at a distances greater than one

wavelength suggests a simple expression. Based on this and other simulation examples, the following expression was developed:

$$\gamma_{kl} = \frac{-\mu_m^3}{2\lambda} \left( \frac{j}{r_{kl}^2} + \frac{\lambda}{2\pi r_{kl}^3} \right) e^{-j\frac{2\pi}{\lambda} r_{kl}} \quad \text{for } r_{kl} > 2\mu_m \quad (125)$$

where  $\gamma_{kl}$  is the element of  $\mathbf{C}_G$  or  $\mathbf{C}_i^{-1}$  corresponding to reradiators  $k$  and  $l$ . For values of  $\gamma_{kl}$  where  $0 < r_{kl} \leq 2\mu_m$  the above expression is less accurate. The value of  $\gamma_{kk}$  (where  $r_{kk} = 0$ ) is dependent on the grid spacing, wavelength, and  $\mu_m^2$ , but generally

$$1 < |\gamma_{kk}| < 1.5 \quad (126)$$

Numerically, it has been found that for an infinite circular grid with  $d = \mu_m$  and  $\mu_m/\lambda \rightarrow 0$  then  $\gamma_{kk} \approx 1.295$  for all values of  $k$ . (Note that if the simplifying approach described in Appendix A is used, and  $\gamma_{kl}$  is defined as a diagonal element of the inverse modified coupling matrix  $\mathbf{C}_c^{-1}$ , then  $\gamma_{00} \approx 1.295$  and  $0.87 < \gamma_{kk} < 0.92$  for  $k > 0$ ).

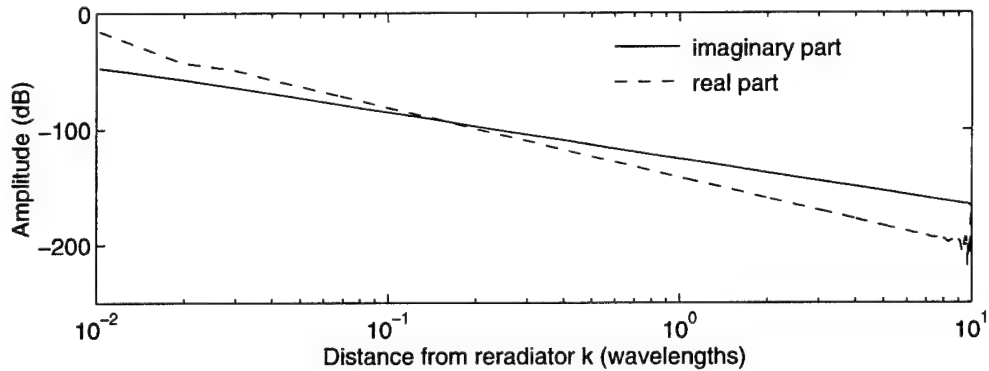


**Figure 34:** Values of the coupling elements  $\gamma_{kl}$  as a function of the distance between reradiators  $r_{kl}$ .

Incorporating the preceding simplifications into equation (119) yields

$$s_{rg} = s_{ri} - s_{tx} \mathbf{q}_c^T (\mathbf{C}_G + \mathbf{\Upsilon}^{-1})^{-1} \mathbf{p}_c \quad (127)$$

Using the definition for multipath (93), then

$$s_{mult} = -s_{tx} \mathbf{q}_c^T (\mathbf{C}_G + \mathbf{\Upsilon}^{-1})^{-1} \mathbf{p}_c \quad (128)$$

In this last expression, the calculation of the effects of multipath has been reduced to considering only the reradiators where  $\beta_k \neq -1$ . Assuming that this does not include the



entire ground grid, then the above expression results in a computational savings.

Defining the dielectric coupling matrix as

$$\mathbf{C}_\epsilon = -(\mathbf{C}_G + \mathbf{\Upsilon}^{-1}) \quad (129)$$

(where the negative sign accounts for the negative sign in (128)), the expression for  $s_{mult}$  can easily be related to the freespace version (54). In this case  $\mathbf{p}_\epsilon$  and  $\mathbf{q}_\epsilon$  serve in the role of transmitter-multipath source and multipath source-receiver attenuation vectors respectively. The corresponding *dielectric earth* attenuation function is then given by

$$\rho_\epsilon(r) = \frac{-\mu_m \mu h}{\lambda} \left( \frac{j}{r^2} + \left(1 - \frac{2\mu_m h}{\lambda^2}\right) \frac{\lambda}{2\pi r^3} \right) e^{-j\frac{2\pi}{\lambda}r} \quad (130)$$

where  $h$  is the height of the transmitter or receiver antenna (as appropriate) and  $\mu = \mu_m$  for the transmitter-multipath source path, and  $\mu = \mu_r$  for the multipath source-receiver path. Compared to the freespace case, for increasing  $r$  the amplitude attenuation is a function of  $r^{-2}$  rather than  $r^{-1}$  and a phase shift of  $-90^\circ$  has been introduced.

Continuing the equivalence with the freespace equations, the effective dielectric earth reradiation coefficient can be defined in terms of the diagonal elements of  $\mathbf{C}_\epsilon$ . The result is given by

$$\begin{aligned} \beta_\epsilon &= \left( \gamma_{kk} - \frac{\beta}{1 + \beta} \right)^{-1} \\ &= \frac{1 + \beta}{\gamma_{kk} + \gamma_{kk}\beta - \beta} \end{aligned} \quad (131)$$

where  $\beta \neq 1$ . Although slightly complicated looking, since  $\gamma_{kk} \approx 1$ , then  $\beta_\epsilon \approx 1 + \beta$ .

As in the case of the definitions developed in the previous section for terrain and vegetation features, the definitions for the attenuation function  $\rho_\epsilon(r)$  and effective reradiation coefficient  $\beta_\epsilon$  developed here can be used in place of the corresponding freespace definitions to implement any of the methods described in Sections 2.0 or 3.0. There is, however, a slight problem with the computation of the off-diagonal elements of the the dielectric coupling matrix. For example, making the appropriate substitutions in (50) yields

$$c_{kl} = \rho_{\epsilon m}(r_{kl}) \quad \text{for } k \neq l, \quad k, l = 1, 2, 3, \dots, N \quad (132)$$

Since the ground grid reradiators are at the same height ( $h = 0$ ), the result is  $c_{kl} = 0$  which contradicts the result computed from (125) using the fact that  $c_{kl} = -\gamma_{kl}$ . Fortunately, this problem is easily remedied by setting  $h = -\mu_m/2$  in which case (132) becomes a very good approximation for (130).

In comparing the effects of variations in elevation to variations in the electrical properties of the earth, the effects are remarkably similar, especially when path losses (or amplitude attenuations) are considered. The main difference being that the factor  $2\sqrt{\pi}z$  in the elevation case has been replaced by  $-\mu$ . This difference, however, means that for similarly sized features (as measured on the X-Y plane), elevation effects would be expected to dominate, particularly when  $z > \mu/2\sqrt{\pi}$ .

## 5.0 SUMMARY OF MULTIPATH EQUATIONS

The multipath models developed in this report are based on representing multipath sources by collections of reradiators. This was shown to lead to the expression

$$s_{mult} = s_{tx} \mathbf{q}_\nu^T \mathbf{C}_\nu^{-1} \mathbf{p}_\nu \quad (133)$$

where  $s_{mult}$  is the multipath signal picked up by the receiving antenna,  $s_{tx}$  is the transmitted signal amplitude (measured at the transmitting antenna),  $\mathbf{p}_\nu$  is the transmitter-radiator complex attenuation vector,  $\mathbf{q}_\nu$  is the reradiator-receiver complex attenuation vector, and  $\mathbf{C}_\nu$  is the reradiator coupling matrix. The elements of the attenuation vectors are defined by

$$p_k = -\rho_{\nu m}(r_{ak}) \quad (134)$$

and

$$q_k = \rho_{\nu r}(r_{bk}) \quad (135)$$

respectively, and the elements of the coupling matrix are defined by

$$c_{kl} = \begin{cases} \rho_{\nu m}(r_{kl}) & \text{for } k \neq l \\ \frac{-1}{\beta_{\nu k}} & \text{for } k = l \end{cases} \quad (136)$$

The definition of the attenuation functions  $\rho_{\nu m}(\cdot)$ ,  $\rho_{\nu r}(\cdot)$ , and the reradiation coefficient  $\beta_{\nu k}$  is dependent on the propagation conditions. The three conditions considered in this report were: free space propagation, propagation over ground with vegetation and terrain features, and propagation over a flat ground with varying electrical properties (nonhomogeneous dielectric earth). To distinguish these three conditions, the subscript  $\nu$  is replaced by  $\alpha$ ,  $z$ , and  $\epsilon$  accordingly. The definitions appropriate to each propagation condition are given in the next three subsections.

## 5.1 Freespace Equations

### Attenuation Functions

$$\rho_{\alpha m}(r) = \begin{cases} \frac{\mu_m}{2\sqrt{\pi}r} e^{-j\frac{2\pi}{\lambda}r} & \text{for } r \geq \frac{\mu_m}{2\sqrt{\pi}} \\ e^{-j\frac{2\pi}{\lambda}r} & \text{otherwise} \end{cases} \quad (137)$$

$$\rho_{\alpha r}(r) = \begin{cases} \frac{\mu_r}{2\sqrt{\pi}r} e^{-j\frac{2\pi}{\lambda}r} & \text{for } r \geq \frac{\mu_r}{2\sqrt{\pi}} \\ e^{-j\frac{2\pi}{\lambda}r} & \text{otherwise} \end{cases} \quad (138)$$

### Reradiation Coefficient

$$\beta_{\alpha k} = \beta_k \quad (139)$$

## 5.2 Vegetation and Terrain Feature Equations

### Attenuation Functions

$$\rho_{zm}(r) = \rho_{\alpha m}(r) - \rho_{\alpha m}(r') \quad (140)$$

$$= \frac{2\sqrt{\pi}\mu_m h_a z_k}{\lambda} \left( \frac{j}{r^2} + \left(1 + \frac{4\pi^2 h_a z_k}{\lambda^2}\right) \frac{\lambda}{2\pi r^3} \right) e^{-j\frac{2\pi}{\lambda}r} \quad \text{for } r^2 > 4h_a z_k \quad (141)$$

$$\rho_{zr}(r) = \rho_{\alpha r}(r) - \rho_{\alpha r}(r') \quad (142)$$

$$= \frac{2\sqrt{\pi}\mu_r h_b z_k}{\lambda} \left( \frac{j}{r^2} + \left(1 + \frac{4\pi^2 h_b z_k}{\lambda^2}\right) \frac{\lambda}{2\pi r^3} \right) e^{-j\frac{2\pi}{\lambda}r} \quad \text{for } r^2 > 4h_b z_k \quad (143)$$

where  $r' = \sqrt{r^2 + 4hz}$ . When calculating  $c_{kl}$  using  $\rho_{zm}(r)$ , the transmitter height is taken

to be the height of the appropriate reradiator, i.e.  $h_a = z_l$ .

#### *Reradiation Coefficient*

$$\beta_{zk} = \frac{\beta_k}{1 + \beta_k \rho_{\alpha m}(2z)} \quad (144)$$

### 5.3 Nonhomogeneous Dielectric Earth Equations

#### *Attenuation Functions*

$$\rho_{em}(r) = \frac{\mu_m^2 h_a}{\lambda} \left( \frac{j}{r^2} + \left(1 - \frac{2\mu_m h_a}{\lambda^2}\right) \frac{\lambda}{2\pi r^3} \right) e^{-j\frac{2\pi}{\lambda}r} \quad \text{for } r > 2\mu_m \quad (145)$$

$$\rho_{er}(r) = \frac{-\mu_m \mu_r h_b}{\lambda} \left( \frac{j}{r^2} + \left(1 - \frac{2\mu_m h_b}{\lambda^2}\right) \frac{\lambda}{2\pi r^3} \right) e^{-j\frac{2\pi}{\lambda}r} \quad \text{for } r > 2\mu_m \quad (146)$$

When calculating  $c_{kl}$  using (136) and (145) the transmitter height is taken to be  $h_a = -\mu_m/2$ . Values of  $c_{kl}$  for  $r \leq 2\mu_m$  are more accurately determined through simulation as outlined in Section 4.3.

#### *Reradiation Coefficient*

$$\beta_{ek} = \frac{1 + \beta_k}{\gamma_{kk} + \gamma_{kk}\beta_k - \beta_k} \quad (147)$$

The value of  $\gamma_{kk}$  is given by the  $k^{th}$  diagonal element of  $\mathbf{C}_i^{-1}$ .

## 6.0 REAL WORLD MODELLING EXAMPLES

In this section, two examples are provided of how the equations and methods developed in this report can be applied to analysis of the effects of VHF multipath on a terrestrial path. In these examples measurements from two separate field trials are presented which clearly show the effects of multipath. These effects are then duplicated by setting up computer simulations and making the appropriate choices and approximations for the simulations. In fact, even using some very simplistic approximations to simplify the processing requirements, some very useful results are developed.

### 6.1 Example 1

In 1994, field trials were carried out at DREO where a mobile VHF CW transmitter was set up to travel slowly down a predefined route such as the one shown on the map in Figure 35. The rate of travel of the mobile transmitter was 0.3 m/s covering a total distance of approximately 160 meters or more. The transmitting frequency used was 62.5 MHz for a signal wavelength of 4.8m. The receiving system consisted of an eight-channel receiver connected to an eight-element linear array located at the position marked "Osprey" on the map. Measurements were made at a rate of 4 samples/second. For this first example, the results for the route shown in Figure 35 are discussed, and this discussion is restricted to the measured signal power averaged for all 8 channels which is shown in Figure 36. The signal-to-noise ratio was sufficiently high that the observed fluctuating behaviour or power ripple in the signal power was due to spatial effects (multipath), and not temporal effects, i.e. repeating the experiment produces a nearly identical signal power pattern.

The explanation for the observed ripple in power is relatively simple. As the transmitter moves, the path lengths of the direct path and the secondary paths also change. Since these paths do not all change at the same rate, the relative phase of the direct and multipath signals are modified. The resultant amplitude of the composite signal is affected accordingly. The period of the power ripple, measured in terms of transmitter distance travelled, is dependent on geometry considerations. Generally multipath sources nearer the receiver causes power ripple with long periods (transmitter distances of many wavelengths) while multipath sources close to the transmitter cause power ripples with periods ranging from very long to very short (on the order of one wavelength or less). Individual multipath sources tend to produce variations whose period is relatively constant (i.e. constant spatial frequency) except when the transmitter is passing by. Inspection

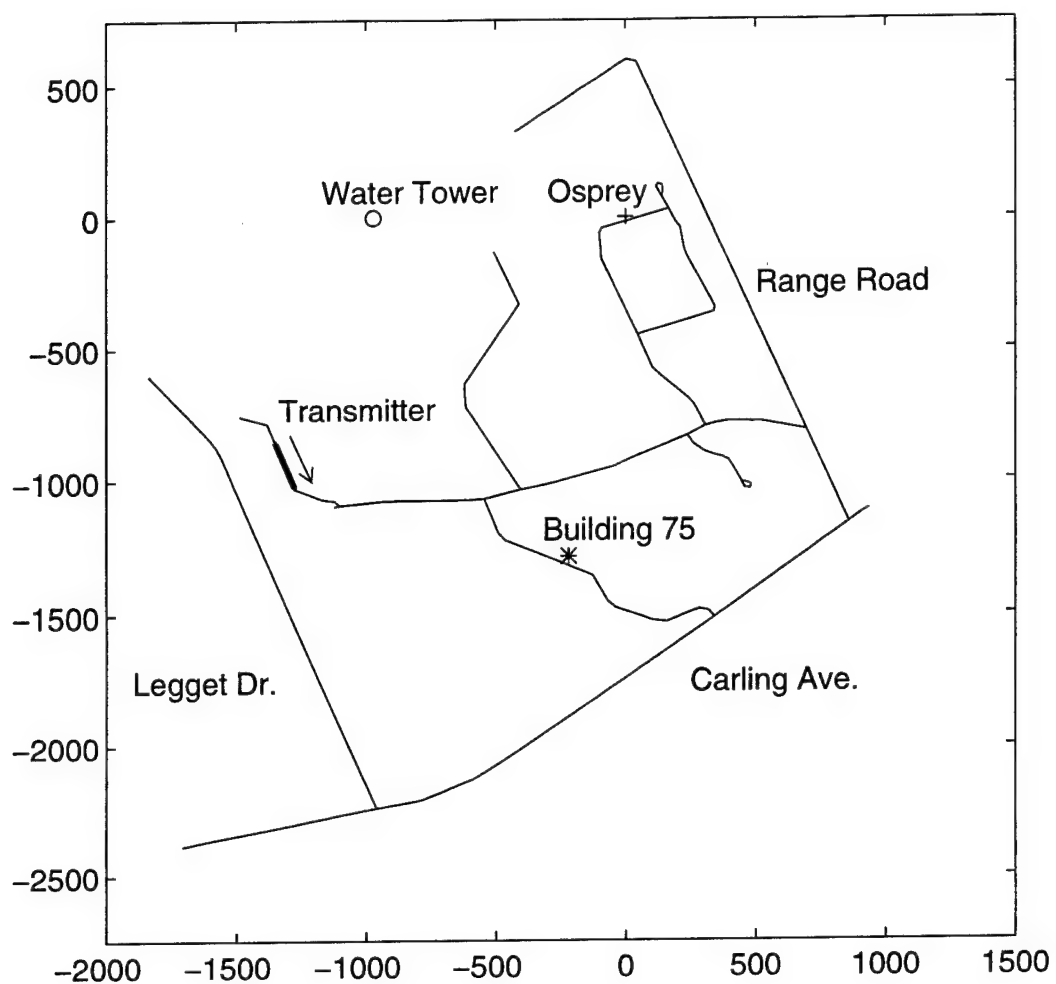


**Figure 35:** Map showing site of multipath measurements carried out at DREO in 1994. Transmitter route is shown by the arrow.

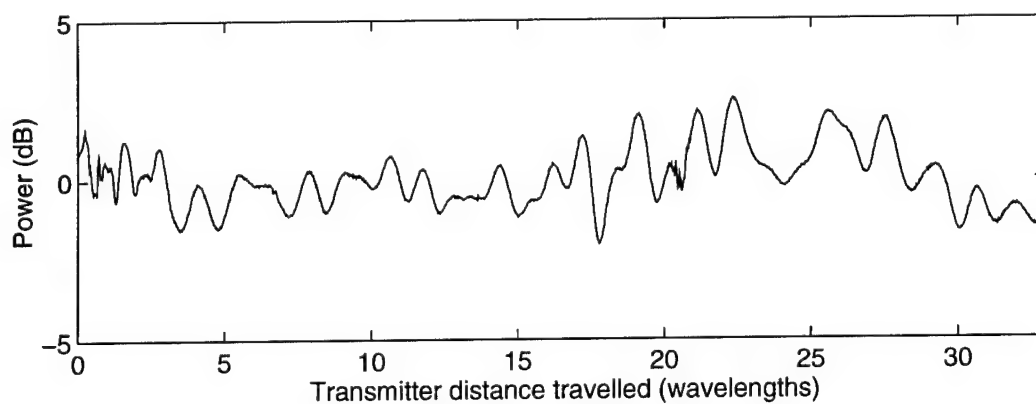


**Figure 36:** Received signal power measured with respect to the transmitter position.

of the data reveals that there appears to be many spatial frequency components (i.e. its “noise-like”), indicating that the multipath was produced by a number of different sources – some of which were definitely located near the transmitter.

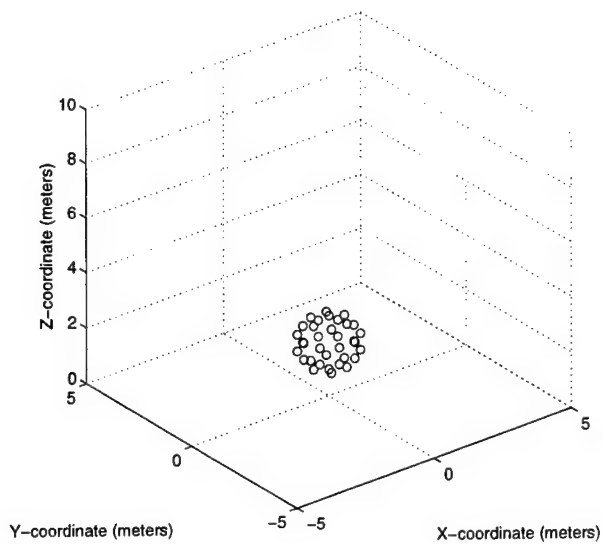
To simulate this measurement, and hopefully learn more about the multipath source, a computer experiment was set up using the same transmitter-receiver geometry and a large number of multipath sources randomly placed over the area shown in Figure 35 using a uniform distribution. Given that terrain features have a greater effect than variations in the electrical properties of the ground, the multipath sources were modelled using the elevated earth equations derived in Section 4.2. The received multipath signal was calculated using the internal coupling approach described in Section 3.3.2. This approach accounts for coupling effects within each multipath source, but ignores the coupling between sources. To minimize the error introduced by this omission, farfield conditions were imposed (i.e. no multipath source was placed closer than the distance  $4D^2/\lambda$  to any other multipath source, the transmitter, or the receiver). The justification for using the internal coupling approach is discussed in Section 6.3.

To properly investigate the effects of multipath it would be necessary to simulate a wide variety of shapes, sizes, and number of multipath sources. For the purposes of brevity, only three computer simulations are described here. In each simulation the size and shape of the multipath sources were identical, and their number was chosen so that the signal-to-multipath power ratio was approximately 10-12 dB which results in a variation in signal power similar in magnitude to the actual measured case.

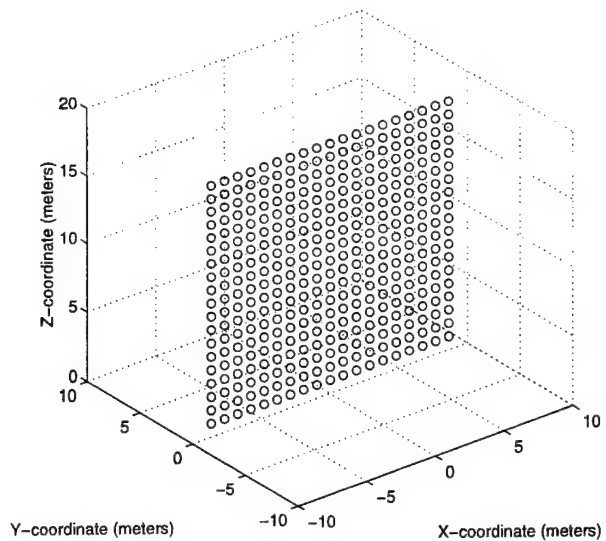
The three multipath shapes modelled were a small hollow sphere, a large vertical flat surface, and a hollow lollipop shaped structure. These shapes are shown in Figures 37a-c. The first two shapes were chosen to represent two extremes types of multipath sources, namely, a small scatterer (e.g. a small bush) and a large reflector (e.g. the side of a building). The third source was chosen to have an intermediate size in order to approximate a common terrain feature, namely, a leafy deciduous tree. In the simulation using the reflector, the orientation of the surface for each multipath source was chosen to be vertical with the lowest edge parallel to the ground plane and aligned randomly in azimuth.

The results of the simulations are contained in Figure 38 and Figure 39. Figure 38a-c shows the location of the most significant multipath sources for each simulation while Figure 39a-c show the corresponding signal powers averaged over the 8 receiving channels. In generating the location maps in Figure 38, significant multipath sources

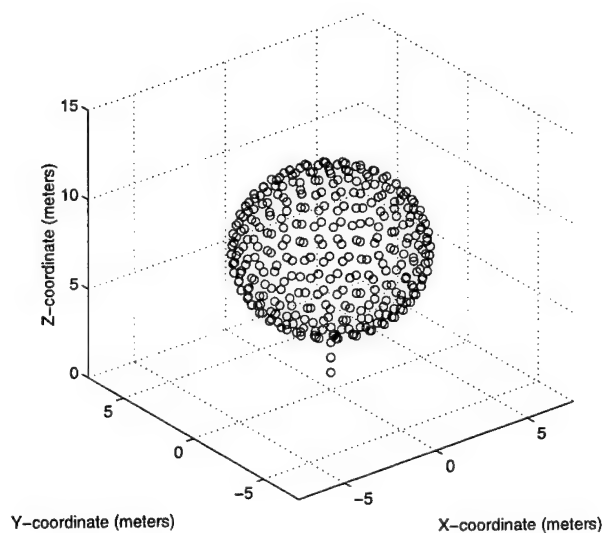




(a)



(b)



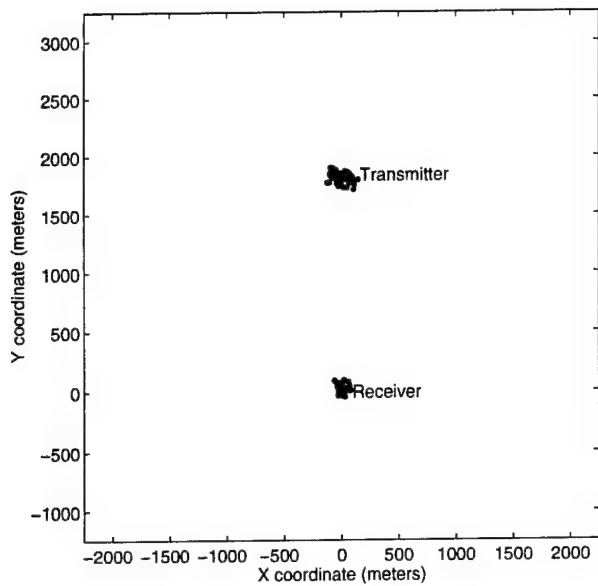
(c)

**Figure 37:** Shape of multipath sources showing reradiator positions for (a) small scatterer model, (b) tree model, and (c) large reflector model.

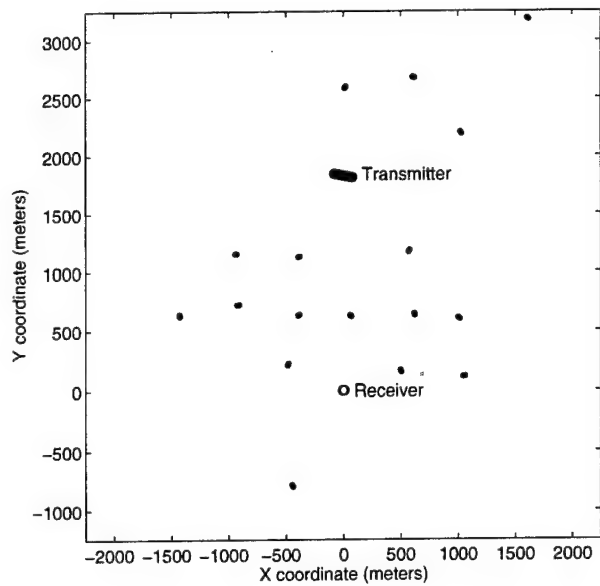
were considered to be those which contributed 99.9% of the total multipath power. The advantage of this style of presentation is that it clearly shows the areas where the greatest amount of multipath is generated. In Figure 38a, for example, the high losses incurred by the scattering of a signal by a small multipath source results in a tight clustering of the significant scattering sources around either the transmitter or the receiver. For a large appropriately oriented reflecting source, the losses due to the multipath source are relatively low and as a consequence significant multipath sources can be found in a large region encompassing the transmitter, receiver, and the area in between as shown in Figure 38b. The tree shape represents a multipath source whose size lies between these two extremes and this fact is reflected by the results shown in Figure 38c.

Qualitatively, the three simulated signal power plots are different. The power plot for both the small scatterer and the tree models exhibit rapid variations in magnitude with periods as short as one wavelength. The main difference between these two models is that the changes in the magnitude of the variations are more dramatic for the small scatterer. This is due to the fact that since the region of influence of a small scatterer is relatively small, large rapid variations will only occur when the transmitter is close to the scatterer which will rapidly diminish as the transmitter moves away. Hence the behaviour of the variations can change quickly over a few wavelengths. The tree model has a larger area of influence so that the change in behaviour does not occur as rapidly.

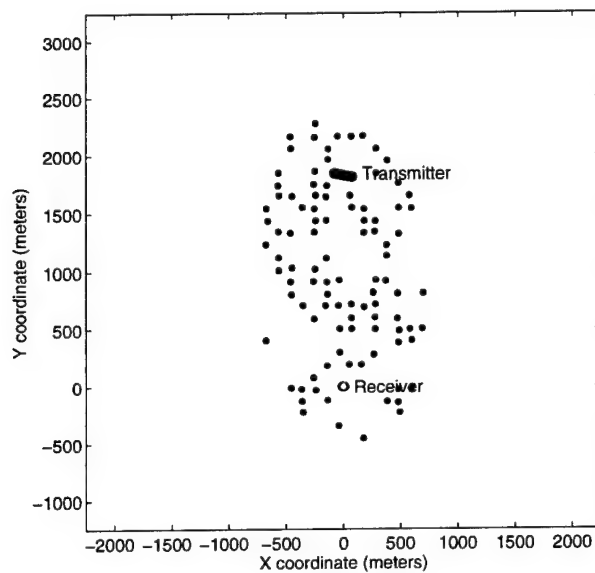
The power plot for the large reflector is markedly different than for the two smaller shapes. The most obvious difference is that the shortest period for the power ripple is much longer than a wavelength. This is due to the averaging effect of the receiving array, an effect which becomes more pronounced as the bearing difference between the transmitter and multipath source (as measured from the receiver) increases. Around the transmitter, the multipath sources most affected are those approximately along the same line as the direction of travel – the farther away, the greater the effect. These are also coincidentally, the same multipath sources which give rise to the most rapid variations in the power (with spatial periods of a wavelength or less), and consequently these rapid variations tend to be smoothed out. In the previous cases of the small scatterer and tree models, the multipath sources were not sufficiently distant from the transmitter in order for there to be much effect. Obviously, rapid variations can still occur if the reflector is placed close to the transmitter, however, in the simulation the farfield condition was imposed which prevents this from happening. In real life measurements, it would only be necessary to ensure that no large potential multipath sources are located too close to the transmitter (in the actual measurement already described, the transmitter was located in



(a)

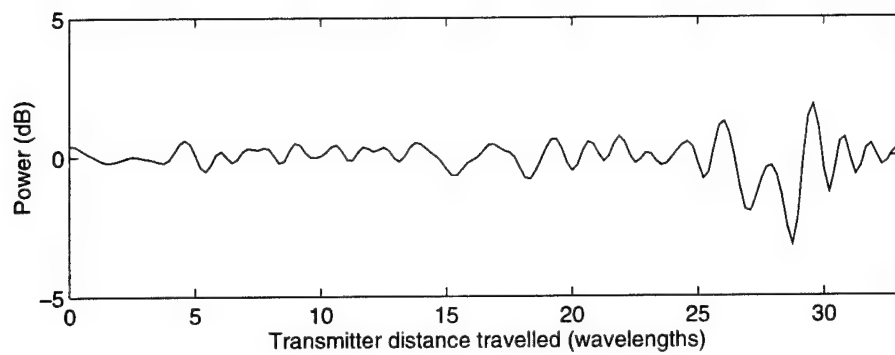


(b)

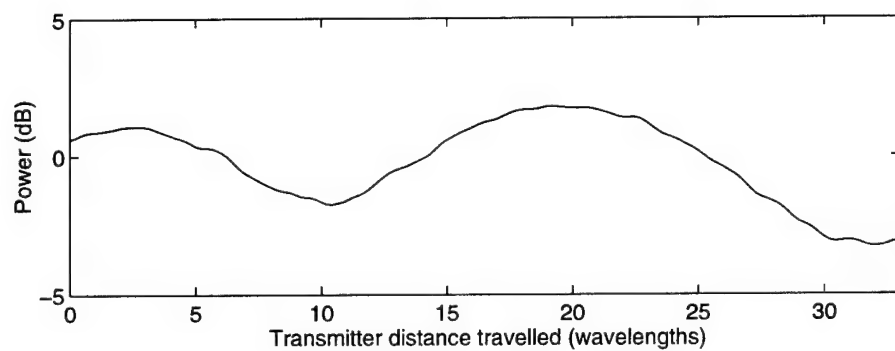


(c)

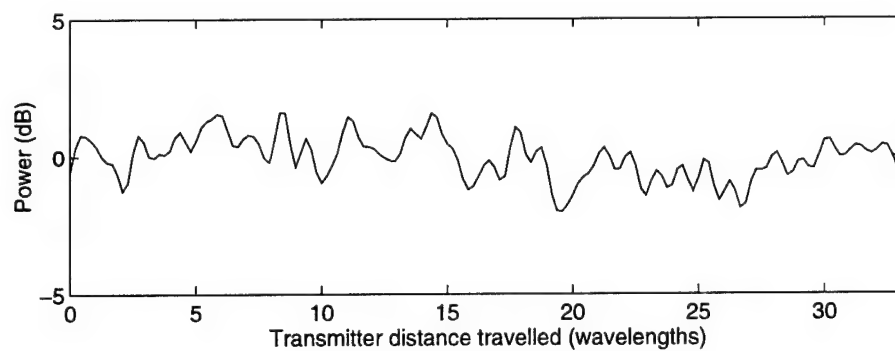
**Figure 38:** Location of most significant multipath sources (shown by dots) using (a) small scatterer model, (b) tree model, and (c) large reflector model.



(a)



(b)



(c)

**Figure 39:** Received signal power using (a) small scatterer model, (b) tree model, and (c) large reflector model.

open country). Hence the averaging effect can be used to advantage to help distinguish between different types of multipath sources.

Using the characteristics discussed here as a means of distinguishing between the multipath source models, the tree model appears to produce the results which best match the actual results shown in Figure 36. Since the moving transmitter technique employed tends to favour identification of multipath sources in the vicinity of the transmitter (i.e. the higher frequency components in the data are easier to identify than the lower frequency components), and the transmitter was located in open country with scattered trees, then the match between the simulation and measurement is gratifying. Based on these results the tentative conclusion would be that trees were the dominant source of multipath. Obviously more measurements and simulation modelling would be required to support this conclusion, especially considering that in real life, trees and other sources of multipath come in a variety of shapes and sizes.

## 6.2 Example 2

In 1992, field trials were carried out at DREO using a wideband DF system against a wideband transmitter. A map of the site for one particular transmitter-receiver combination is shown in Figure 40. The DF antenna consisted of a circular array of 4 dipole elements mounted on a mast raised to a height of 8 meters. Bearing estimates were made using the phase differences between antennas (similar in principle to the phase interferometer approach). The bearing results over a 6 MHz band for the transmitter-receiver site combination in the map is shown in Figure 41.

The ripples in the measured bearing data as a function of frequency are again due to path length differences between the direct path and secondary paths. Although the path lengths remain fixed in this case, the phase differences between the direct and secondary paths change due to the change in signal frequency. Generally, the longer the secondary path, the shorter the period of the bearing ripple. Mathematically, the additional or excess path length can be determined from this period according to

$$\text{Excess Path} = c/\Delta_f \quad (148)$$

where  $c$  is the speed of light and  $\Delta_f$  is the frequency period of the observed bearing ripple. This expression assumes the direct signal is the dominant signal (e.g. not completely blocked by some large obstacle) and that only a single multipath source is involved in

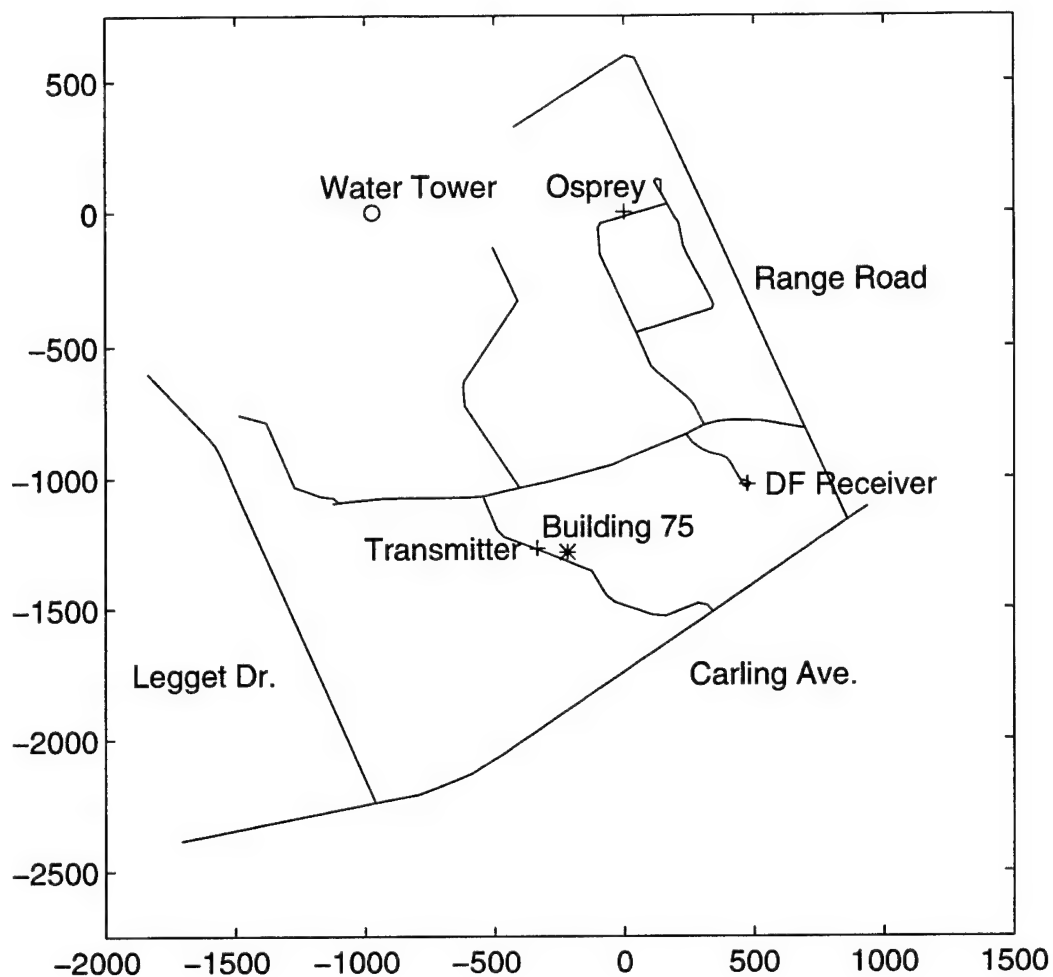


**Figure 40:** Map showing site of wideband DF measurements carried out at DREO in 1992.

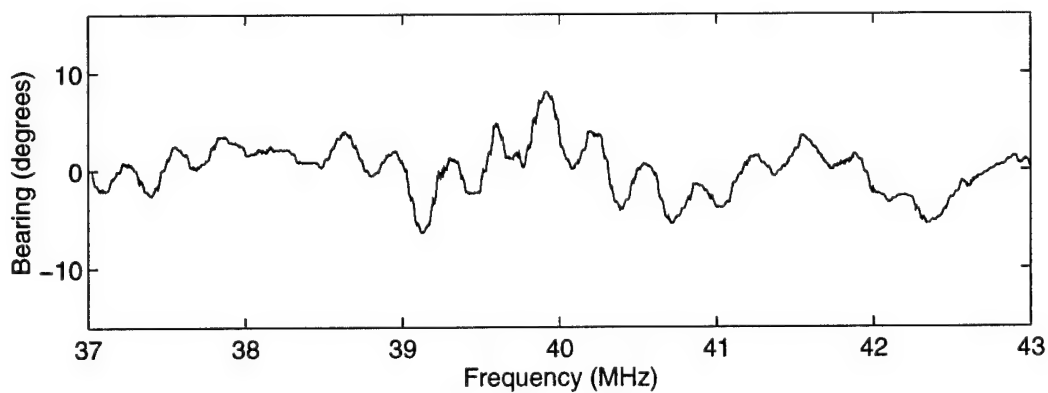


**Figure 41:** Received signal power measured with respect to the transmitter frequency.

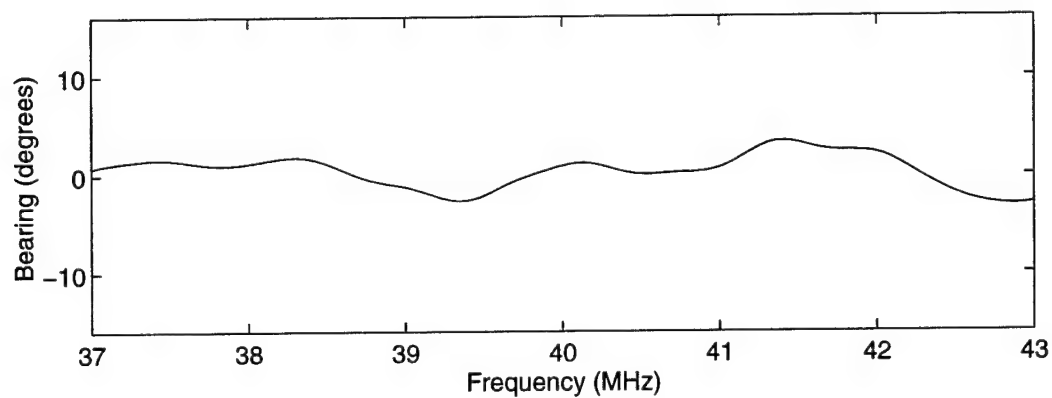
producing the bearing ripple. In Figure 41, the bearing ripple contains several components with different periods, however one component with a period of 325 kHz is clearly evident. Assuming this is caused by a single source, then using the above expression, the excess path length is 923 m.

To simulate the wideband DF measurement, a computer experiment was again setup employing the same transmitter and DF receiver geometry as the actual measurement. Using a uniform distribution, multipath sources were spread randomly across the region encompassing the transmitter and receiver. The density of multipath sources was chosen to give a signal-to-multipath power ratio of approximately 10 dB. The farfield condition was again imposed to allow the internal coupling method to be used. Since an excess path of 923m suggests larger multipath sources, only the tree model and large flat reflecting surface model were tested in the simulations. The dimensions of the tree model were the same as before while the flat surface was composed of a  $14 \times 14$  grid of reradiators with a reradiator spacing of  $d = 1.5\text{m}$  (instead of a  $19 \times 19$  grid with  $d = 0.96\text{m}$ ). The results of the simulations are shown in Figure 42.

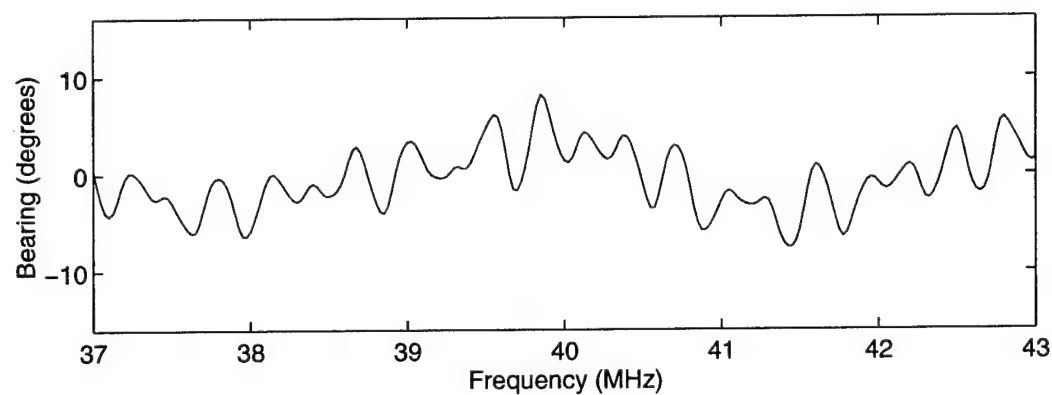
Comparing the simulation results to the actual measurements reveals that the large reflecting surface model provides a more realistic simulation, particularly when the bearing ripple components with short periods are considered. This is in contrast to the results found in the first example. The reason for this is probably due to the fact that in this second example the transmitter was located near a number of medium sized buildings, while in the first example the transmitter was in an open area with a few scattered trees (the receiver environments were similar in both cases – open field surrounded by groves of trees). Alternatively, the results of the second example may still indicate that smaller tree sized objects still dominate, but that the environment does contain a few larger reflectors. The higher frequency bearing ripple in Figure 41, for example, may have be due to a single multipath source only. Hence, this suggests that more real measurements would be required to make a better assessment, and that simulations should include a variety of multipath models with varying sizes and shapes which have dimensions similar to those found in the real environment.

### 6.3 Assumption Verification

In the examples presented in this section, a number of simplifications were used to reduce the processing. In particular, the farfield condition was introduced to allow the



(a)



(b)

**Figure 42:** Received signal power using (a) tree model, and (b) large reflector model.



use of the internal coupling method which greatly simplifies processing. This simplification was therefore based on two assumptions: imposing farfield conditions would not distort the results, and coupling between multipath sources could be ignored. An important question when considering the results was were these assumptions valid?

The justification for the farfield assumption was that it was found that for the densities of multipath sources required to generate a realistic amount of multipath, the average spacing exceeded the farfield condition. However, in the real world, no such condition is imposed so that in some situations this could lead to erroneous results. This was apparent when analyzing the result for Figure 39c where it was previously pointed out that the farfield condition in conjunction with the averaging of the receive array leads to a slowly varying signal power plot – a result that would only occur in real life if the multipath sources were some distance from the transmitter. Had the transmitter been located close to a large grove of trees, the power measurements could have easily exhibited rapid variations similar to those generated by smaller multipath sources, leading to the false conclusion that the multipath effects were generated by isolated trees.

Previously it was found (Section 3.3.3) that coupling between sources could be ignored if farfield condition were met. As a precaution and where possible, simulations were also carried out using the full method and the multipath source coupling method. In all cases the shape of the power plots were virtually indistinguishable from the shape generated using the internal coupling method. Generally, the received multipath power was slightly higher (1 dB or less) for internal coupling method than the other two methods. Since the shape of the signal power plots was of most interest, the small error in received multipath power was inconsequential.

From this discussion, it is clear that under the conditions specified, the assumptions used for the simulations in the examples were reasonable. It is also equally clear that the success of any simulation is highly dependent on the validity of the underlying assumptions. Hence a very important part of the modelling process necessarily includes verification of the underlying assumptions

## 7.0 CONCLUSIONS

In this report, a new approach to modelling propagation effects that occur for terrestrial paths was introduced. The main motivation for developing this approach was to provide a means of investigating effects observed in VHF radio direction finding measurements for terrestrial paths. Particularly the effects due to multipath caused by the transmitted radio signal being reradiated, reflected, or diffracted off of bushes, trees, forests, buildings, hills, etc.

The new approach is based on representing the terrain and vegetation, which effect the signal path, by a large number of small (relative to the signal wavelength) isotropic reradiators. In this way it incorporates some of the sophistication found in the more complex and computationally intensive electromagnetic methods commonly used for antenna modelling. This degree of sophistication is necessary to help understand the fine scale effects observed in actual measured data (e.g. rapid changes in received signal amplitude as the transmitter is moved distances of as little as one wavelength). Current propagation models tend to overlook these fine scale effects.

Despite being simpler than electromagnetic methods, the computational requirements for the new approach can easily exceed the abilities of most present day computers for problems involving typical military signal paths. However, various simplifications can be employed to greatly simplify the computations depending on the complexity of the terrain and vegetation, and the qualities of the model data that are of most interest. For example, a flat homogeneous ground with only a few terrain features can be modelled by subdividing the terrain features into collections of isotropic reradiators. The effect of the rest of the ground can then be directly incorporated into the calculations without having to subdivide it as well. If these features are far enough apart, it may be possible to ignore the coupling interaction between these features. The calculations can then be done by examining one feature at a time and using superposition to get the final results.

Using some of these simplifications, it was shown that the new method was able to produce results which were comparable to real world examples. In addition by making suitable adjustments to the simulation in terms of the number of sources of multipath, their size and shape, the best results were achieved when the adjusted parameters mostly matched those of the corresponding features in the real world.

For complex environments (lots of obstacles in the signal path such as bushes, trees, etc.), coupling effects become more and more important. Under these conditions, the

number of features to be modelled and the fact that coupling effects need to be considered, would likely make the computations for the new method prohibitive. Hence more work will be required in simplifying the computations if these environments are to be analyzed.

In general, the new method provides a means of better understanding the effects due to multipath observed in terrestrial VHF signal problems. In particular, understanding the effects due to small changes in the position of the transmitter or receiver, or small changes in the transmission frequency. It also opens up the possibility of testing and developing new VHF DF algorithms which are better able to deal with the VHF multipath environment than current approaches. Additionally, it will also be possible to test the usefulness of different DF site calibration methods, and possibly develop improved ones.

## REFERENCES

- [1] Read, W., "The Effects of the Environment on an Experimental VHF Radio Direction Finding Antenna System", Defence Research Establishment Ottawa, Report No. 1226, August 1994.
- [2] Read, W.,J.,L., "Measurements of Multipath and its Effects on Terrestrial VHF Radio Direction Finding", DREO Report xxxx, February 1996.
- [3] Whittaker, J.H., "Ground Wave and Diffraction", *Propagation Modelling and Decision Aids for Communications, Radar and Navigation Systems*, AGARD Lecture Series 196, pp. 2A-1 to 2B-14, September 1994.
- [4] Born, M., and Wolf, E., *Principles of Optics*, Pergamon Press, Oxford, England, p. 132, 1965.
- [5] "Report on VHF DF Super-resolution Field Trials held at Defence Research Establishment Ottawa", TTCP Report by Subgroup Q, Technical Panel QTP-18, September 1994, CONFIDENTIAL.
- [6] "Nav aids and Avionics Enroute Systems, Doppler VHF/DF, Site Selection", Publication No. C4-2VHF/DF-3, Telecommunications and Electronics Branch, Transport Canada, March 1, 1976.
- [7] Kraus, J.D., *Antennas*, McGraw-Hill Book Company, New York, U.S.A, Chapter 3.11, 1950.
- [8] Beckmann, P., and Spizzichino, A., *The Scattering of Electromagnetic Waves from Rough Surfaces*, Artech House, Inc., Norwood, MA, U.S.A, Chapters 2.2, 1987.
- [9] *Linear Systems*, Thomas Kailith, Editor, Prentice-Hall, Inc, Englewood Cliffs, N.J., U.S.A, pp. 655-656, 1980.
- [10] Shigekazu, S., *A Basic Atlas of Radio-Wave Propagation*, John Wiley and Sons, 1987.
- [11] Wolfram, S., *Mathematica: A System for Doing Mathematics by Computer*, Addison-Wesley Publishing Company Inc., Redwood City, California, 1991.

## APPENDIX

### A.0 CIRCULAR GROUND GRID CALCULATIONS

In this section the analysis focuses on reducing the amount of processing required to perform ground grid calculations by using a circular grid of reradiators. This analysis is limited to the case where the transmitter is positioned above the center of the grid, and reradiators at the same radius from the center all have the same value for  $\beta$ .

Consider a circular grid of reradiators such as the one shown in Figure 31. Numbering the reradiators in a clockwise manner spiraling outwards, then equation (47) can be re-expressed as,

$$\begin{aligned}
 -s_{tx}\rho_m(r_0) &= \frac{-s_0}{\beta_1} + s_1 \sum_{i=2}^3 \rho_m(r_{1i}) + s_2 \sum_{i=8}^{19} \rho_m(r_{1i}) + s_3 \sum_{i=20}^{37} \rho_m(r_{1i}) + \dots \\
 -s_{tx}\rho_m(r_1) &= s_0\rho_m(r_{20}) + s_1 \left( \frac{-1}{\beta_2} + \sum_{i=3}^7 \rho_m(r_{2i}) \right) + s_2 \sum_{i=8}^{19} \rho_m(r_{2i}) + s_3 \sum_{i=20}^{37} \rho_m(r_{2i}) + \dots \\
 -s_{tx}\rho_m(r_2) &= s_0\rho_m(r_{80}) + s_1 \sum_{i=2}^7 \rho_m(r_{8i}) + s_2 \left( \frac{-1}{\beta_8} + \sum_{i=9}^{19} \rho_m(r_{8i}) \right) + s_3 \sum_{i=20}^{37} \rho_m(r_{8i}) + \dots \\
 &\text{etc.}
 \end{aligned} \tag{A.1}$$

The above expression can also be expressed in matrix form as

$$s_{tx}\mathbf{p}_c = \mathbf{C}_c \mathbf{s}_g \tag{A.2}$$

where  $\mathbf{p}_c$  is the transmitter-grid attenuation vector with elements defined by

$$p_k = -\rho_m(r_k) \tag{A.3}$$

$\mathbf{s}_g$  is the reradiated grid signal with elements  $s_0, s_1, s_2, \dots$ , and  $\mathbf{C}_c$  is the modified coupling matrix with elements given by

$$c_{kn} = \sum_{i=n_1}^{n_2} \rho_m(r_{k_1i}) \quad \text{for } k \neq n \tag{A.4}$$

## APPENDIX

and

$$c_{nn} = \frac{-1}{\beta_{n_1}} + \sum_{i=n_1+1}^{n_2} \rho_m(r_{n_1 i}) \quad (\text{A.5})$$

with  $k_1$  representing the lowest numbered reradiator in the  $k^{th}$  ring, and  $n_1$  and  $n_2$  representing the lowest and highest numbered reradiators in the  $n^{th}$  ring respectively. Finally, to solve for the reradiated signal  $\mathbf{s}_g$ , equation (A.2) is rearranged to get

$$\mathbf{s}_g = s_{tx} \mathbf{C}_c^{-1} \mathbf{p}_c \quad (\text{A.6})$$

Suppose now, that the receiver is colocated with the transmitter. The signal received from the grid can be found by summing the contributions from the individual reradiators. Mathematically,

$$s_{grid} = s_0 \rho_m(r_{b1}) + s_1 \sum_{i=2}^7 \rho_m(r_{bi}) + s_2 \sum_{i=8}^{19} \rho_m(r_{bi}) + \dots \quad (\text{A.7})$$

where  $r_{bk}$  is the distance from the receiver to the  $k^{th}$  reradiator. Since the distance for every reradiator in the  $n^{th}$  ring is given by  $r_n$  then this expression can be simplified to

$$s_{grid} = s_0 \rho_m(r_0) + s_1 6 \rho_m(r_1) + s_2 12 \rho_m(r_2) + \dots \quad (\text{A.8})$$

and using the matrix equations developed earlier, this can be rewritten as

$$s_{grid} = s_{tx} \mathbf{q}_c^T \mathbf{C}_c^{-1} \mathbf{p}_c \quad (\text{A.9})$$

where  $\mathbf{q}_c$  is the grid-receiver attenuation vector with elements defined by

$$q_k = K \rho_m(r_k) \quad (\text{A.10})$$

and where  $K$  is the number of reradiators in the  $k^{th}$  ring ( $K \approx 2\pi k$ ).

## DOCUMENT CONTROL DATA

(Security classification of title, body of abstract and indexing annotation must be entered when the overall document is classified)

1. ORIGINATOR (the name and address of the organization preparing the document. Organizations for whom the document was prepared, e.g. Establishment sponsoring a contractor's report, or tasking agency, are entered in section 8.) DEFENCE RESEARCH ESTABLISHMENT OTTAWA NATIONAL DEFENCE SHIRLEYS BAY, OTTAWA, ONTARIO K1A 0Z4 CANADA		2. SECURITY CLASSIFICATION (overall security classification of the document including special warning terms if applicable)  UNCLASSIFIED	
3. TITLE (the complete document title as indicated on the title page. Its classification should be indicated by the appropriate abbreviation (S,C or U) in parentheses after the title.)  MULTIPATH MODELLING FOR TERRESTRIAL VHF RADIO DIRECTION FINDING (U)			
4. AUTHORS (Last name, first name, middle initial) READ, WILLIAM J.L.			
5. DATE OF PUBLICATION (month and year of publication of document)  DECEMBER 1996	6a. NO. OF PAGES (total containing information. Include Annexes, Appendices, etc.) 94	6b. NO. OF REFS (total cited in document)  11	
7. DESCRIPTIVE NOTES (the category of the document, e.g. technical report, technical note or memorandum. If appropriate, enter the type of report, e.g. interim, progress, summary, annual or final. Give the inclusive dates when a specific reporting period is covered.)  DREO REPORT			
8. SPONSORING ACTIVITY (the name of the department project office or laboratory sponsoring the research and development. Include the address.) DEFENCE RESEARCH ESTABLISHMENT OTTAWA, NATIONAL DEFENCE SHIRLEYS BAY, OTTAWA, ONTARIO K1A 0Z4 CANADA			
9a. PROJECT OR GRANT NO. (if appropriate, the applicable research and development project or grant number under which the document was written. Please specify whether project or grant)  5BD12		9b. CONTRACT NO. (if appropriate, the applicable number under which the document was written)	
10a. ORIGINATOR'S DOCUMENT NUMBER (the official document number by which the document is identified by the originating activity. This number must be unique to this document)  DREO REPORT 1300		10b. OTHER DOCUMENT NOS. (Any other numbers which may be assigned this document either by the originator or by the sponsor)	
11. DOCUMENT AVAILABILITY (any limitations on further dissemination of the document, other than those imposed by security classification)  <input checked="" type="checkbox"/> (X) Unlimited distribution <input type="checkbox"/> ( ) Distribution limited to defence departments and defence contractors; further distribution only as approved <input type="checkbox"/> ( ) Distribution limited to defence departments and Canadian defence contractors; further distribution only as approved <input type="checkbox"/> ( ) Distribution limited to government departments and agencies; further distribution only as approved <input type="checkbox"/> ( ) Distribution limited to defence departments; further distribution only as approved <input type="checkbox"/> ( ) Other (please specify):			
12. DOCUMENT ANNOUNCEMENT (any limitation to the bibliographic announcement of this document. This will normally correspond to the Document Availability (11). However, where further distribution (beyond the audience specified in 11) is possible, a wider announcement audience may be selected.)  UNLIMITED			

13. ABSTRACT (a brief and factual summary of the document. It may also appear elsewhere in the body of the document itself. It is highly desirable that the abstract of classified documents be unclassified. Each paragraph of the abstract shall begin with an indication of the security classification of the information in the paragraph (unless the document itself is unclassified) represented as (S), (C), or (U). It is not necessary to include here abstracts in both official languages unless the text is bilingual).

(U) This report details the development of computer models to investigate and explain the effects of multipath on VHF radio direction finding (DF). The motivation for this development was to help explain the large and small scale multipath effects which occur for changes in transmitter and receiver position, or for changes in frequency. Particularly important in the analysis of current wide and narrow band DF approaches and the development of better ones. The new approach is based on representing the terrain and vegetation, which effect the signal path, by a large number of small (relative to the signal wavelength) isotropic reradiators. Polarization effects are not accounted for. Although this kind of approach can quickly become a computationally daunting task, a number of simplifications are introduced which greatly simplify the calculations. Two examples have been included illustrating the use of the proposed approach in the analysis and modelling real world measurements.

14. KEYWORDS, DESCRIPTORS or IDENTIFIERS (technically meaningful terms or short phrases that characterize a document and could be helpful in cataloguing the document. They should be selected so that no security classification is required. Identifiers, such as equipment model designation, trade name, military project code name, geographic location may also be included. If possible keywords should be selected from a published thesaurus. e.g. Thesaurus of Engineering and Scientific Terms (TEST) and that thesaurus-identified. If it is not possible to select indexing terms which are Unclassified, the classification of each should be indicated as with the title.)

MULTIPATH TRANSMISSION  
VHF  
DIRECTION FINDING  
PROPAGATION  
N-CHANNEL  
BEAM FORMING  
SIMULATION  
COMPUTER MODELS  
ANTENNA ARRAYS